# Mechanical Behaviour of Hawkesbury Sandstone Exposed to Different Heating Conditions

Keelan Cranfield-Brooks

BEng (Hons)

Thesis submitted in fulfilment of the requirements for the degree of Master of Research

Institute of Sustainable Industries and Liveable Cities

College of Engineering and Science

Victoria University, Melbourne, Australia

April 2024

# Abstract

Subsurface tunnels have become a critical solution for urban transportation in areas where road upgrade options are constrained by space or infrastructure limitations. However, the confined nature of tunnels and vehicles powered by combustion engines pose significant fire risks. Such fires, resulting from accidents, could compromise the integrity of the surrounding rock structure. Despite extensive research on fire effects in various settings, limited knowledge exists on fire's specific mechanical and chemical impacts on Hawkesbury sandstone, a rock type commonly encountered in Australian tunnel projects. This research addresses this knowledge gap by investigating the effects of fire on Hawkesbury sandstone's mechanical behaviour and chemical properties.

The study aimed to evaluate sandstone's mechanical and chemical responses subjected to controlled heating conditions that simulate real-world tunnel fire scenarios. Victoria University's NATA-accredited structural fire testing facility provided a unique platform for replicating these conditions. Experiments included heating of specimens following the Hydrocarbon Curve (HC) and Modified Hydrocarbon Curve (MHC), which reach peak temperatures of 1,100°C and 1,300°C, respectively, within five minutes, and specimens heating linearly at the rates of 2, 5, 10 and 20°C/min for comparison. The cylindrical sandstone specimens after heating were subjected to uniaxial compression strength (UCS) and splitting tensile strength tests to quantify mechanical changes. X-ray diffraction (XRD), Scanning Electron Microscopy (SEM) and digital image correlation (DIC) analyses were conducted to examine mineral transformations and the damage evolution behaviour.

The results demonstrated a consistent reduction in both UCS and tensile strength across all heating scenarios, with more pronounced degradation observed under the rapid heating conditions of the HC and MHC. These conditions also led to increased axial strain capacity, although discrepancies were noted between the axial strain measured by the testing apparatus and that observed in DIC analysis. Mineralogical analysis via XRD revealed enhanced crystallinity and an increased quartz content, accompanied by a reduction in clay minerals. SEM analysis was limited to elemental changes. This structural evolution correlated with the mechanical changes observed.

In conclusion, the study provides critical insights into the implications of tunnel fires on Hawkesbury sandstone. By establishing the mechanical and mineralogical

transformations of varying heating rates, this research contributes to the understanding necessary for geotechnical risk assessments and tunnel design considerations in fire-prone environments.

**Keywords:** Mechanical Properties, Sandstone, Fire Curves, Tunnel Fires, Thermal Shock

# Acknowledgements

I want to thank my supervisors, Dr Wasantha Liyanage and Dr Maurice Guerrieri, for providing technical support and reviewing the thesis draft. Special thanks to my principal supervisor for his endless patience with coordinating this research while living interstate under challenging circumstances. Thank you to Associate Professor Paul Joseph and Ph.D. candidate Thathsarani Kannangara of Victoria University's Werribee campus, who immensely helped with expanding the research scope by adding muffle furnace testing support. Thank you to Ian Snyders (Senior Geotechnical Engineer) and Zachary Corbett (Geotechnical Engineer) from Grange Resources for the countless hours spent improving my knowledge of rock mechanics.

# Declaration

I, Keelan Cranfield-Brooks, declare that the Master of Research thesis entitled "Mechanical Behaviour of Hawkesbury Sandstone Exposed to Different Heating Conditions" is no more than 50,000 words in length, including quotes and exclusive of tables, figures, appendices, bibliography, references, and footnotes. This thesis contains no material submitted previously, in whole or in part, for the award of any other academic degree or diploma. Except where otherwise indicated, this thesis is my work. I have conducted my research in alignment with the Australian Code for the Responsible Conduct of Research and Victoria University's Higher Degree by Research Policy and Procedures.

# Contents

# Tables

# Figures

# 1. Introduction

The tunnelling industry in Australia, reflective of global trends, is experiencing unprecedented growth in the 21st century [1]. Urbanisation, technological advancements, and the increasing need for sustainable infrastructure solutions, such as highways and railway bypassing through key congested areas in cities, are driving a surge in spending Australia-wide [2]. Significant projects are underway Australia-wide, including Melbourne Metro and West Gate Tunnel in Victoria, West Connect, Sydney Metro and Snowy 2.0 in New South Wales, and Cross River Rail in Queensland, indicating how much tunnel construction is underway Australia-wide with more projects. For densely populated urban areas, a tunnel offers a convenient and viable solution for enhancing transportation networks without needing land buyback schemes or disrupting existing cityscapes. By diverting the traffic, underground tunnels alleviate surface congestion, reduce travel times, and contribute to improved air quality by minimising vehicle emissions at the street level, contributing economically through shorter commutes and health benefits to cities and communities [3].

The benefits of tunnels are not exclusive to a civil construction context. Within mining, tunnels can provide access to deep ore deposits where open-cut mining methods are unsuitable. This is particularly important as resources close to the surface are depleting, requiring operations to reach greater depth to achieve the equivalent grade. Depending on the ore body, open pit mining can significantly increase in strip ratios, forcing some open-cut mines to transition to underground mining once they reach a certain tipping point where economic factors inform the decision.

The strategic importance of tunnels extends beyond their immediate utility for transport for cars and mining as they can play a role in disaster resilience, such as emergency routes for evacuation and emergency access. Two examples from Finland that may not come to mind to most people are the 50,500 bomb shelters in Finland, which are required under buildings hosting large numbers of people [4], and the Onkalo spent nuclear fuel repository, which houses spent uranium 430 metres belowground, deep in granite bedrock and encased in copper casks plugged with bentonite [5].

Advances in tunnelling technology have made construction more feasible and cost-effective, further driving the industry's growth as the pipeline of tunnelling projects in Australia allows an economy of scale. Cities across Australia will continue to grow well

into the 2050s as the Australian Bureau of Statistics shows Australia's population could reach between 30.9-42.0 million [6], leading to a long construction pipeline in all major cities regardless of whether it is public transport or road user tunnels. The impact this has on Australia's most populous city, Sydney, is that its pipeline of tunnelling construction will, in large parts, intersect with the Hawkesbury Sandstone that dominates the greater Sydney area, as shown in Figure 1 - Adapted Sydney Basin special geological map showing the Hawkesbury Sandstone distribution across Sydney (modified after Figure 1 [7]). The Western Harbour Tunnel alignment estimates that 87% of the boring material will be through sandstone, with the remaining volume through clay [8].


*Figure 1 - Adapted Sydney Basin special geological map showing the Hawkesbury Sandstone distribution across Sydney (modified after [7])*

Across the world, tunnels can be constructed through a variety of methods and cross-sectional shapes but will generally fit into these three main configurations:

1) Unlined tunnel – Generally constructed with drill & blast excavation as shown in Figure 2, an unlined tunnel. If the rock mass is stable on its own, then there may be no mesh and bolt support in the roof, however there is generally roof bolting and mesh installed in the roof to hold up the larger rock structure which is damaged in the excavation process. Similar applications occur in coal mining where development occurs quickly and the cost to reward of shotcrete lining is not financially beneficial.


*Figure 2 – Zambele unlined tunnel for road transport constructed in 1905 in Trento, Trentino-Alto Adige, Italy [9]*

2) Shotcrete–lined tunnel—This tunnel is generally constructed with drill and blast excavation followed by shotcrete lining, as shown in Figure 3. Shotcrete lining can help stabilise roofs and reduce the chance of smaller rockfalls.

*Figure 3 - Tunnel being lined with shotcrete in conjunction with anchor bolts and mesh reinforcement, Located in Houston, Texas, USA [10]*

3) Shield-lined tunnel—This type is generally constructed with a TBM, as Figure 4 of Melbourne's Metro Tunnel shows. Due to the accuracy of tunnel boring machines, precast concrete panels or "shields" can be installed behind the face of the TBM, with pumped concrete used to fill the gap between the excavated void and the tunnel rings.

*Figure 4 - Melbourne's Metro Tunnel construction with a TBM with reinforced concrete shield lining, Located in Melbourne, Victoria, Australia [11]*

The essential conditions that determine which construction method is appropriate will be a mixture of geology, design life, geotechnical investigation and budgets. In scenarios where these conditions are favourable, using a Tunnel Boring Machine (TBM) can yield a speed that is two to four times greater than that achieved through traditional drill and blast methods. However, this advantage must be carefully weighed against the time required for the TBM's setup and dismantling processes, as highlighted in the literature [12]. This choice can make sense for civil transport, where factors such as construction speed can play an essential role in funding approval. At the same time, a decline or drift in mining developments would likely not require a concrete shield lining in heading developments, given the design life is considerably shorter than a transport tunnel. This may lead to main entrances being afforded rock bolts and shotcrete when required for the life of the mine, whereas the development headings with shorter life spans may be reduced to simply rock bolts to support a roof.

When shield lining is concerned, the distance between the wall and the rock structure will change from tunnel to tunnel, depending on construction methodology and voids. Reinforced concrete shield lining sections currently testing by Victoria University are up to 300mm thick for civil tunnels in current Melbourne construction projects. [13]. Shotcrete applications for tunnel lining can be from 20-300mm thick [14], while unlined tunnels can be left as exposed rocks with no support or simply rock bolts.

In all contexts of tunnel construction, they are all generally aimed at facilitating transport. An in-depth analysis conducted by Larsson [15] scrutinised tunnel fire incidents and determined that a significant number of them involved heavy vehicles transporting non-dangerous goods. Yet, the fires emanating from these accidents were often on par with, or even more severe than, those originating from fuel tanker incidents. Larsson's findings indicate that a small percentage (6%) of tunnels lacked reinforcement, while the majority (61%) incorporated a blend of shotcrete and mesh for structural support. A notable portion (26%) featured sections reinforced with concrete linings.

The diversity in these tunnel linings translates into different responses to thermal shock during a fire. Tunnels equipped with any form of lining benefit from an added defence layer that mitigates the initial impact of thermal shock on the substrate rock and helps prevent thermal spalling. Despite these variations in design and reinforcement, each tunnel type shares the common challenge of being enclosed spaces where heat has limited escape routes. This fact underscores the importance of considering thermal dynamics outside of spalling testing and fire safety in designing and constructing tunnel linings, as they play a critical role in the structure's ability to withstand and respond to fire incidents.

Tunnel fires present significant hazards due to the enclosed nature of these structures, where heat accumulation can occur without sufficient avenues for dissipation. This situation accentuates the risk of heat-induced structural changes in tunnels, regardless of whether they are unlined or possess various lining levels. A notable instance illustrating this danger was the 1999 catastrophe in the Mont Blanc tunnel, where a fire resulted in 35 fatalities [16]. During this incident, temperatures soared to 1,000°C across a stretch of 700 yards (640 meters), demonstrating the intense heat build-up within such confined spaces. Despite one of the tunnel's refuge doors being designed to withstand fire for up to four hours, the blaze persisted for 50 hours [17]. In the year before the incident, the tunnel accommodated 766,000 vehicle passages, underscoring the point that even a single severe accident can lead to disastrous outcomes. This tragic event underscores the critical need

for robust understanding of how a fire impacts the tunnel as a whole system, given an unlined tunnel would experience spalling in the rock structure itself, while a shotcrete lined or shield lined tunnel would experience spalling in the concrete as a sacrificial layer, while the question of heat transfer into the rock mass as a whole is the research gap. s.

Promat [18] offers a detailed compilation of fire curves instrumental in simulating the swift escalation in temperatures characteristic of hydrocarbon fires. One specific curve, the RWS (Rijkswaterstaat) curve, is derived from the scenario of a 50m³ fuel tanker igniting, leading to a temperature increase to 1140°C within the initial five minutes and reaching a peak of 1,350°C [18]. The rate of temperature rise during these critical first five minutes is 228°C per minute, a figure in stark contrast to the more moderate heating rates of 5-20°C per minute that are typically discussed in existing literature. Prior studies on heating have primarily concentrated on examining the alterations in rock properties induced by the heating process, tailoring their methodologies to circumvent the extreme thermal shocks encountered during actual fires. Consequently, these studies do not fully encapsulate the impact of fires on rock structures, given the rapid and non-linear trajectory of temperature elevation experienced during real fire events.

This study will look to use the fire testing capability of Victoria University to simulate heat treatment with the Hydrocarbon Curve (HC), Modified Hydrocarbon Curve (MHC) and four linear heating rates (2, 5, 10, 20°C/min) to an equivalent peak temperature of the fire curves against non-treated rock samples as a control to understand how mechanical properties change after an incident involving fires.

## 1.1 Objectives

The proposed research addresses the following research questions:

1) How does the heating rate change Hawkesbury sandstone's mechanical properties?
2) What is the difference between linear and exponential heating on rocks when heated to an equivalent peak temperature?
3) What is the impact on the microstructure and mineralogy of rocks when heated at different rates and subjected to a simulated fire scenario?

In response to the above questions, this study aims to experimentally investigate the weakening of rocks after exposure to linear heating and realistic fires. The specific objectives are:

1) To experimentally study and quantitively describe the effect of fire exposure on the compressive and tensile strength and microscopic characteristics of Hawkesbury sandstone from Sydney basin, Australia.
2) To investigate the above changes of Hawkesbury sandstone for different specimen scales to establish a scaling law to extrapolate laboratory-scale results to field-scale.

## 1.2 Significance and Novelty

This study offers a foundational dataset that sheds light on how linear thermal heating and thermal shock following a simulated fire influence the mechanical properties of sandstone, a critical gap in knowledge given the absence of a globally recognised standard for evaluating tunnel fire damage. The dataset provided through this research compares the differential effects of heating rates on sandstone's mechanical behaviour, enhancing our understanding of thermal impacts at various scales. While the insights provided apply only to sandstone, they are relevant for unlined tunnels' design and safety assessment. Moreover, they offer potential value for evaluating the integrity of shield or shotcrete-lined tunnels when the linings are compromised and expose the rock surface.

Integrating mineralogical analysis and scanning electron microscopy enables a qualitative micro-scale examination in combination with macro-scale mechanical testing, including tensile and compressive strength assessments. Together, these methodologies paint a comprehensive picture of the potential risks that tunnel fires may pose to structural stability in sandstone. Together with the testing of the scale effect, the impact of heat treatment can attempt to be understood at scale, given the application to large rock masses in a tunnel. By advancing the available knowledge on this topic, the research contributes significantly to the field of geotechnical engineering, particularly in enhancing safety and design protocols for tunnel infrastructure subjected to high thermal stress.

## 1.3 Research Design

The research design adopted a quantitative systematic methodology to align with the established objectives. The experimental phase involved testing and analysing cylindrical samples of Hawkesbury sandstone prepared using diamond coring drill in the rock mechanics laboratory at Victoria University. The selected diameters—15mm, 32mm, 50 mm, 67mm, and 75mm—were chosen based on the equipment’s capacity, with the

sandstone sourced from a Sydney quarry at about a 20-metre depth selected for its uniform structure without visible discontinuities.

The research selected heating the specimens following the HC and MHC as fire curves, which peaked at 1,100°C and 1,300°C, respectively, to simulate the thermal shock caused by a tunnel fire. Linear heating rates of 2, 5, 10 and 20ºC/min up to the peak temperature of 1,100ºC were selected to isolate the heating rate as the variable most different from existing heat treatment literature and realistic fire simulations with the peak temperature in all tests being maintained for 1 hour. This peak temperature was determined by the HC and MHC treatments conducted in a commercial lab with a set peak temperature duration of 1 hour.

Once heated, the samples will be tested through UCS, indirect tensile strength, scanning electron microscopy, x-ray diffraction and digital image correlation to demonstrate quantitatively and qualitatively the changes made due to the different heating rates against untreated samples. The resulting data set will then provide insights into how, in combination with high temperatures, heating rates change quantifiable characteristics such as mechanical and chemical properties as well as qualifiable characteristics such as microscale fracturing.

The research posed deductive questions, which were analysed using multi-method experimentation. Research in heat treatment used the same or similar methodological approaches with a post-positivism worldview. The experiment results are meant to find objective data to compare variables with some qualitative data to support the explanation. The layers of the research onion metaphor were used to illustrate the proposed research approach clearly:

- Philosophies: Post-positivism worldview
- Approach: Deductive approach
- Strategy: Experimental analysis
- Choice: Multi-method
- Techniques and procedure: Data collection and analysis

Guidelines on how to carry out the lab testing were obtained through Australian standards.

With the above explanations, the below tests were conducted on the sandstone cores:

1. Uniaxial compression strength testing (UCS) – This is a test where stress is applied parallel to the long axis to find the compressive strength of the rock specimen [19]. The UCS tests were conducted at a displacement rate to ensure the test specimens failed between 2 and 15 minutes, as required by the ASTM Standard D7012-23 [20]. The standard followed was AS 4133.4.2.1-2007 [20]. The UCS was determined following Equation (3).

$$\sigma = \frac{P}{A} \quad (3)$$

where,

$\sigma_1$ = UCS, P = Peak axial load and A = cross-sectional area

2. Splitting tensile strength test (Brazilian method) - This is a laboratory test to indirectly determine the tensile strength of rocks by laying a core between two curved steel plates and compressing along the diameter [21]. The standard followed was AS 1012.10-2000 [22]. The final tensile strength was calculated using Equation (4).

$$\sigma t = \frac{2*P}{\pi*D*t} \quad (4)$$

where,

$\sigma_t$ = The tensile strength of the specimen, P = The peak axial load, D = The diameter of the specimen, t = The width of the specimen

3) X-ray diffraction (XRD) - This is a laboratory test that is a fast and reliable method using the diffraction of X-rays for the identification of the minerals and their quantities [23]. The testing was done through the XRD facility at the University of Melbourne in Melbourne, Australia.

4) Digital image correlation – Using an iPhone camera filming both the strength tests, the videos footages were cropped from the start of the test to failure, then processed through Ncorr v1.2 to visualise the evolution of strains during loading until the failure.

5. Scanning electron microscopy (SEM) – This is a laboratory test that will produce a cross-sectional image of the internal structures, microscale damage to existing grains and atomic composition of the specimens [24]. The testing was done at the Sem facility at Victoria University.

The results from the strength tests were then plotted in Microsoft Excel to analyse and contrast results. XRD results were shown in full and the crystallinity and quartz

percentages were plotted for discussion. DIC results were put into tables with 20% increments of stress between 0-100% to show progressive changes of strains until failure.

## 1.4 Thesis Structure

This thesis contains six chapters and an appendix. Below is a short description of each chapter:

Chapter 1: Introduction

This chapter provides an overview of tunnel structures and their increasing relevance in addressing traffic challenges in densely populated urban areas. It introduces the risks associated with using energy-intensive machinery in tunnels, including those powered by hydrocarbon fuels and emerging technologies like lithium-based batteries, which pose fire hazards. Examples of tunnel fire incidents are discussed, highlighting the discrepancy between the 4-hour fire resistance design of tunnel linings and the extended durations of real-world fires. The chapter also outlines this research's objectives, significance, and novelty, covered under the sections:

1.1 Objectives (including research questions)
1.2 Significance and Novelty
1.3 Research Design
1.4 Thesis Structure

All of which explains how the research defines the problem statements and overall methodology to investigate the thermal impact on sandstone specimens.

Chapter 2: Literature Review

The second chapter looks at the existing methods used to model the temperature that fires burn through a collection of fire curves from Europe. A comprehensive review of existing heat literature follows, which looks at many sandstone examples and existing trends noticed within the literature, which heats to temperatures lower than predicted for a realistic fire. Then, a comparison is made between the two bodies of data. The gaps are highlighted through the predictable, stable nature of experimental heating and the thermal shock experienced by combustion fires. The scale effect is examined to see the gap between smaller samples against the reality of a large rock structure that would be assessed with a real tunnel fire. Then, finally, a review of other applications where rocks may be exposed to fires through wildfires, underground coal gasification and geothermally active tunnels, which have some insights into varying heating situations.

Chapter 3: Materials and Research Methodology

The third chapter covers sourcing materials, preparation and testing methodology for the Hawkesbury sandstone.

Chapter 4: Experimental Results and Discussion

The fourth chapter discusses the results of the tensile and compression strength testing for the selected heating rates and varied diameters. These have been plotted and contrasted to demonstrate the relevant outcomes. The SEM and XRD results are included to show the changes in microstructure and mineral composition.

Chapter 5: Conclusions and Recommendations

This chapter summarises the key findings of the research, integrating insights from the experimental work, SEM, and XRD analyses. It outlines practical recommendations for future studies and discusses potential applications of the research in geotechnical engineering. Emphasis is placed on exploring tunnel configurations to enhance safety and design considerations for underground infrastructure.

# 2. Literature Review

This chapter discusses previous research on existing methods to model fires, existing heat treatment research, contrasts between the two data sets, the scale effect in rocks, as well as other pertinent topics where rocks are exposed to heat for long periods, such as wildfires, underground coal gasification and geothermally active tunnels.

## 2.1. Fire Curves

Promat provides a helpful summary of international fire curves for fire safety design, shown in Figure 5 [18]. This selection of fire curves shows rapid heating acceleration rates within the first 5 minutes of heating, similar to an accident with a fuel source leading to a fire with various scenarios. RABT ZTV curves were developed in Germany with linear heating rates, plateaus for 25-55 minutes, followed by linear cooling for 110 minutes, possibly to simulate firefighting. The RWS curve is modelled off 50m$^3$ of fuel, similar to a fuel tanker, which could last up to 120 minutes. Results were based on testing in the Netherlands in 1979 and reconfirmed with full-scale tests in the Runehamar tunnel in Norway [25]. MHC was a French regulatory request to alter the original HC after the Mont Balance tunnel tragedy in 1999, which led to 39 deaths [26]. The modification intentionally captured the heat change rate within confined spaces such as tunnels, which can peak at 1300 ºC. All the below fire curves can be recreated during testing with Victoria University's fire testing facilities [13].

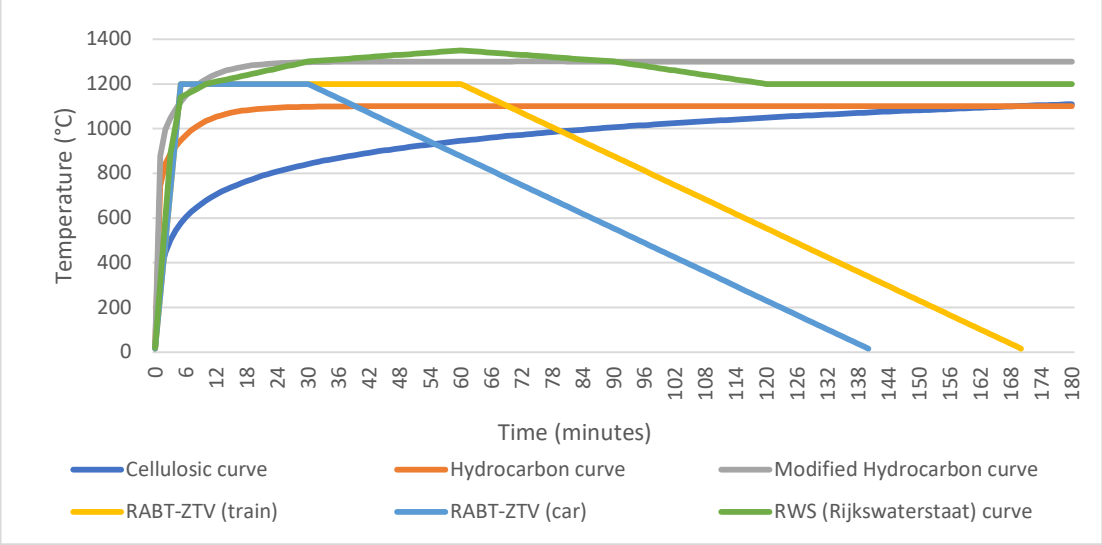


*Figure 5 – A collection of international fire curves from the Promat website (modified after [18])*

## 2.2. Effect of High Temperature on the Mechanical Behaviour of Rocks

Several researchers have investigated the effect of elevated temperature on the mechanical properties of various rocks in the literature, as shown in Table 1. Wasantha et al. [27] conducted a review of the existing literature on topics related to tunnel fires and found that there are only a few studies that investigated the effect of fire on the rock behind the tunnel lining. Promat's international fire curves [18] in Figure 5 shows all fire curves achieving ~1,000°C with rapid heating rates in the first 10 minutes, while the collection of existing heat treatment studies in Figure 6 heat at rates of 2-20°C/min. Only a very few studies meeting or exceeding 1,000°C but at rates that take many more hours than the fire curves [28-31].

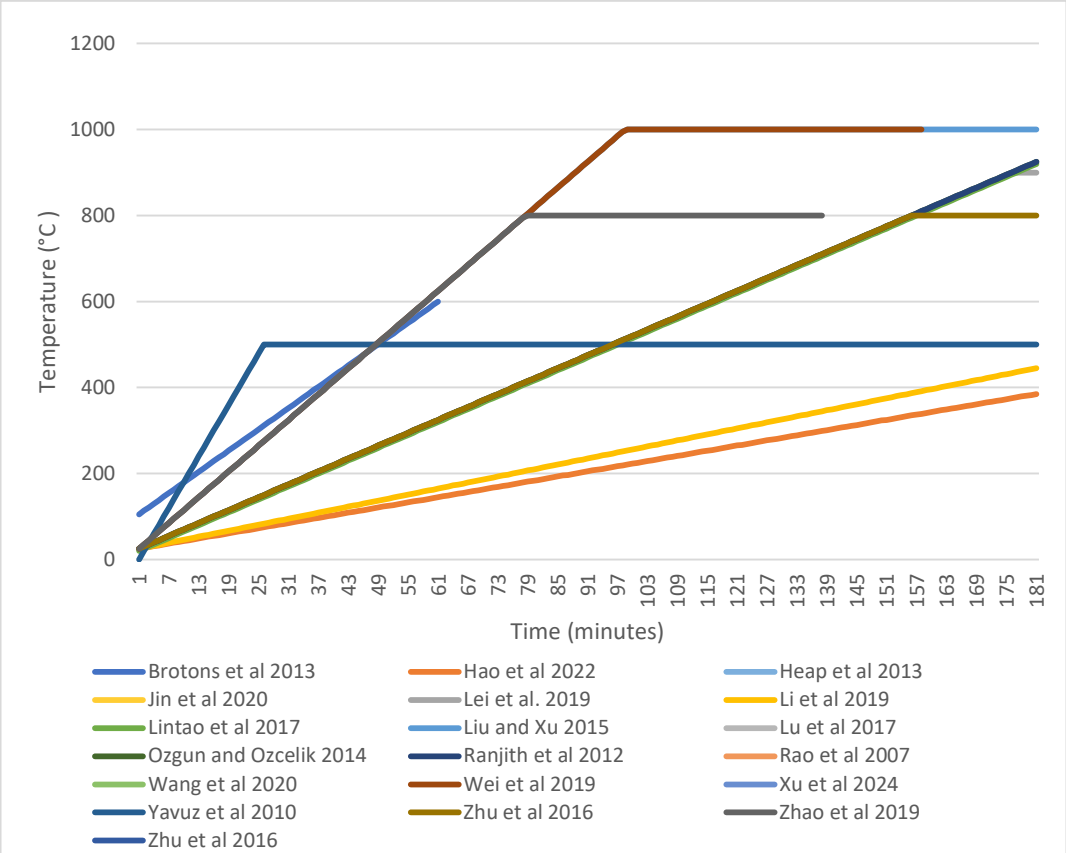


*Figure 6 - Fire treatment experiments with the highest temperatures shown*

Brotons et al. [32] tested San Julian's calcarenite from Alicante, Spain, a type of limestone, to temperatures between 105-600°C within 60 minutes, starting in a kiln at 105°C. UCS results were reduced by up to 35% for air-cooled samples and 50% for water-cooled samples at 600°C. Similar trends occurred with slake durability index testing, Young's modulus and Poisson's ratio when comparing air-cooled and water-cooled,

showing that cooling intervention from water, which would help resolve fire incidents but at the cost of the cross-sectional stability of the tunnel.

Hao et al. [33] tested sandstone at temperatures between 150-900°C, with peak temperatures being maintained for 2 hours once reached. They used a heating rate of 2°C/min. Testing of the treated samples showed mechanical properties peaked at 300°C then reduced after that. The mineral composition changed most between 600-900°C with water vapour being released, which was reflected through volume changes and reductions in wave velocity with acoustic testing.

Lei et al. [34] investigated sandstone from Jiulongpo, Chongqing, China, with temperatures between 25-900°C. Samples were heated at a rate of 5°C/min, then slowly cooled (rate not specified). Colour changes are evident in all treatments above 200°C. A change of colour to a brighter shade of orange was observed up to 600°C. Compressive strength increased up to 200°C and decreased from 400°C onwards. XRD analysis showed a 17.6% clay in the sandstone composition, and the decrease in strength occurred sooner than in other studies. These mechanical property changes aligned with the change in porosity percentage after temperature treatment.

Li et al. [35] tested andesite rocks after heating at a rate of 2.3°C/hr to peak temperatures between 500-1100°C. Peak temperatures were maintained for 2 hours, and results were measured with triaxial shear testing and p-wave testing. Their results showed some consolidation due to the presence of clay content, leading to a minor increase in strength with the 500°C samples, though this did reduce with the higher temperature treatments.

Liu and Xu [29] tested granite and sandstone under a variety of temperatures between 100-1,000°C. Heating rates were well below a HC or MHC fire curve but showed that as peak temperatures increased, there was a reduction in strength. This result differed between the two rock samples for the reduction of stress/strain testing but showed a decline regardless. For temperatures between 400-600°C, there was an increase in density, which is consistent with other previous studies discussed, showing that consolidation plays a key role within those temperature ranges but then shows the opposite, i.e., a reduction of density with higher temperatures. It is clear from the experiment that structural changes occur with increases in cracking, with more brittle characteristics becoming evident.

Lintao [36] used sandstone samples from an underground coal gasification site in Poland for high-temperature treatments, followed by triaxial tests and x-ray scanning to validate results. Observations were made that water evaporated below 400°C, leading to increased density and minor increases in strength, and temperatures between 400-800°C leading to increases in volume and cracks increasing within the sample. Finally, the temperatures >800°C samples began to show melting and thermal decomposition occurring, which lead to reductions in rock strength. This study shows similar insights to Li et al. [4] for consolidation, however, this appears to be irrelevant at temperatures >800°C, which will be the range that hydrocarbon fires create. Therefore, the reductions in strength and volume changes may be applicable to tunnel fires.

Ranjith et al. [37] conducted UCS testing on Hawkesbury Sandstone for temperatures in the range of 25-950°C. Samples were heated at a rate of 5°C/min and kept at the peak temperature for 2 hours. Heat treatment up to 600°C led to an increase in UCS strength, which was then reduced at higher temperatures. The Elastic modulus peaked at 400°C then reduced rapidly.

Jin et al. [38] investigated sandstone from the Hanzhong area of Shaanxi Province, China, where specimens were subjected to heat treatment up to a maximum of 800℃ with a heating rate of 5℃/min. Maximum temperatures were maintained for 2 hours; then, cooling was done through natural airflow and cooling in 100L of 25℃ water for 8 hours. Their investigations revealed differences in mechanical properties depending on the cooling method applied. Naturally cooled samples did not show a continuous decrease in strength with temperature increase, unlike those subjected to water cooling, which is effectively thermal shock, where a more substantial reduction in strength was observed. Axial strains increased from 0.2% up to 1.1%, while compressive strengths reduced from 50MPa untreated, up to 56MPa at 300°C then down to 17MPa at 800°C, marking a ~66% reduction from highest to lowest values. Notably, above 500°C, water cooling significantly increases the widening and expansion of cracks, while above 800°C, the pore size increases, and fractures develop into networks that substantially increase water permeability. These applications have interesting ramifications for firefighting interventions or any sudden releases of water under the surface.

Wei et al. [31] focused on course sandstone from a coal seam roof, with a maximum temperature of 1,000℃ with a heating rate of 10℃/min. Maximum temperatures were maintained for 4 hours, with cooling occurring naturally in the furnace. For acoustic

testing, there is an inverse correlation between increasing temperatures and decreasing wave velocity caused by the heating damage, which is up to 53% above 500℃. With UCS testing, however, heat treatment had a strengthening effect on compressive strength and a decrease in deformation under load. Triaxial rock strength is positively correlated with temperature increases and confining pressure up to 800℃ when the confining pressures are lower than 15MPa, which then matches the theoretically calculated value. This observation does not continue with higher confining pressures. Colour changes were observed in the two colours of sandstone tested which continued to change with increasing temperatures. Strength increases peaked around 500℃ and then began to decrease while axial strain increased.

Rao and Wang [39] examined sandstone samples for their tensile strength up to 300°C with heating rates of 30 ℃/min with peak temperatures maintained for 2 hours. A linear increase in tensile strength and elastic modulus was observed in samples up to 250°C, beyond which these properties decreased. Their work suggests a critical threshold for thermal damage in sandstone, which aligns with observations of other researchers regarding thermal thresholds, however, at a considerably lower temperature than the other studies referenced.

Lu et al. [40] investigated sandstone from Linyi, Shandong, which was treated at 50°C increments from room temperature up to 900°C at a rate of 30℃/min with a maximum temperature of 900°C maintained for 30 minutes. Samples were naturally cooled and tested for their tensile strength. The samples underwent 4 clear stages of strength reduction starting from room temperature and reductions starting from 50°C samples. Longitudinal wave velocity, which demonstrates internal cracking, showed a downward trend across all temperatures. However, this was dissimilar to the tensile strength results and did not have clear stages. Chemical changes occurred up to 300°C with free and combined water escaping, 300-600°C showed an expansion of quarts, 600-800°C showed the start of minerals melting then from 800°C above, macro fissures were visible across the surface of the samples. The constant reduction in tensile strength is dissimilar to other tests, which either maintain strength in compression or increase up to 500°C then decrease afterwards.

Wang et al. [41] investigated sandstone from the upper layer of the coal seam of the Taiyuan-Shanxi Formation in the Ordos Basin, China, with a maximum temperature of 1,000°C heated at 5°C/min and maintained for 2 hours at peak temperature. Samples were

cooled at a 0.3°C/min rate in the furnace. Samples tested were rectangular prism blocks with colour changes from grey to red with temperature increases. The outer surfaces appear smooth without visible pores, joints, or macroscopic fissures up to 1,000°C, where fissures parallel to the longest length appear in the face. Peak temperatures increased up to 800°C then reduced by almost half at 1,000°C. Up to 800°C stress-strain curves show a clear post-peak stress reduction section indicating brittle behaviour. XRD testing shows massive reductions in clay and other trace minerals past 600°C and quartz going from 33% to 90% in the 1,000°C sample. SEM also shows that intergranular cracks caused by high temperatures are the main way microcracks propagate.

Zhu et al. [42] investigated sandstone heat treated at temperatures up to 800°C at a rate of 5°C/min with peak temperatures maintained for 50 minutes. at each temperature, 2 or 3 intact sandstone samples and 5 kinds of flawed samples containing a pre-existing single fissure at angles of 15°, 30°, 45°, 60° and 75° respectively, were tested. All samples increased in UCS up to 400°C then decreased towards 800°C. At the same temperatures, the failure modes of samples changed with increasing fissure angles. When the angles increase from 15° to 75°, the failure mode transitions from tensile and shear crack mixed failure to shear crack failure. Temperature and fissure angles had a strong influence on failure modes.

Xu et al [43] investigated sandstone from Rizhao, Shandong Province, China, heat-treated at temperatures up to 750°C at a rate of 10°C/min and maintained for 2 hours. Samples were cored to specifically intersect bedding planes at 0°, 30°, 45°, 60° and 90°. One extra sample tested for rapid cooling in a water bath which was 25°C for 2 hours. XRD testing showed no significant mineral composition changes up to 300°C and changes from 450°C above. Cooling intervention exacerbated internal cracks due to the thermal shock created with cooling intervention. Peak axial strain gradually rises as the temperature increases but decreases then rises again as the dip angle increases. Dip angle and temperatures affected the failure modes of all samples. Maximum UCS values increased as temperatures increased up to 600°C then decreased at 750°C in all samples tested. This shows the impact of temperature being influenced by changing geology, such as discontinuities playing a part in how temperature impacts sandstone.

Heap et al. [44] conducted a comprehensive study on the thermal behaviour of high-strength concrete made in a laboratory setting. The concrete samples were incrementally heated to temperatures ranging from 100°C to 1000°C, with a consistent rate of 1°C/min,

and maintained at peak temperatures for one hour. Controlled cooling was also applied at a rate of 1°C/min. UCS and tensile strength tests progressively declined in mechanical strength properties as temperatures increased, with microcracking observable at 180°C. Axial strain decreased up to 200°C but then increased with all temperatures up to the maximum tested, indicating a shift from brittle failure mechanisms at lower temperatures to more ductile behaviour as temperatures approached 1000°C. At this upper limit, UCS was reduced by 96% and tensile strength by 94%. Photomicrographic analysis displayed the evolution of microstructural damage, showing initial visible crack formation at 300°C and a transition to a porous, "sponge-like" texture at higher temperatures. Chemical analysis further indicated significant transformations, including dehydroxylation occurring between 440°C and 480°C.

Ozgun and Ozcelik [45] explored the thermal effects on eight commonly used building stones in Turkey, including four types of limestone and four types of marble, by subjecting them to temperatures ranging from 25°C to 1000°C. These samples underwent heat treatment at a rate of 5°C/min and were allowed to cool naturally after maintaining each target temperature for one hour. The study assessed changes in unconfined compressive strength (UCS) and tensile strength alongside other physical properties like water absorption by capillarity and density variations. Findings indicated an increase in water absorption beginning at 400°C, attributed to microscale cracking within the stone structure. While the density of samples showed minimal variation across different rock types, an overall decrease in density was noted with increasing temperatures. Both limestone and marble samples displayed a slight increase in compressive strength up to 400°C in some samples, followed by a general reduction in strength up to 1000°C. This pattern was mirrored in the tensile strength results with similar reduction curves, though not identical.

Zhao et al. [46] investigated the thermal effects on failure characteristics of granite from Shandong Province, China with pre-existing fissures. Samples were heated between 100-800°C at a rate of 10°C/min. UCS testing found no change in strength below 400°C, with strength rapidly decreasing afterwards up to 800°C. The failure mode changes at the 600°C heating point with observations that pre-existing fissures influence the strength of granite. Of the samples tested, there was no difference found when comparing the thickness of the granite sheets between 16 and 29mm.

Zhang et al. [47] investigated granite and sandstone samples from Shandong province, Eastern China and were heated to temperatures between 25-500°C. Heating was done at a rate of 5°C/min, maintained for 2 hours, and then cooled down at the same rate. The granite was shown to decrease in mass between 100-300°C while exponentially increasing in volume from 100-500°C. The porosity of the sandstone increased from 7.8 to 9.5% between 100-500°C for sandstone. The overall testing showed an inverse relationship between porosity and wave velocity through ultrasonic testing as temperatures increase, implying an increase in pores expansion and increased crack density, leading to reductions in compressive strength.

Yavuz et al. [48] investigated the behaviour of carbonate rocks from various locations in Turkey heated to temperature ranges of the 100-500°C range, which also heated at a rate of 20°C/min, which is the highest of all the studies referenced. Interestingly, the temperatures were maintained for 1-6 days, but negligible variations in strength testing results were observed after the 1-day mark, indicating the peak damage occurred within that 24-hour window. The results of the study showed a correlation between porosity and resulting increase in crack density, which indicates that porosity could exacerbate thermal shock with faster heating rates.

Table 1 summarises the studies by their authors, rock types, temperature tested and heating rates .

*Table 1 - Summary of the heat treatment conditions used in some relevant previous studies*

| Study | Rock type and origin | Start Temperature (°C) | Peak Temperature (°C) | Temperatures Tested (°C) | Heating rate (°C/min) |
|---|---|---|---|---|---|
| Brotons et al 2013 [32] | Calcarenite (Limestone) - Alicante, Spain | 105 | 600 | 105, 200, 300, 400, 500, 600 | 1.6, 3.3, 4.9, 6.6 and 8.3°C/min (temps reached in 60 minutes) |
| Hao et al 2022 [33] | Sandstone - Location not specified | 25 | 900 | 25, 150, 300, 450, 600, 750, 900 | 2°C/min |
| Heap et al 2013 [44] | High Strength Concrete - Lab made | 100 | 1000 | 100, 200, 300, 500, 750 and 1000°C | 1°C/min |
| Jin et al 2020 [38] | Sandstone - Hanzhong area of Shaanxi Province, China | 25 | 800 | 25, 100, 300, 500, 600, 800 | 5°C/min |
| Lei et al. 2019 [34] | Sandstone - Jiulongpo, Chongqing, China | 25 | 900 | 25, 200, 400, 600, 800, 900 | 5°C/min |
| Li et al 2019 [35] | Andesite - Guadeloupe, Caribbean, France | 25 | 1100 | 500, 800, 930, 1100 | 2.33°C/min |
| Lintao et al 2017 [36] | Sandstone - Wieczorek Mine, Katowice, Poland | 20 | 1000 | 20, 400, 800, 1000 | 5°C/min |
| Liu and Xu 2015 [29] | Granite & Sandstone - Qinling Mountains, China | 100 | 1000 | 100, 200, 400, 600, 800, 1000 | 10°C/min |

| | | | | | |
|---|---|---|---|---|---|
| Lu et al 2017 [40] | Sandstone - Linyi, Shandong province | 25 | 900 | 25, 50, 150, 200, 250, 300, 350, 400, 450, 500, 550, 600, 650, 700, 750, 800, 850 and 900°C | 30°C/min |
| Ozgun and Ozcelik 2014 [45] | Limestone and marble - Turkey | 25 | 1000 | 25, 200, 400, 600, 800, 1000°C | 5°C/min |
| Ranjith et al 2012 [37] | Sandstone - Hawkesbury, Sydney AUS | 25 | 950 | 25, 200, 400, 600, 800, 950 | 5°C/min |
| Rao et al 2007 [39] | No location given | 25 | 300 | 20, 60, 100, 150, 200, 250, 275 and 300°C | 3°C/min |
| Wang et al 2020 [49] | Upper layer of the coal seam of the Taiyuan-Shanxi Formation in the Ordos Basin, China | 20 | 1000 | 20, 200, 400, 600, 800 and 1000°C | 5°C/min |
| Wei et al 2019 [31] | Course sandstone from a coal seam roof - no location given | 25 | 1000 | 25, 100, 200, 300, 400, 500, 600, 700, 800, 900, 1000 | 10°C/min |
| Xu et al 2024 [43] | Sandstone - Rizhao, Shandong Province, China | 25 | 750 | 25, 300, 450, 600 and 750°C | 10°C/min |
| Yavuz et al 2010 [48] | Marble, Travertine and Limestone - Various locations in Turkey | 100 | 500 | 100, 200, 300, 400, 500 | 20°C/min |
| Zhang et al 2016 [47] | Granite & Sandstone - Shandong Province, China | 25 | 500 | 25, 100, 200, 300, 400, 500 | 5°C/min |
| Zhao et al 2019 [46] | Granite - Shandong Province, China | 100 | 800 | 100, 300, 400, 500, 600, 700, 800 | 10°C/min |
| Zhu et al 2016 [42] | Sandstone - not stated | 25 | 800 | 25, 200, 400, 600 and 800°C | 5°C/min |

## 2.3 Experimental Heating Versus Fire Curves

A key gap in the existing literature is the difference between the fire curves constructed to represent temperature versus time variation of actual fires and the heat treatments undertaken with kilns. Figure 7 plots six fire curves in red, as shown in the Promat fire curve [18] and a sample of 19 relevant heat treatment papers discussed in this literature review in blue. The modified MHC, RWS curve and RABT-ZTV (car) exceed 1,000°C in 3, 4 and 5 minutes, respectively, which is a heating rate of ~200-333°C/min, while the majority of heat treatment studies have been done between 2-20°C/min. This difference makes for an unreliable comparison when looking to understand the impacts of tunnel fires on rocks where a thermal shock with rapid heating rates occurs.

As shown in Figure 7, the rates of acceleration are not comparable to accurately capture how thermal shock will affect the rock specimens. Research has been conducted on thermal shock, and the resulting spalling in concrete is a well-understood mechanism such that it is included in Australian Standards 3600:2018 Concrete Structures [49] with minimum depths for reinforcement. However, this is not a fair comparison as the

production of concrete is a homogenous mixture, and rock formations are natural and not as chemically consistent.

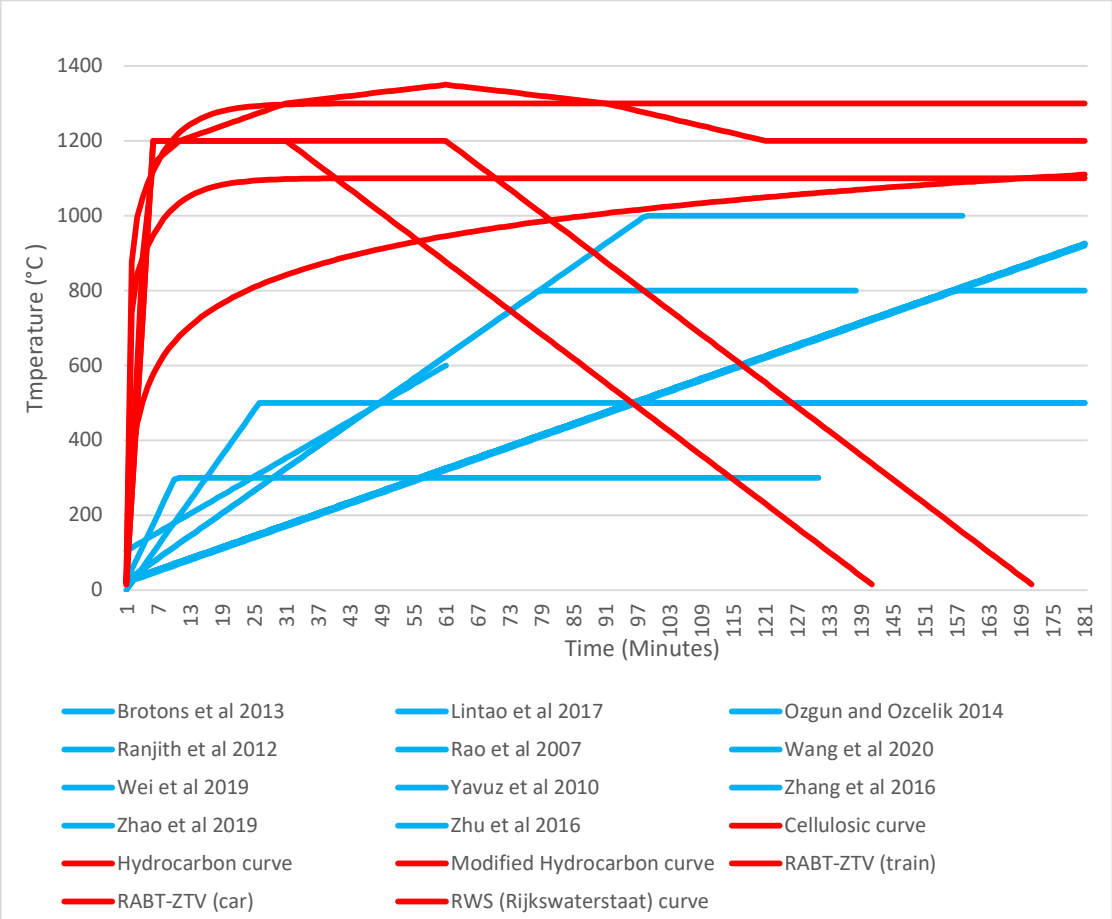


*Figure 7 – Comparison between existing heat treatment studies and international fire curves*

## 2.4 Scale Effect In Rocks

Geologists and geotechnical engineers often use exploration drill hole data to inform their geological and geotechnical models, which are typically obtained using NQ (47.6mm) or HQ (63.5mm) cores [50]. These core sizes are often used for lab testing to understand large parts of the rock strength understanding. Han et al. [51] compared 300mm diameter cores with varying compacted aggregate particle sizes between 20-60mm, which showed larger 60mm aggregate led to higher internal angles of friction and, therefore, higher strength samples. Rusnak and Mark [52] investigated point load testing to find UCS and this can be conducted with varying sample sizes with Pressure = Force/Area being used for scaling of results with a resulting correction factor to compare against standard 50mm samples. Thuro et al. [53] found that core diameters only had a marginal effect on resulting strength values for limestone, while the modulus of elasticity increased for

kersantite and tensile strength decreased for limestone with length-to-diameter ratio. This study appears to roughly replicate findings from Ergun and Hasancebi [54], showing UCS results did not make significant changes for marble and limestone between length/diameter ratios of 1-2.5, while other rocks such as Basalt and Grey Andesite had more significant reductions in UCS strength.

For a practical application of how to test if the results match a scale effect, Hoek and Brown [55] the scale effect of UCS strength can be tested against the value of the 50mm diameter sample with the below formula:

$$\sigma_{cd} = \sigma_{c50} \left(\frac{50}{d}\right)^{0.18} \quad (1)$$

This has been shown to apply to many rocks such as marble, limestone, granite and basalt to name a few. Walton [56] tested this against stanstead granite at diameters of 43, 63 and 75mm with results lining up to the above formula.

However, Pells [59] conducted tests specifically on Hawkesbury sandstone, which provides valuable insights for this study. Sample rocks were Hawkesbury sandstone, with cores tested at diameters from 18mm to 144mm in West Pymble and two samples at 17mm and 50mm drilled from Gosford quarries. The West Pymble samples demonstrated increased strength at larger diameters, ranging from 25.3MPa to 31.1MPa, contradicting the scaling proposed by Hoek and Brown. In contrast, the Gosford quarry samples did not provide enough data to confirm a scaling trend, as the 17mm sample was 0.8MPa stronger than the 50mm sample. Pells notes that the rock types available to Hoek and Brown were igneous or crystalline and, therefore, contain microcracks, which may explain the size-dependent strength observed in those cases but not Hawkesbury sandstone, a sedimentary rock.

These findings underline the importance of considering specific rock properties and conditions when applying scaling models, as discrepancies may arise due to inherent differences in rock composition and microstructural characteristics.

## 2.5 Other Applications of Rocks Exposed to Fire

### 2.5.1 Wildfires

Wildfires in forests have the potential to create conditions for rock weathering and thermal spalling [57]. Blackwelder [58] was one of the first to investigate the damage in the Rocky Mountains, which have historically been ravaged by forest fires. Observations

were made that cracking occurred parallel to the surface and was influenced by rock types and discontinuities. Experimental testing of various rock types was undertaken with a kiln to recreate conditions similar to the intensity of forest fires reaching up to 880ºC with both rapid cooling through rainfall and slow cooling with no natural intervention. Test conditions were not identical for all rock types but generally showed heating to 200-300ºC with rapid cooling led to no real changes, while higher temperatures with rapid cooling led to shattering with some samples. Higher peak temperatures at slower heating rates lead to superficial changes to the rock and one crack along an existing discontinuity. Buckman et al. [59] attempted to quantify the volume of rock spalling due to wildfires in central Australia through field observations. The assessment provides in equation 1 an erosion rate is due to fire spalling as a function of the area of rock surface affected by fire spalling as a percentage of total surface area (A), the thickness of the spalled sheet (W) and the annual fire recurrence (t) in the surrounding area.

$$E = \frac{W*A}{t} \quad (2)$$

Resulting erosion rates showed wildfires have led to a 64 times greater magnitude of erosion when compared to other non-fire-related weathering processes. While this is not exactly the same as a hydrocarbon fire, it shows that fires pose a risk to rock structures that are not contained within a tunnel, with outside factors such as rain and wind impacting wood-fuelled fires.

Goudie et al. [57] explored fire weathering's impact on the modulus of elasticity through a methodical approach with variable control across seven rock types at ten different temperatures between 50-900ºC with two combinations of cycles (1 & 5 cycles total) to simulate savannah and shrubland fires reaching a typical 500-800ºC. Through furnace testing and a grindoscopic apparatus for validation, seven stones were treated with a furnace temperature of 500ºC for 5 minutes for various durations. Significant decreases in elasticity were observed at temperatures as low as 200ºC. Samples exposed to longer durations of heat treatment reduced the elasticity further, with some showing reductions after 1 minute, except for slate, which had negligible changes. Yorkstone, a weakly foliated arkosic sandstone, showed an increase in strength up to 400ºC, which may indicate some consolidation within samples; however, rock specimen changes in volume were not measured.

### 2.5.2 Underground Coal Gasification

Underground coal gasification (UCG) represents an innovative approach to accessing coal deposits that are not economically feasible to mine using conventional methods. This technology involves the in-situ conversion of coal into syngas by injecting oxidants and steam to initiate high-temperature chemical reactions within the coal seam (Figure 8). The process can reach temperatures up to 1500°C, facilitating sulfidation and oxidation reactions that transform coal into a combustible gas mixture while still underground [60]. The design of injection wells is critical, as they must endure significant thermal and mechanical stresses. Although these wells are engineered to withstand extreme conditions, the surrounding coal deposits may not be thoroughly characterised, posing a risk of unpredicted behaviour. Water injection at temperatures below 350°C (sparging) is part of this procedure, aimed at managing the thermal dynamics within the gasification zone [61]. The intense heat from the UCG process can compromise the integrity of adjacent rock layers, potentially leading to surface subsidence—a consequence of the structural weakening induced by the high temperatures.

Stephens [62] analysed the relationship between temperature and syngas composition using data from the Lurgi gasification process. Findings indicate that temperatures above 1200°C can enhance hydrogen yield within the syngas, aligning with the industry's optimal operational temperature threshold of 1,000°C to optimise the gas composition [60]. During maintenance shutdowns, the residual heat from the accumulated hot debris within the gasifier continues to affect the surrounding geological structures, potentially impacting the overburden's stability over time [61].

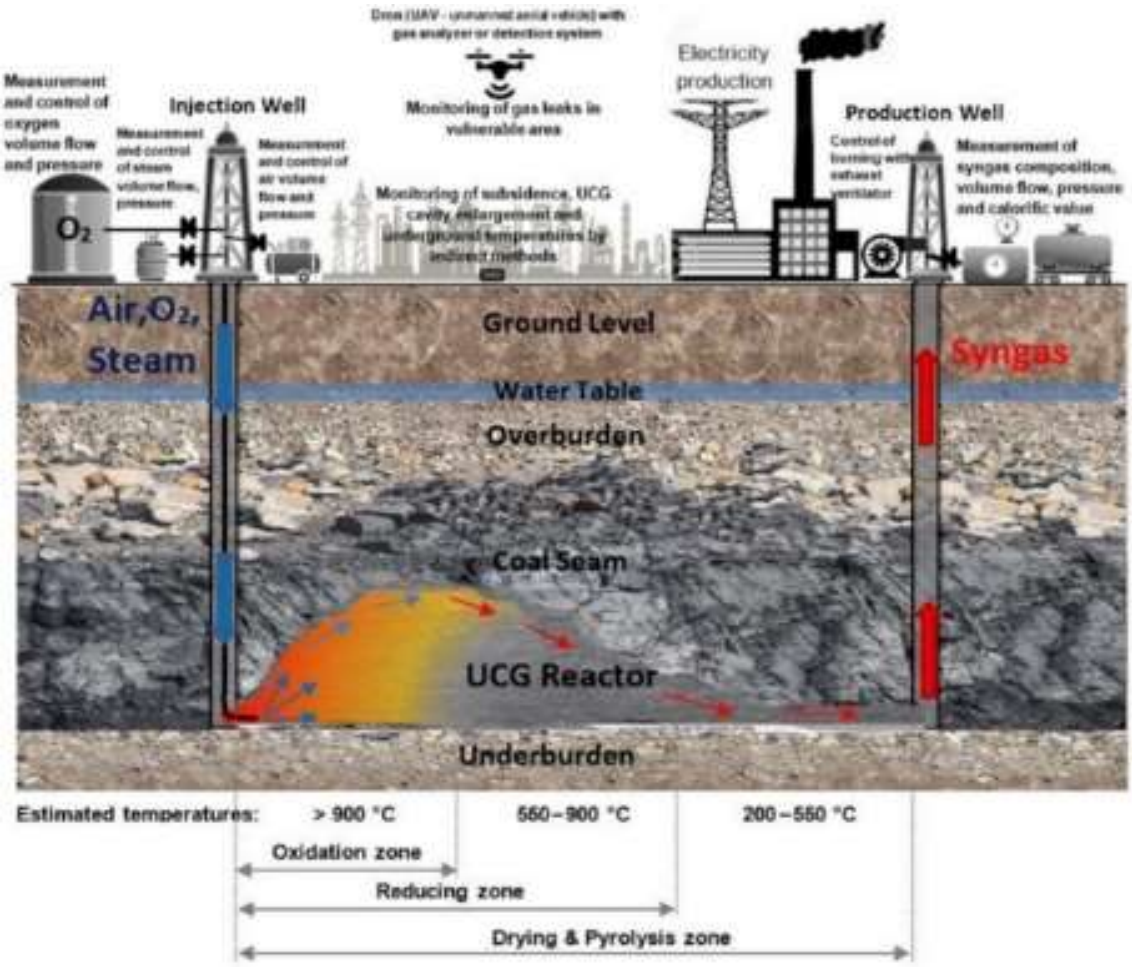


*Figure 8 – A schematic diagram showing the underground coal seam gasification process (From Laciak 2021 [63])*

Integrating new insights, the Leigh Creek coal gasification project exemplifies the application of UCG technology on difficult-to-access coal deposits situated at depths between 200m and 1,100m. With a planned operational lifespan of 30 years, this project aims to convert solid coal into syngas efficiently at temperatures exceeding 900°C, demonstrating the process's feasibility for deep-seated coal resources [100].

The energy yield of syngas is influenced by the type of coal used. For instance, lignite, with an energy content of 17-18kJ/t, and anthracite, at 32-33kJ/t, produce syngas with varying energy efficiencies. This variation underscores the importance of selecting appropriate coal types for UCG to optimise the energy output of the produced syngas [64].

Life cycle assessments, as detailed in the study on coupled UCG and $CO_2$ capture and storage, highlight that lignite, despite its lower energy content, can yield syngas with

relatively high energy efficiency when processed through UCG, suggesting an advantage in using lower-grade coal for this technology [65].

Subsidence remains a significant concern in UCG, with research advocating for a minimum of 15m of consolidated rock above the coal seam to mitigate such risks. The integrity of the overlying strata and the surrounding impermeable rocks is crucial to prevent gas escape and water ingress, thereby enhancing the process's environmental and operational safety [66]. Moreover, optimal coal seam depths have been identified between 92 and 460 m to minimise subsidence risks, emphasising the preference for deeper seams [66].

Furthermore, the interaction of UCG with surface and groundwater resources is notable, as subsidence can alter hydrological dynamics, potentially increasing water usage and contaminant release, highlighting the need for comprehensive environmental monitoring and management strategies in UCG projects [67].

In summary, UCG offers a promising alternative for utilizing deep-seated or otherwise inaccessible coal deposits with an example of coal production using heat for extraction, potentially over a well life of >20 years. Its structural and geological impacts necessitate careful consideration for the extraction method, which is in limited use and would provide considerably high sub-surface temperatures for a period even longer than tunnel fires, potentially as an area to study and measure the impact of sustained heating on adjacent rock structures, however, the sample size of this and the body of data testing these adjacent structures is not available. The risk of inrush from underground aquifers provides a thermal shock risk from hot production wells, with water potentially cooling down the well once it is breached.

### 2.5.3 Geothermally Active Tunnels

Wang et al. [68] provides some understanding of how temperatures change with in situ rock in underground tunnels from the case study in a high-geothermal tunnel. The researchers found that temperatures were initially around ~70°C and reduced to a stable 35°C after 14 days. Observations were made with drill holes measuring temperatures at set distances into the adjacent rock. While this scenario did not target fires, it does look at heating decay rates for natural rocks and could show some insight into the cooling rate of samples. However, this does not appear to be a strong enough understanding to apply to the cooling rates for rock specimens treated by fire, which are likely to be cooled with

water or other firefighting systems. A contrast could be made with rock samples that cool at room temperature versus samples that cool with intervention.

## 2.6 Summary

The literature review shows that while there is a large body of research demonstrating varying heat rates on rocks, inclusive of many sandstone-based studies, this is not easily translated into the application of a tunnel fire caused by a hydrocarbon, or similar fire. Work has been done to provide formulae which can assist in modelling, however, there is still a gap between the two.

There is a limitation on how these varying rates would apply to a real tunnel cross-section, however, the linear rates between 2-20ºC/min and the exponential fire curves will provide and understanding as to the impact that heating rate, rather than just peak temperature, changes the mechanical properties of sandstone.

The literature review shows that there is a clear trend within sandstone that samples change volume and generally reduce in strength when heated, but there is still a significant gap in how rock adjacent to tunnels is likely to react and how thermal shock impacts most rock types.

Analysis and comparison between the linear and exponential heating rates will help in terms of understanding how this works thoroughly for sandstone as well as testing the scale-effect, which is key to understanding whether these results could translate to a larger forensic structural analysis of a tunnel impacted by a fire.

# 3. Materials and Research Methodology

## 3.1 Collection of Materials

Sandstone was sourced from a quarry in Gosford, Sydney, New South Wales, Australia. The blocks were delivered to the Victoria University, Footscray Park Campus for storage and testing. The sandstone was delivered as pre-cut cubes, and they were all visually homogenous.

## 3.2 Sample Preparation

Upon arrival at the laboratory, cylindrical specimens were cored from the blocks using a handheld diamond drill mounted into a drill press at the rock mechanics laboratory, Footscray Park Campus, Victoria University. Drilling was performed to create cores in five diameters: 15mm, 32mm, 50mm, 67mm, and 75mm, from the available diamond drill hole sizes which were then used for subsequent testing phases. For each combination of heat treatment protocol and core diameter, three specimens of each diameter were prepared for UCS testing. An additional set of 50mm diameter cores was also prepared for tensile strength analysis, with three replicates for each heat treatment case considered. The lengths of the cores for compressive strength testing were cut to twice their respective diameters, and for tensile strength testing were cut to half the diameter, after which they were labelled, as the typical specimen set illustrated in Figure 9. To comply with the relevant standards, the end surfaces of the cylindrical samples were ground and smoothed that provide a flat surface for compression testing.

*Figure 9 – Various diameter core samples for both UCS and tensile testing*

## 3.3 Heat Treatment

Heat treatment of all specimens was conducted at Victoria University's Werribee campus. The HC and MHC fire curves were selected for their exponential heating rates, which most accurately simulate the conditions of an accidental and hazardous fire scenario. The samples designated for the HC curve analysis peaking at 1,100°C, and the MHC fire curve peaking at 1,300°C, were subjected to treatment using the structural fire test furnace facilities as shown in Figure 10. This equipment can replicate the exponential profiles of realistic fire curves. Conversely for the experiments using linear heating rates of 2°C/min, 5°C/min, 10°C/min, and 20°C/min,which covers the range of heating rates used in the vast majority of previous studies, peaking at a maximum temperature of 1,100°C with the maximum temperature sustained for one hour, a programmable muffle furnace was employed..

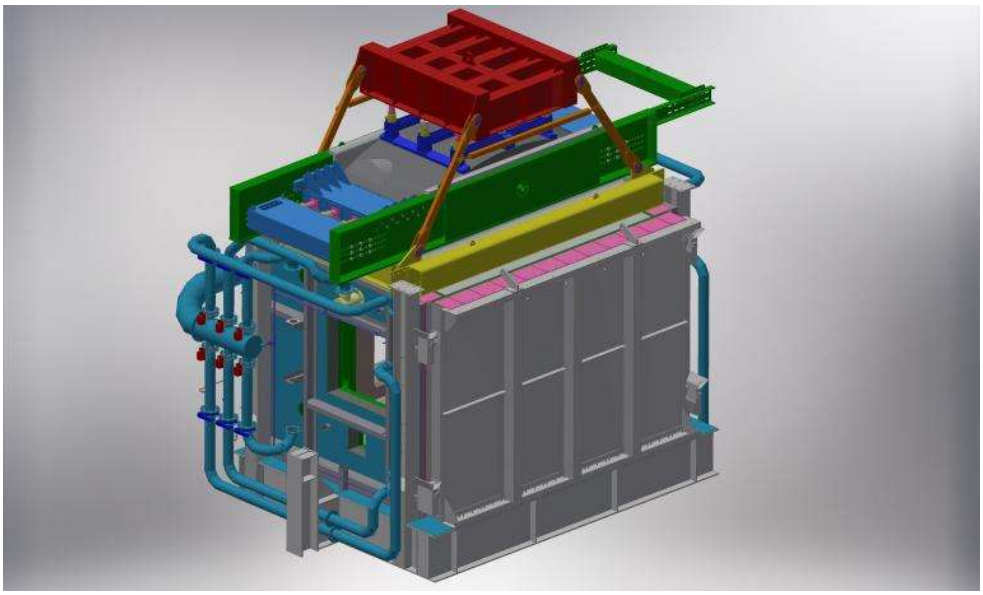

*Figure 10 - Fire testing facility at Victoria University's Werribee campus [69]*

## 3.4 Sample Preparation for Digital Image Correlation Analyses

In the application of digital image correlation (DIC) using the Ncorr software, an extension for Matlab, meticulous preparation of the sample surfaces is imperative for precise image analysis. The chosen methodology involves coating of the specimens after heat treatment on the side of the sample undergoing video recording with a layer of white paint, followed by the application of random black speckles from a spray paint can. This preparation creates an optimal contrast essential for the image correlation process, facilitating the software's ability to track deformations effectively.

The procedure involves capturing video footage of the painted surface as the sample is subjected to axial stress. The contrasting speckles against the white background enable the software to accurately monitor and map the strain distributions on a pixel-by-pixel basis. This process allows for the detailed visualisation of strain patterns as they evolve under stress, providing a comprehensive two-dimensional strain field analysis.

Unlike traditional strain gauges that offer limited one-dimensional strain data, often reduced to peak values or confined within the onset of plastic deformation, DIC offers a multi-dimensional view of strain distribution as shown in Figure 11. This capability not only allows for the identification of peak strain values but also enables the detailed observation of how strain propagates across the sample's surface, offering insights into localised deformation behaviours.

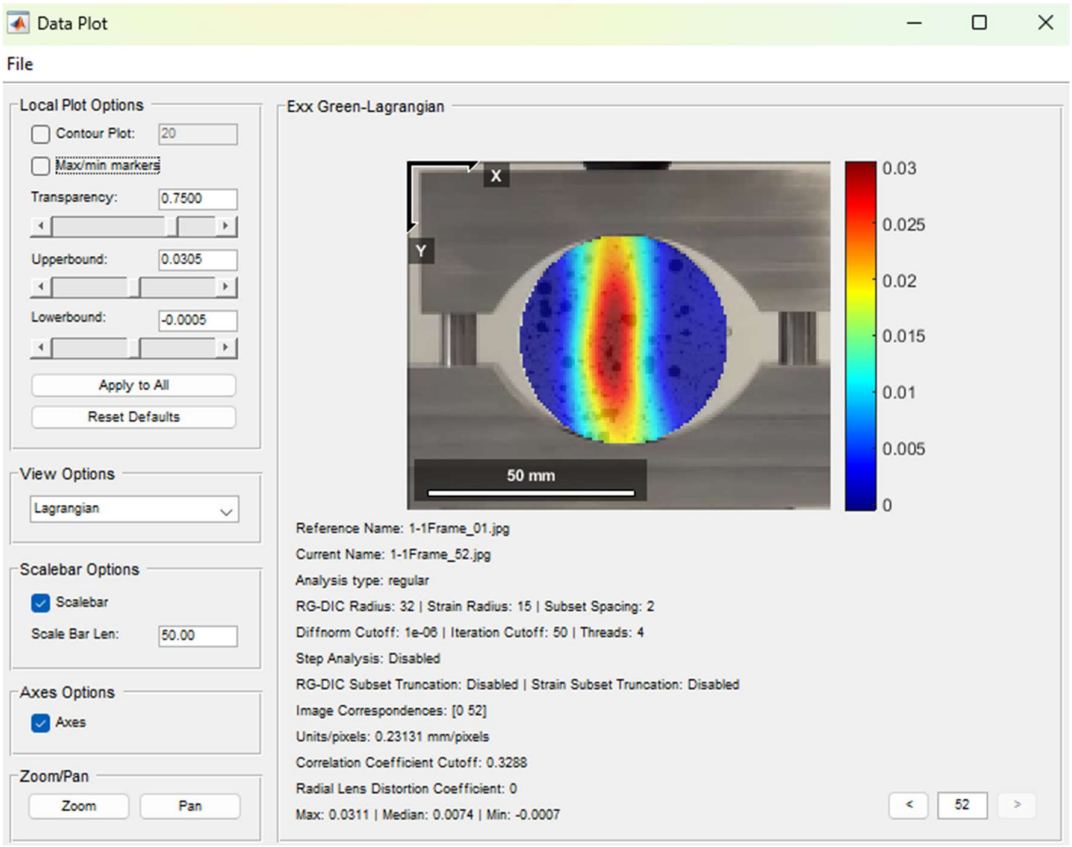


*Figure 11 - Data plotting of Exx Green-Lagrangian with Ncorr v1.2*

For calibration purposes, a known measurement across the observed face is established, allowing for the conversion of pixel dimensions into real-world measurements. This calibration is critical for translating the visual data into accurate strain measurements, ensuring that each pixel's width is correctly associated with a specific measurement scale.

During the sample preparation phase, it is crucial to apply the white base paint as thinly as possible using a brush. This practice is intended to prevent the introduction of a thick paint layer that could mask or alter the strain indications, potentially affecting the DIC's accuracy. Thicker paint layers might exhibit mechanical properties different from those of the sample material, particularly in terms of elastic response, which could lead to erroneous DIC readings.

The video analysis phase involves segmenting the footage into discrete intervals, typically capturing 50 frames from the onset of stress application to the point of initial failure. These frames are then analysed at specific stress intervals—0%, 20%, 40%, 60%, 80%, and 100%—to methodically observe and document the progression of strain and the development of potential failure zones within the sample.

## 3.5 Compression and Tensile Strength Testing

The total count of samples tested, inclusive of their peak temperatures, is listed in Table 2 below:

*Table 2 - Count of samples with diameters, heating rates, peak temperatures, and strength test type*

| | **Sample Naming** | **1_X** | **2_X** | **3_X** | **4_X** | **5_X** | **6_X** | **7_X** |
|---|---|---|---|---|---|---|---|---|
| | **Heating Rate** | **None** | **HC** | **MHC** | **2°C/min** | **5°C/min** | **10°C/min** | **20°C/min** |
| **Diameter (mm)** | **Peak Temperature / Testing Type** | **25°C** | **1100°C** | **1300°C** | **1100°C** | **1100°C** | **1100°C** | **1100°C** |
| 20 | **Compression** | 3 | 3 | 3 | | | | |
| 32 | **Compression** | 3 | 3 | 3 | | | | |
| 50 | **Compression** | 3 | 3 | 3 | 3 | 3 | 3 | 3 |
| 50 | **Tensile** | 3 | 3 | 3 | 3 | 3 | 3 | 3 |
| 67 | **Compression** | 3 | 3 | 3 | | | | |
| 82 | **Compression** | 3 | 3 | 3 | | | | |

For the compression and tensile strength testing, the RTX-1000 compression testing rig at Victoria University's Rock Mechanics laboratory was used. The painted face of compression and tensile strength specimens would face an iPhone camera which was set up, and then the relevant test would be undertaken while being filmed, as shown in Figure 12.

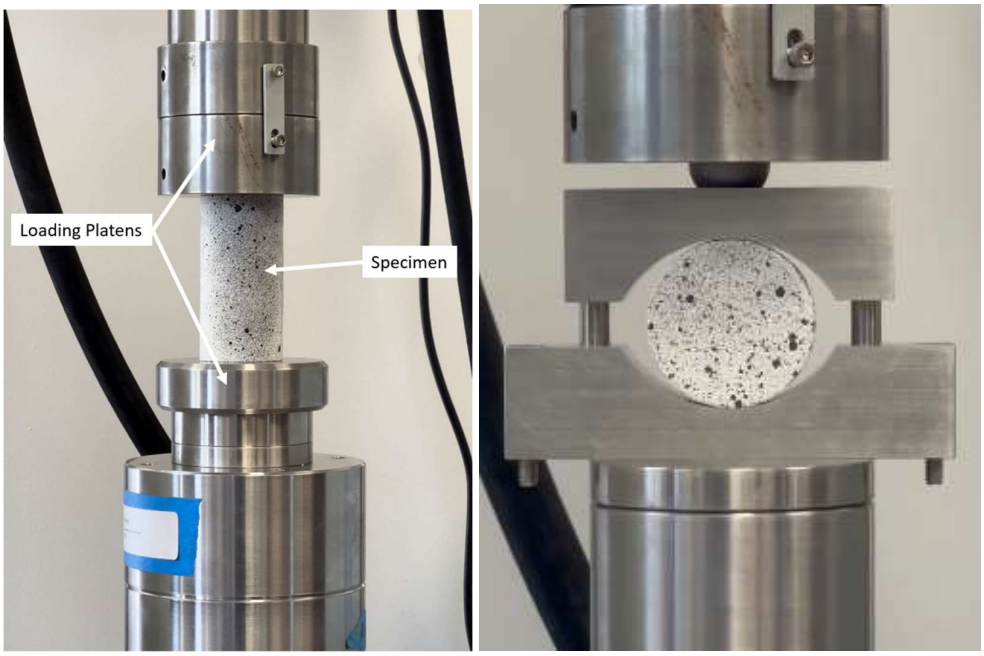


*Figure 12 – Painted sample undergoing (a) compression and (b) tensile testing*

## 3.6 X-ray Diffraction (XRD)

In this research the use of X-ray Diffraction was used to determine the mineral composition changes before and after heat treatment. The hypothesis was that there is a potential for different heating rates to cause different mineral changes which is often observed in geological formation processes.

The testing itself was completed through the University of Melbourne's Materials Characterisation and Fabrication Platform. XRD was conducted with a Bruker D8 Advance Diffractometer [70]. Due to the strength testing process destroying the cylindrical rock specimens, powder from the centre of the cores was taken after strength testing for further processing prior to XRD characterisation.

## 3.7 Scanning Electron Microscopy (SEM)

Scanning Electron Microscopy was used as a second form of measuring elemental changes with the changes measured from large parts of the specimen before and after heat treatment. SEM can be used for morphological changes; however, this research only focused on elemental changes.

## 3.8 Occupational Health and Safety Risks

The rock mechanics experiments posed several risks in sample preparation and strength testing. Risk analysis for OHS was undertaken in combination with existing policies and

procedures at Victoria University's geotechnical laboratory. The risks associated with the testing are listed in Table 3, which includes the risk management strategy.

The research itself involved simulations of fire with high peak temperatures, however, these tasks were performed under the careful supervision of experienced researchers at the two labs at the Werribee campus, Victoria University, with risks being managed by the OHS procedures there. X-ray diffraction testing was outsourced via Melbourne University.

*Table 3 - List of tests and tasks with the associated risk and management strategy*

| **Test / Task** | **Testing equipment** | **Risk/hazard** | **Risk management strategy** |
|---|---|---|---|
| Sample preparation | Lifting trolley, Diamond tipped drill, Rock trimming and grinding machine | • Possible inhalation of silicon dust<br>• Possibility of dust reaching eyes<br>• Operation of high-speed saw | • Wearing earmuffs during the cutting of samples<br>• Wearing safety glasses during the operation of blade or drilling<br>• Using the protective shields on both cutting machines<br>• Using safe lifting procedures to move sandstone from the delivery pallet with a trolley |
| UCS and indirect splitting tensile test | Compression testing rig | • Possibility of dust or rock fragment reaching eyes | • Wearing safety glasses during strength testing |

# 4. Experimental Results and Discussion

## 4.1 Compressive Strength Results

The compressive strength results for the 50mm samples under various heat treatments are presented in Figure 13, with the averaged UCS and peak strain values shown in Table 4 and visualised with Figure 14. The results indicate a clear trend of strength reduction with increasing heating rates, as well as significant changes in peak strain behaviour. This aligns with observations from other studies but also highlights unique trends that require further analysis.

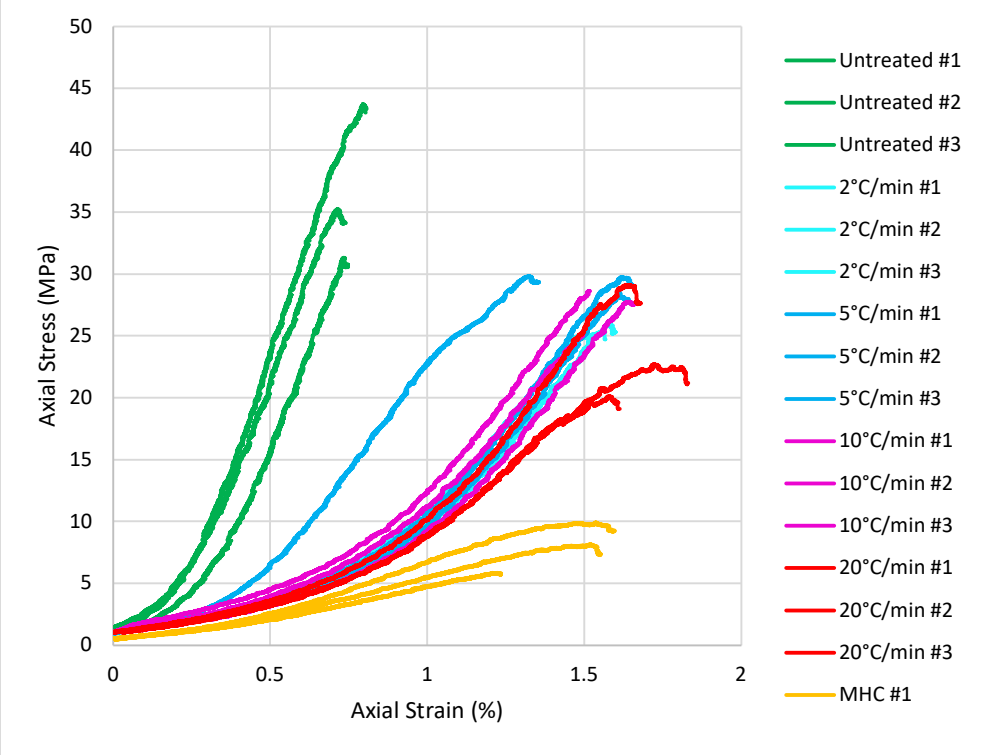


*Figure 13 - Axial stress versus axial-strain results from 50mm compressive strength testing samples for heating scenarios 1 and 3-7*

Table 4 - Summary of maximum strain and maximum stress at that strain for compression testing

| Samples | Max. Strain | Max. Axial Stress |
|---|---|---|
| Untreated 50mm Average - Max Temp 25°C | 0.77 | 34.92 |
| Linear 2°C/min 50mm Average - Max Temp 1,100°C | 1.54 | 24.04 |
| Linear 5°C/min 50mm Average - Max Temp 1100°C | 1.65 | 28.53 |
| Linear 10°C/min 50mm Average - Max Temp 1100°C | 1.56 | 27.08 |
| Linear 20°C/min 50mm Average - Max Temp 1100°C | 1.72 | 20.16 |
| MHC 50mm Average - Max Temp 1,300°C | 1.46 | 7.47 |

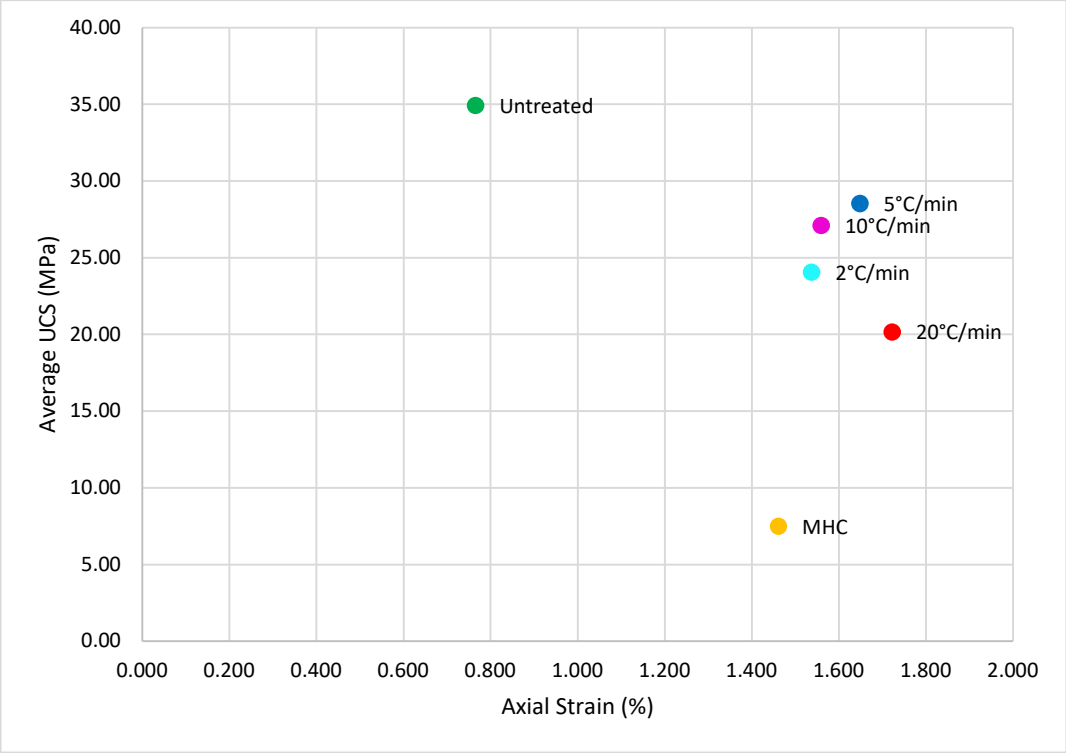


*Figure 14 - Average UCS versus peak axial strain values for different heat treatments*

The UCS results indicate that heat treatment reduces the compressive strength and increases peak strain, with the most significant reductions observed under rapid heating rates, such as 20°C/min and extreme temperatures, such as the MHC treatment. This is consistent with the findings by Lei et al [35], who observed decreases in compressive strength of sandstone above 400°C due to porosity increases and microcrack development. Additionally, the rapid heating under the MHC regime appears to exacerbate these effects, producing brittle failures similar to those described by Lintao et

al. [37] and Ranjith et al [38], where rapid heating leads to significant reductions in UCS beyond 800°C.

Comparisons can also be drawn with Hao et al. [34], who observed that sandstone's mechanical properties peak at around 300°C before declining significantly at higher temperatures. Similarly, in this study, peak strain increased with higher heating rates, particularly at 20°C/min, and UCS declined to its lowest point. This may be attributed to water loss, mineral decomposition, and the propagation of microcracks, as noted by Zhao et al [47] and Zhang et al [48] in their studies on thermally treated sandstone and granite.

The results also highlight that slower heating rates (e.g., 2°C/min and 5°C/min) allow for greater elastic deformation, potentially due to slower thermal gradients reducing internal stress concentrations. This behaviour parallels the findings of Brotons et al [33], who demonstrated reduced mechanical degradation under slower heating conditions. Additionally, the colour and physical changes observed in samples post-treatment are comparable to those reported by Xu et al [44], indicating progressive thermal damage.

The behaviour of axial strain is particularly noteworthy. While no direct linear relationship is observed between heating rate and axial strain, the 20°C/min samples exhibit the highest strain at failure (1.7%), suggesting a threshold beyond which thermal damage becomes more pronounced. This is corroborated by findings from Jin et al [39], where rapid heating led to significant strain increases due to thermal shock effects.

Finally, the substantial reductions in UCS observed under the MHC treatment align with observations from Rao and Wang [40] and Lu et al [41], who noted that high-temperature regimes and rapid heating rates induce irreversible damage, such as pore expansion and crack network formation. The brittle nature of these failures supports the hypothesis that rapid heating compromises the material's ability to sustain loads.

In conclusion, the findings in this study underscore the importance of heating rates in determining the mechanical properties of sandstone. The observed trends align with previous studies, reinforcing the idea that peak temperatures, as well as heating regimes, play a critical role in microstructural degradation. However, the deviations seen at higher heating rates, particularly with the MHC treatment, suggest that unique factors specific to exponential heating rates may play a unique role in affecting mineral composition and microstructure with Hawkesbury sandstone, given the clay content of the rock. Further

investigation, particularly at intermediate temperatures and largest sample sizes, is recommended to elucidate these effects fully.

## 4.2 Splitting Tensile Strength Test

Heat-treated samples with a 50 mm diameter were tested using the splitting tensile strength test, and the results are presented in Figure 15 and Table 5, showing the maximum tensile strength and the strain at maximum stress for each tested condition.

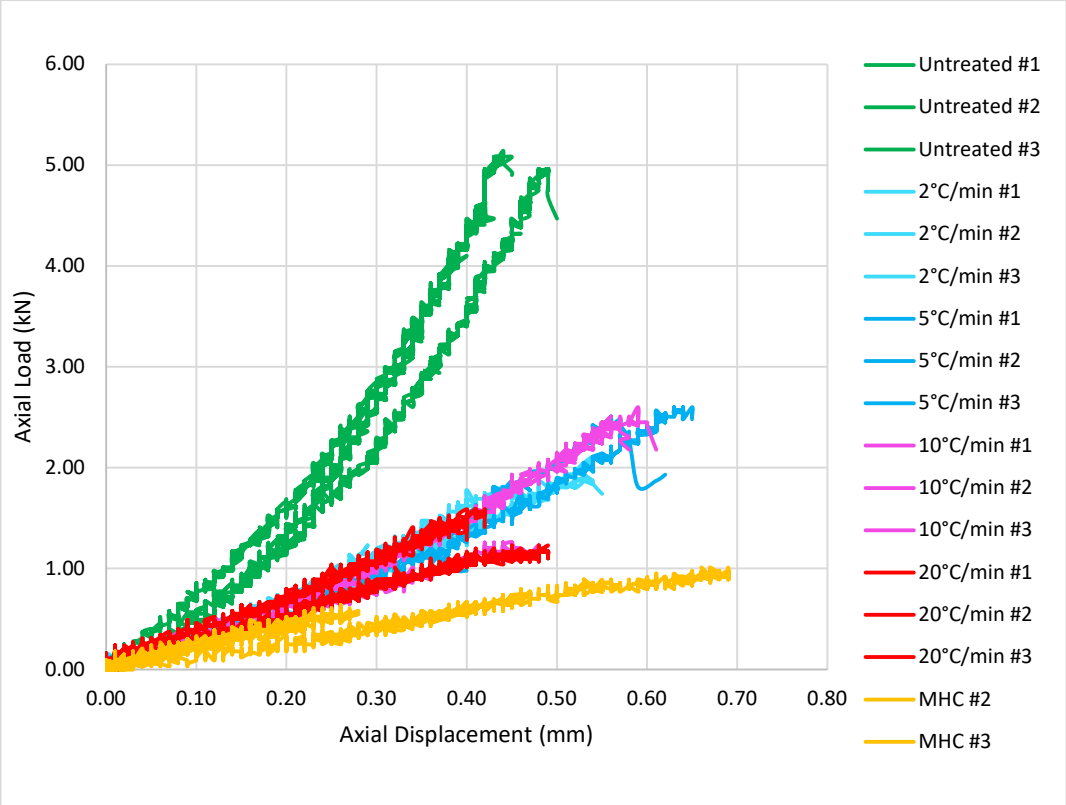


*Figure 15 - Axial load versus axial displacement curves of specimens after tensile strength*

*Table 5 - Summary of maximum displacement and maximum load at that strain for tensile strength testing*

| **Samples** | **Max. Strain (mm)** | **Max. Tensile Strength (MPa)** |
|---|---|---|
| Untreated 50mm Average - Max Temp 25°C | 0.46 | 0.62 |
| Linear 2°C/min 50mm Average - Max Temp 1100°C | 0.52 | 0.25 |
| Linear 5°C/min 50mm Average - Max Temp 1100°C | 0.5 | 0.23 |
| Linear 10°C/min 50mm Average - Max Temp 1100°C | 0.56 | 0.27 |
| Linear 20°C/min 50mm Average - Max Temp 1100°C | 0.45 | 0.18 |
| MHC50mm Average - Max Temp 1300°C | 0.56 | 0.11 |

Figure 16 depicts the average of the maximum axial load and displacement at peak load during tensile strength testing.

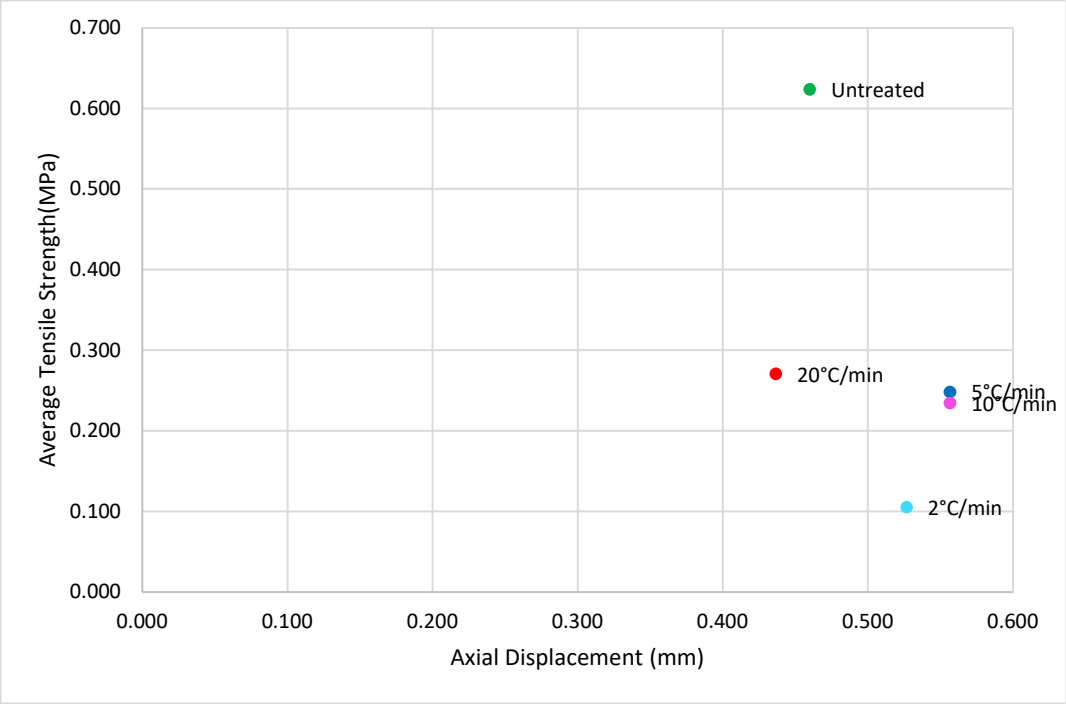


*Figure 16 - Average tensile strength versus peak axial displacement values of the different heat treatment scenarios*

The tensile strength results reveal a grouping trend for the linear heat-treated samples between 2°C/min and 10°C/min, with a noticeable divergence at the more aggressive heating rate of 20°C/min. A marked separation is observed in MHC specimens tested at 1,300°C, which displayed significantly lower tensile strength. This is consistent with findings by Heap et al. [45], who documented a 94% reduction in tensile strength for high-strength concrete samples as temperatures approached 1,000°C, citing extensive microstructural damage and transition to ductile behaviour as key contributors to the reduction.

The absence of clear differentiation among the linear heating rates of 2°C/min to 10°C/min aligns with findings by Ozgun and Ozcelik [46], who reported similar reduction trends in tensile strength across varying heating rates up to 5°C/min, with microscale cracking becoming evident above 400°C. However, the substantial reduction observed at 20°C/min suggests a thermal threshold beyond which the rapid heating exacerbates internal stresses, possibly leading to pronounced microcracking. This aligns with Lu et al. [41], who highlighted that longitudinal wave velocity—a proxy for

internal cracking—showed a consistent downward trend with temperature increases, correlating to reduced tensile strength.

For MHC-treated samples, the sharp reduction in tensile strength to 0.11MPa can be linked to the extreme peak temperature of 1,300°C, which surpasses the melting threshold of quartz and promotes macro-fissure formation, as noted by Lu et al [41]. These results also indicate that the aggressive thermal cycles in the commercial kiln may have introduced heterogeneity in sample heating, potentially amplifying damage. Similar behaviours were observed by Rao and Wang [40], who suggested a critical thermal threshold for sandstone, albeit at lower temperatures, where strength significantly declined.

Interestingly, while the peak axial strain increased for most linear heat-treated samples, the 20°C/min specimens showed reduced strain despite their lower tensile strength. This suggests a shift in failure mechanisms, possibly from ductile to brittle modes, which warrants further investigation. This is then different in the MHC samples having displacements between 0.27 and 0.68mm, which is not a large enough data set to make a conclusion. Heap et al. [45] similarly reported a transition from brittle to ductile behaviour at higher temperatures in concrete, characterised by increased strain and reduced mechanical strength.

The results of this study emphasise the complex interplay between heating rate, peak temperature, and thermal damage mechanisms. Grouping results for 2°C/min to 10°C/min may suggest a plateau in damage propagation within this range. At the same time, deviations at higher rates and temperatures point to critical thresholds where thermal stresses dominate. Further testing, especially with larger sample sets, is required to confirm the influence of specimen size and kiln heterogeneity observed in the MHC-treated samples.

## 4.3 Scale Effect

The results of the scale effect test, conducted on both untreated and 2°C/min heat-treated samples across five different diameters, are presented in Figure 17 and Figure 18. The data were analysed using the Hoek-Brown scale effect formula to evaluate the alignment of experimental results with the theoretical scaling predictions.

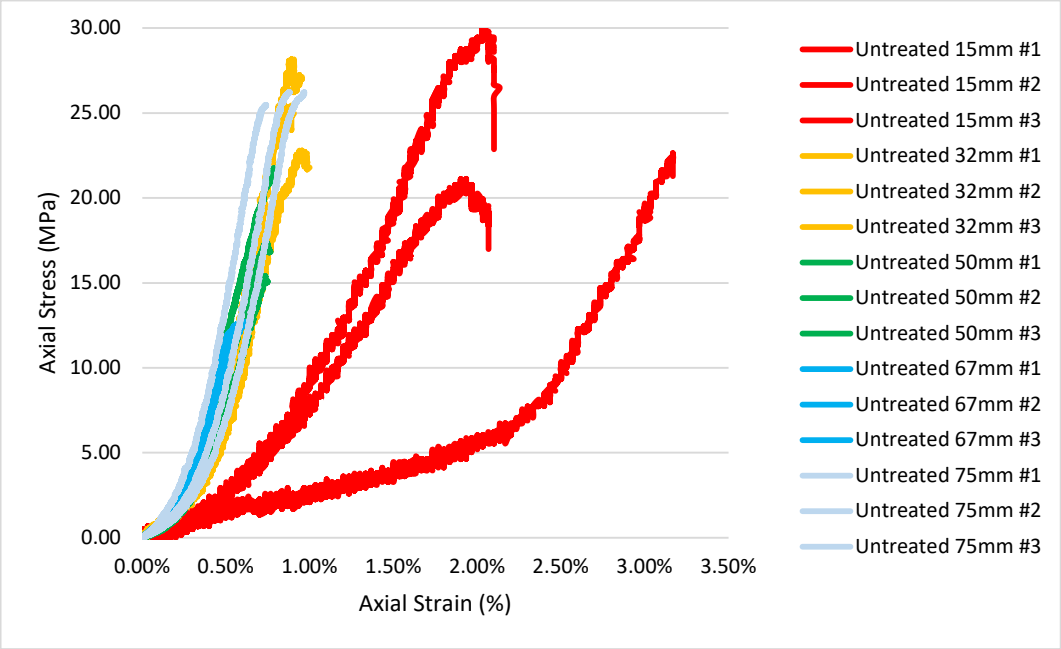


*Figure 17 - Scale effect results for untreated specimens*

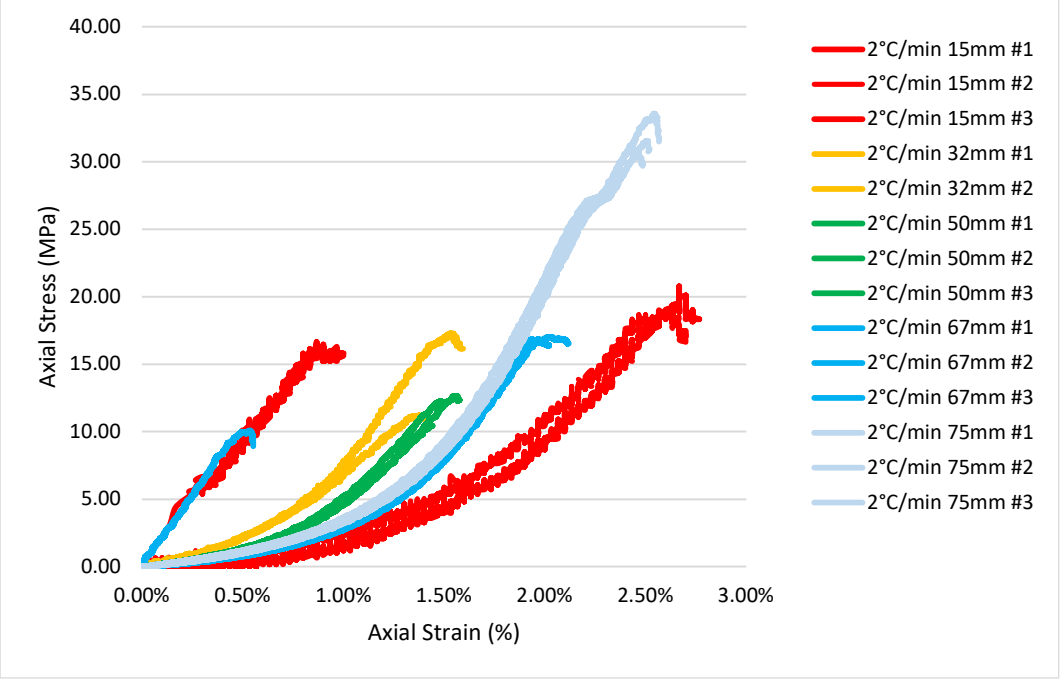


*Figure 18 - Scale effect results for heat-treated specimens at 2°C/min*

In Figure 17, there are clear groundings of results, with all diameters except 15mm achieving similar strain percentages around 0.5-1%, while the 15mm sample pulls away with a greater value between 2-3.25%. The heat treated in Figure 18 shows a different story with a wider range of values but more clustering around the peak stress values.

The adjusted UCS values appear to be lowest at the 50mm results in both data sets, with higher values observed for smaller and larger diameters. This diverges from the understanding of the Hoek-Brown formula, which predicts a general decrease in strength with increasing diameter. This diverges from the understanding of the Hoek and Brown formula. The reductions in strength range from 24% to 44%, with the most significant decreases occurring at diameters of 15mm, 32mm while the 75mm sample mildly increased in strength. The heat treatment was conducted in a closed kiln system with a gradual temperature increase, and all samples were treated together on the same day and in the same session. This controlled process eliminates heating inconsistencies as a potential source of variation in the results. Furthermore, similar trends are observed in the untreated samples, ruling out experimental inconsistencies as a cause. However, a larger sample size would be necessary to validate these findings further.

Figure 19 presents the results evaluated against the Hoek and Brown formula. The formula, based on trends identified in Hoek and Brown's [57] experimental data, demonstrated an increase in strength with decreasing sample diameter and tapering after 100mm. While these trends were observed across various rock types, sandstone was not included in their dataset. The graph shows that while the 15mm and 32mm samples may partially align with the general trend, they deviate significantly from the calculated values, and the 67mm and 75mm samples do not follow the curve at all. This indicates a potential limitation in the applicability of the Hoek-Brown model to Hawkesbury sandstone or heat-treated specimens and an increase of strength at 75mm, which would need to be further investigated with repeat tests.

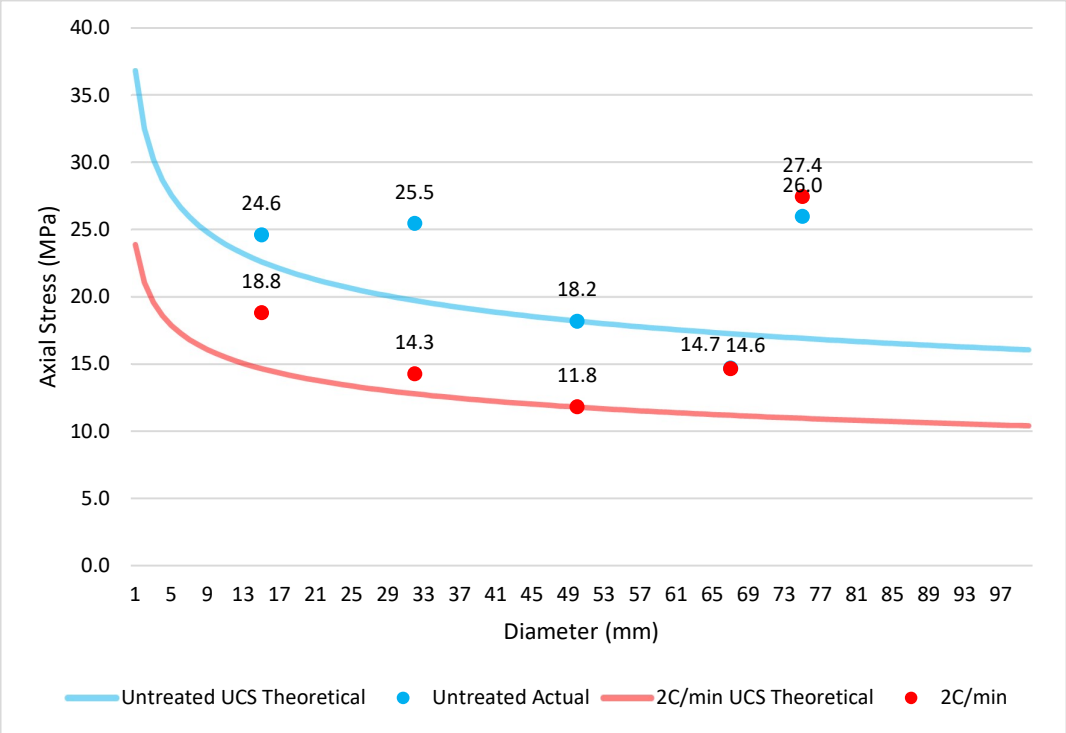


*Figure 19 – Scale effect results estimated using the Hoek and Brown empirical models*

A key observation is that the trends in strength reduction for both untreated and treated samples contradict the expected behaviour as per Hoek and Brown's scaling theory. Pells *[59]* provides an alternative explanation, highlighting that Hoek and Brown's dataset primarily involved igneous or crystalline rocks, which often contain microcracks that influence size-dependent strength. In contrast, Hawkesbury sandstone, a sedimentary rock, exhibits different microstructural characteristics that may not conform to the same scaling behaviours.

The standard deviations calculated (under the appendices as Table 15) further support this observation. Untreated samples for 15-67mm show a wide spread of results with a standard deviation of 0.4 to 3.9 indicating variability in strength across the dataset. Meanwhile, heat-treated samples, excluding the incomplete 32mm dataset, show tighter clustering around the mean, with a standard deviation of 0.2-3.2. For both data sets the 75mm specimens had the lowest standard deviations in results, with higher strengths recorded. These differences suggest that heat treatment may influence the uniformity of the samples but does not necessarily reconcile the observed trends with the theoretical scaling.

These results underline the importance of considering specific rock properties and the effects of heat treatment when applying scaling models. The deviation from Hoek and Brown's predictions emphasises the need for more comprehensive datasets that account for sedimentary rocks like Hawkesbury sandstone. Additionally, larger sample sizes and expanded testing under varying treatment conditions are recommended to validate and further explore the observed discrepancies.

## 4.4 Deformation and Damage Evolution Using Digital Image Correlation

The application of digital image correlation (DIC) using the Ncorr v1.2 software in our study was aimed at evaluating the evolution of deformation patterns and assessing damage during compression tests. Specifically, this technique utilised images derived from recorded video sequences to conduct a detailed deformation analysis. However, it is important to note that the video data for sample untreated 50mm #2 encountered corruption issues, leading to a lack of image data for this sample, thus illustrating the challenges in maintaining data integrity across all test samples.

For the image analysis, a systematic approach was adopted where the video was segmented into 51 discrete frames, selected at regular intervals. This segmentation facilitated a structured analysis, with key frames at positions 1, 10, 20, 30, 40, and 51 chosen for detailed examination, corresponding to strain progression stages at 0%, 20%, 40%, 60%, 80%, and the point of failure, respectively. These frames were deemed appropriate in visualising the straining behaviour as it progressed in both the Eyy and Exx components.

Focusing on the untreated sample #3 during compression, Figure 20 and Figure 21 illustrate the strain development in Eyy and Exx, respectively, as the sample approached failure. Additional insights and data compilations related to these findings are shown in the appendices as Figure 47 to Figure 56 for UCS and Figure 57 to Figure 73 for tensile results for the remaining results not listed in the rest of this section.

However, the study encountered significant challenges in employing DIC for compression strength analysis. A limitation observed was the unpredictability and non-uniformity of the failure planes across different samples as part of the experimental design. Initial analyses of several videos suggested that the strain was not displaying as the failure occurred perpendicular to the direction of the film. This discrepancy is attributed to the inherent variability in how compressive forces manifest through the

cylindrical samples, which can be difficult to predict and standardise for consistent DIC application.

The unpredictability of the compressive failure planes meant that the data obtained for strains perpendicular to the applied stress axis were not consistently reliable indicators of impending material failure. While some correlations between observed strain patterns and the actual failure planes were noted, the inconsistency across the sample set rendered this approach less effective for comprehensive compression strength analysis. Therefore, despite observing strain in the Eyy plane that aligned with the eventual failure zones in some samples, the overall method was deemed unsuitable for predictive or quantitative assessment of compression strength based on the current experimental design and observed data variability.

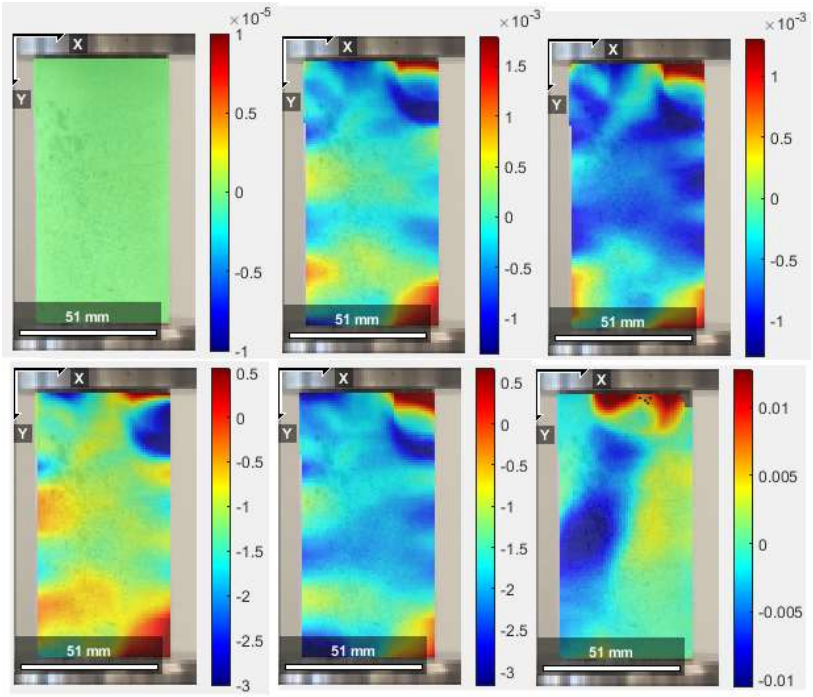


*Figure 20 – Untreated 50mm sample #3 showing Eyy strain plot using Green-Lagrangian method*

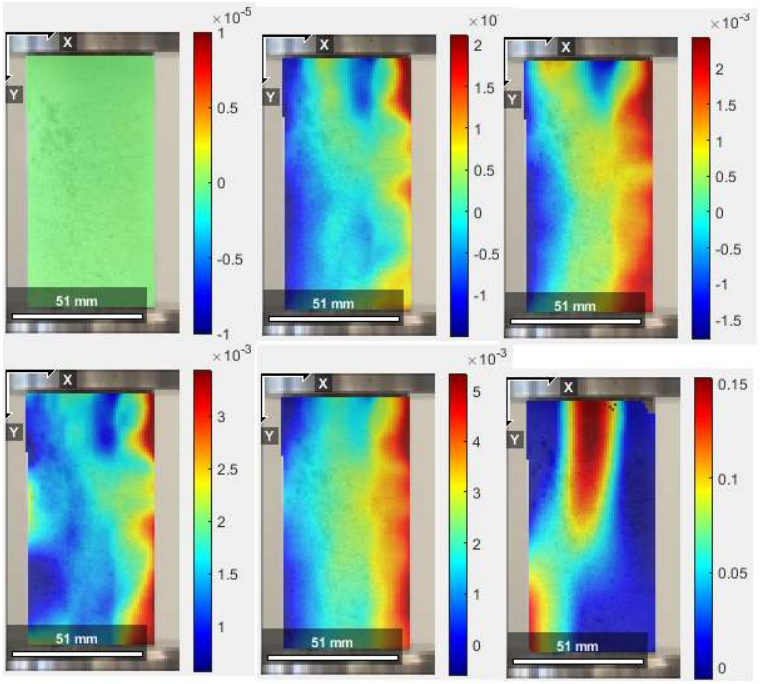


*Figure 21 – Untreated 50mm sample #3 showing Exx strain plot using Green-Lagrangian method*

During the tensile strength testing phase, the digital image correlation (DIC) technique proved to be far more effective in measuring strain across the different heat treatments. This was primarily due to the planeness of the surface of the specimens and the position of the video recording, which was set parallel to the expected failure planes, facilitating the DIC process. Figures 22-24 illustrate the Exx strain for samples subjected to no treatment, 2°C/min heating, and MHC heating, respectively, enabling a comparative analysis of the effects of varied thermal treatments on material behaviour.

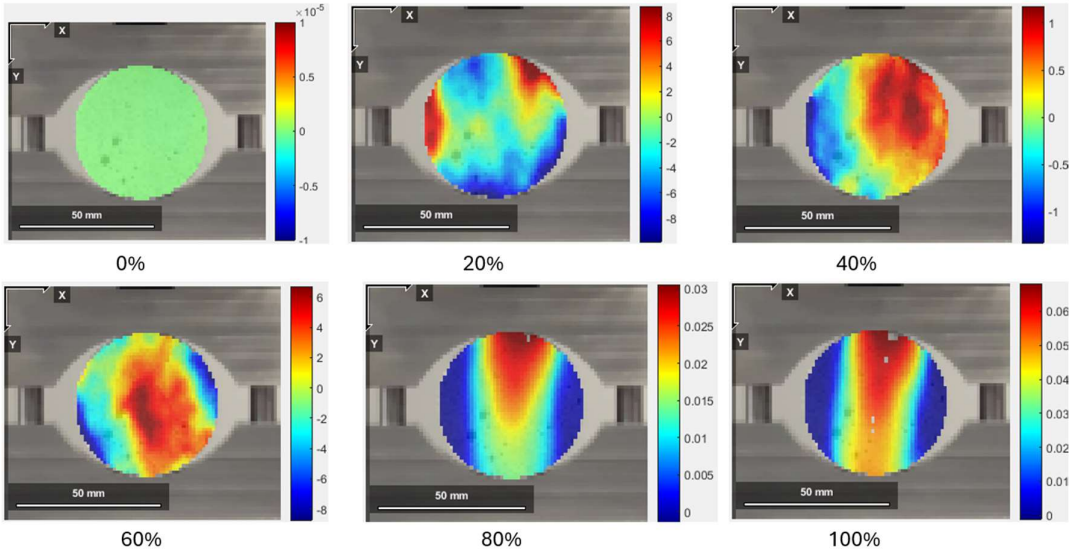


*Figure 22 – Untreated Sample #3, Exx Green-Lagrangian*

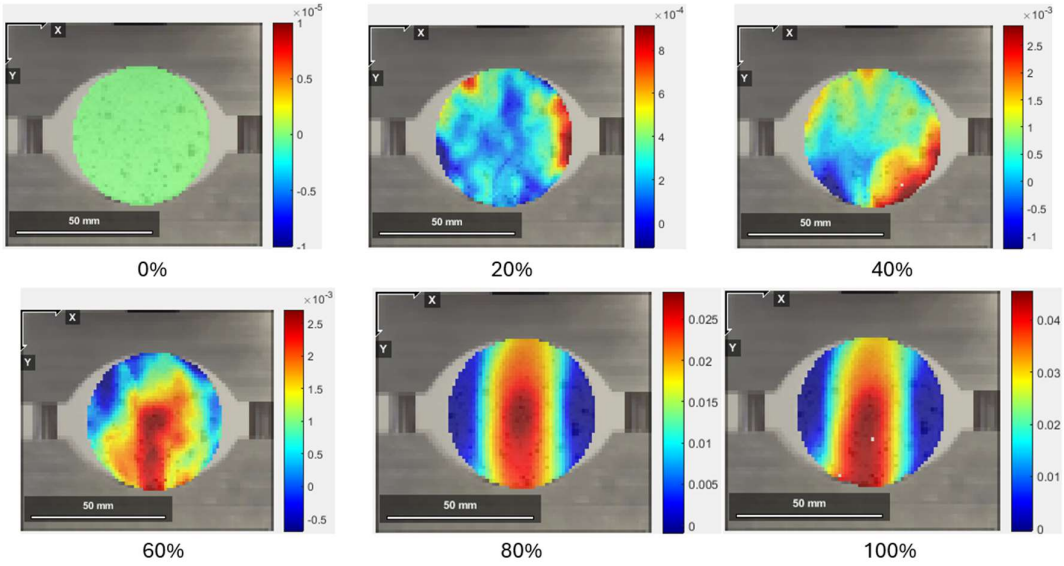


*Figure 23 – 2°C/min Sample #3 Exx Green-Lagrangian*

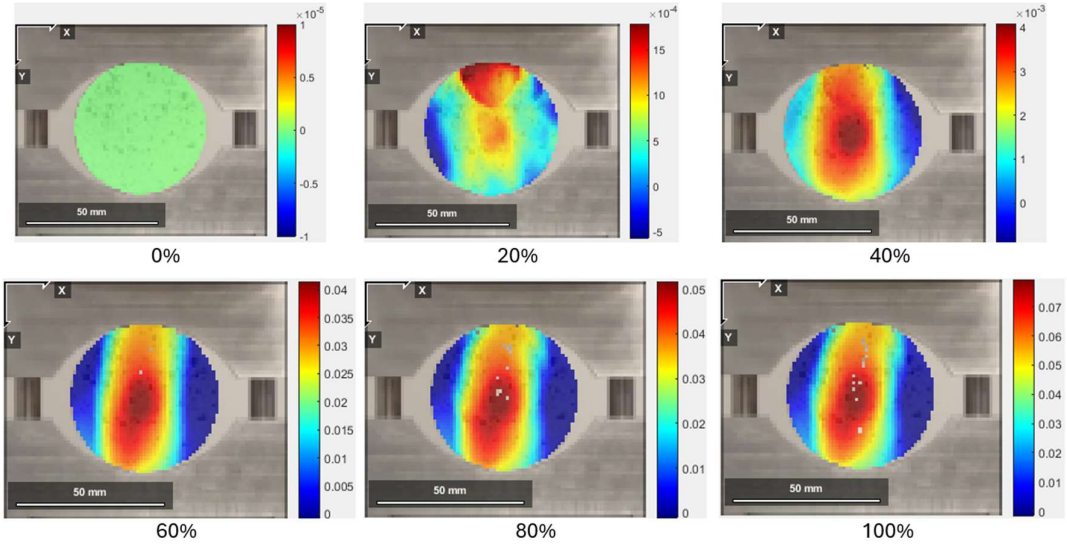


*Figure 24 – Modified Hydrocarbon Sample #3 Exx Green-Lagrangian*

Although there was a noticeable discrepancy between the strain readings obtained from the DIC process and those recorded by the traditional testing apparatus, the DIC method successfully captured the varying strain responses across the face of the samples to thermal treatments. This was particularly evident as the DIC-derived strain data closely aligned with the visual progression of crack formation observed in the video recordings up to the point of tensile failure.

Figure 25 shows the strain output of Ncorr, depicting values extracted from the final image captured of a sample, which displays calculated values expressed across the face of the sample. This analysis is based on all 51 images, referenced against the initial image

prior to stress application, and provides a detailed evaluation of maximum, minimum, and median strain values across the sample's face, as compiled in Table 6.

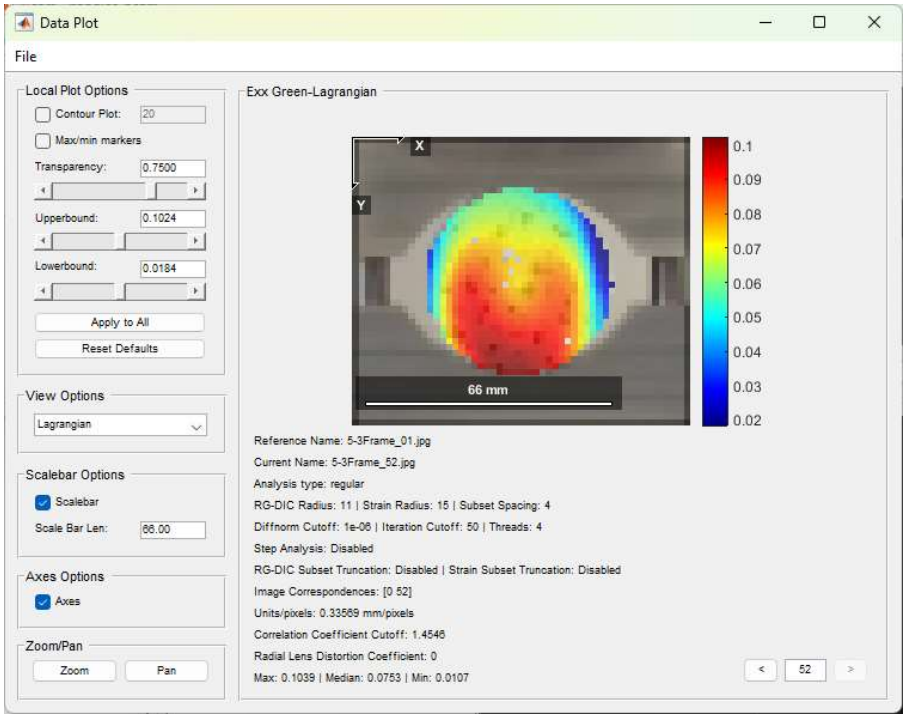


*Figure 25 – Ncorr data plot for the final image of 5°C/min heating sample #3*

*Table 6 – Horizontal strain values for tensile testing using Ncorr analysis*

| | **Exx** | | |
|---|---|---|---|
| **Sample** | **Maximum Strain (mm)** | **Median Strain (mm)** | **Minimum Strain (mm)** |
| Untreated #1 | 0.0311 | 0.0074 | -0.0007 |
| Untreated #2 | 0.0459 | 0.0254 | -0.0011 |
| Untreated #3 | 0.0726 | 0.0361 | -0.0015 |
| 2°C/min #1 | 0.0515 | 0.0269 | -0.0003 |
| 2°C/min #2 | 0.0574 | 0.0197 | -0.0005 |
| 2°C/min #3 | 0.0461 | 0.0260 | -0.0006 |
| 5°C/min #1 | 0.0288 | 0.0195 | 0.0002 |
| 5°C/min #2 | 0.0759 | 0.0552 | 0.0050 |
| 5°C/min #3 | 0.1039 | 0.0753 | 0.0107 |
| 10°C/min #1 | 0.0932 | 0.0325 | 0.0011 |
| 10°C/min #2 | 0.0981 | 0.0876 | 0.0014 |
| 10°C/min #3 | 0.0722 | 0.0200 | -0.0034 |
| 20°C/min #1 | 0.1261 | 0.0459 | -0.0102 |
| 20°C/min #2 | 0.0589 | 0.0160 | -0.0515 |
| 20°C/min #3 | 0.0497 | 0.0225 | -0.0033 |
| MHC #2 | 0.0372 | 0.0185 | 0.0005 |
| MHC #3 | 0.0806 | 0.0413 | -0.0018 |

A particular challenge encountered with the Ncorr software was its partial coverage in displacement mapping, highlighted in samples like the one in Figure 27, where a significant segment displayed no displacement data. Despite multiple attempts at data reprocessing, this issue persisted, influencing the strain value inconsistencies noted in Table 6. Nearly all median strains have a range of values, which makes averaging ineffective due to the deviation. This persisted even though the data was calibrated against a 50mm sample width.

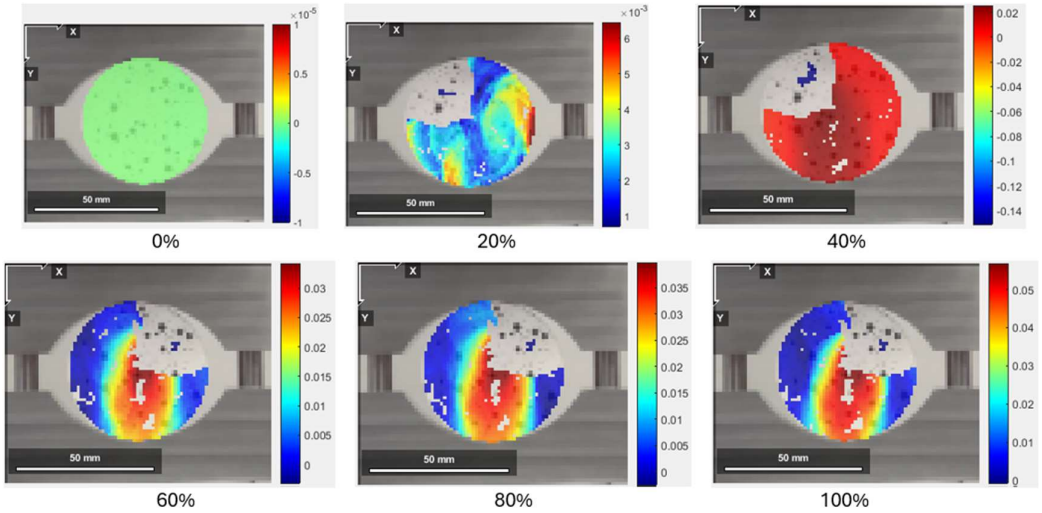


*Figure 26 – DIC strain results (Exx) for Modified Hydrocarbon Curve sample #2 with some face strain not measured*

The summarised data, illustrated in Table 7 and Figure 27, indicates an inconsistent trend where displacement increases for untreated, 5ºC/min and 10ºC/min heating rates, suggesting initial material plasticity. Conversely, a reduction is observed in the 20ºC/min and MHC heating rates. This trend almost aligns with the data in Figure 14 from the measurements collected in the UCS testing, however, the MHC heating rate increases while this measurement decreases. While minimum strain data are provided, their utility is limited due to the lack of corroboration with UCS test results, which focus solely on stress and strain at the point of force application.

*Table 7 – Average DIC values for tensile testing using Ncorr*

| | Exx Averages | | |
|---|---|---|---|
| **Sample** | **Maximum Strain (mm)** | **Median Strain (mm)** | **Minimum Strain (mm)** |
| Untreated | 0.0499 | 0.0230 | -0.0011 |
| 2°C/min | 0.0517 | 0.0242 | -0.0005 |
| 5°C/min | 0.0695 | 0.0500 | 0.0053 |
| 10°C/min | 0.0878 | 0.0467 | -0.0003 |
| 20°C/min | 0.0782 | 0.0281 | -0.0217 |
| MHC | 0.0589 | 0.0299 | -0.0007 |

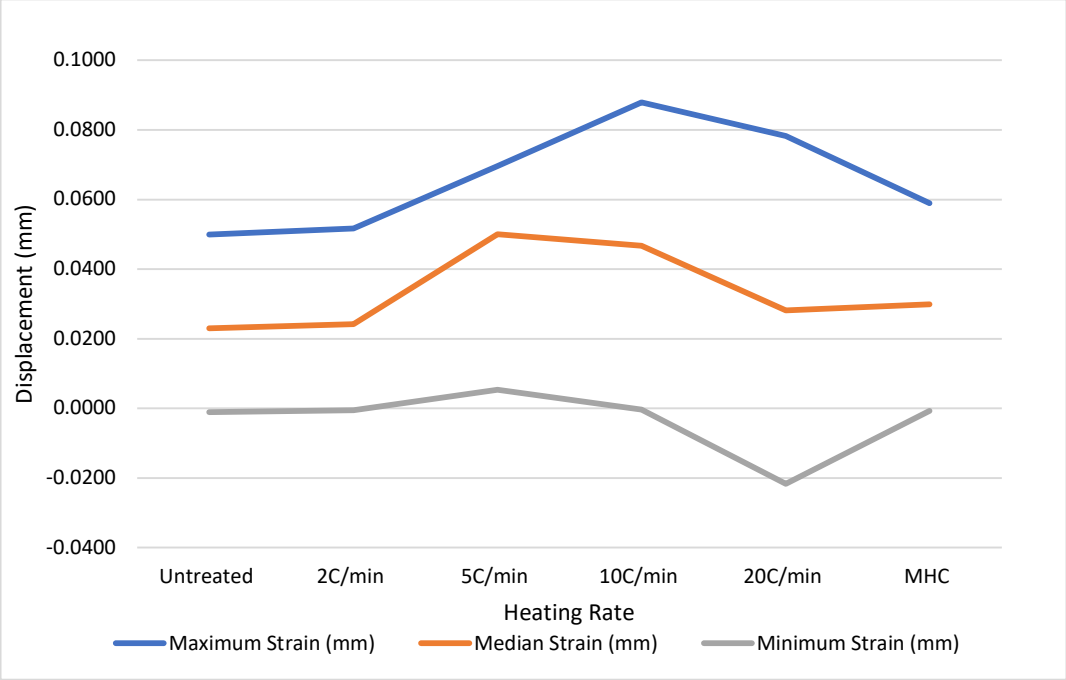


*Figure 27 – Average DIC values for tensile strength testing using Ncorr plotted*

Despite deriving some valuable insights from the current dataset, the evident variability suggests the need for a more extensive sample size to refine the calibration and validation of these results. Such an expanded dataset would significantly enhance the interpretative value of the DIC method, offering a more robust two-dimensional strain analysis across the tensile sample faces.

## 4.5 XRD Results

XRD testing was conducted on the samples after heat treatment and subsequent strength testing. The samples were destroyed to obtain adequate material for XRD analysis. Therefore, the decision was made to utilise failed samples after UCS testing, as mechanical failure was not expected to alter the mineral composition significantly.

XRD analysis indicated a potential trend in the crystallinity percentage. Based on the known composition of sandstone, it was hypothesised that the presence of clay, which contains OH bonds, would undergo dehydration upon heating. This dehydration process could lead to sample consolidation, reducing the clay content and increasing the relative proportion of quartz (SiO2). Gao et al. [73] support this hypothesis, as their study demonstrated that heat treatments of layered sandstone, particularly above 400°C, resulted in significant mineralogical changes due to thermal cracking and dehydration effects.

To illustrate the observed trend, Figure 28 organises the data by heat acceleration rate, starting from room temperature, progressing through increasing linear rates, and concluding with HC and MHC treatments. These results are derived from Figure 29 to Figure 35. XRD plot shows the crystallinity and quartz percentages, revealing an initial decrease in crystallinity followed by an increase at more rapid heating rates. This aligns with the hypothesis that OH bonds in clays are lost during heating, leading to a reduction in clay content and a relative increase in quartz. Pathiranagei et al. [74] observed a similar trend, with clay decomposition and phase transitions, including the dehydroxylation of kaolinite, occurring at temperatures exceeding 400°C. Their research further highlighted the associated increase in porosity with a reduction in clay content.

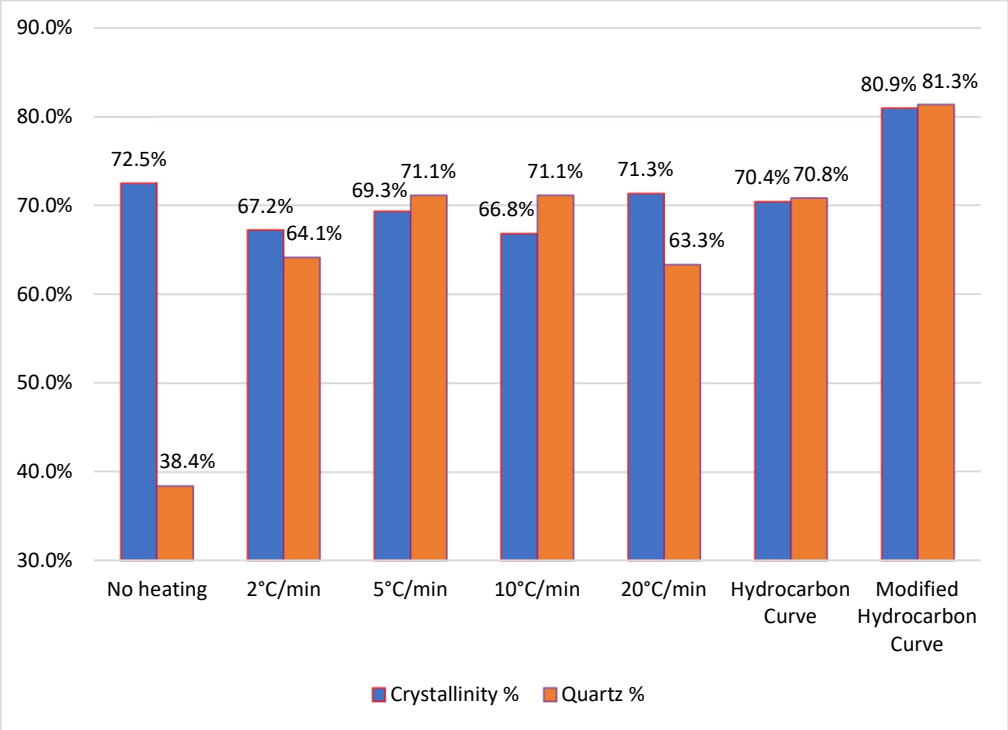


*Figure 28 – Crystallinity and quartz content percentages for different heating rates*

The results also demonstrate a mixture of clays, including SiO2, within the sample composition. However, capturing the precise scale was challenging due to the rapid heating rates in HC and MHC treatments, which achieved peak temperatures in under 10 minutes. In contrast, the linear heating rates required significantly longer durations to reach peak temperatures, with times of 550, 220, 110, and 55 minutes for the respective rates. This progressive difference suggests that the clustered crystallinity and quartz percentages observed for linear heat rates likely reflect the stability of gradual heating. In contrast, the thermal shock induced by HC and MHC treatments resulted in marked variations due to the significantly higher heating accelerations. Meng et al. [75] corroborated these findings, reporting that sandstone subjected to the thermal shock experienced a pronounced reduction in clay content, an increase in quartz, and visible colour changes, transitioning from pale yellow to darker orange above 400°C.

Additionally, digital image correlation (DIC) analysis provided insights into pressure scaling as strain along the failure plane. Variations between samples were evident, influenced by the curved surface of the cylindrical specimens. This curvature introduced inconsistencies in capturing the failure plane across multiple tests, as camera alignment could not uniformly capture the plane for all samples. Gao et al. [73] also utilised DIC to observe thermal cracks forming within and between particles, further validating the technique's utility in studying sandstone subjected to heat treatment.

In summary, the XRD results, in conjunction with DIC analysis and supporting literature, suggest that the heat treatment of sandstone induces significant mineralogical transformations, particularly involving the loss of OH bonds in clays, a relative increase in quartz, and thermal cracking. These changes are magnified under rapid heating conditions, aligning with findings from Gao et al. [73], Pathiranagei et al. [74], and Meng et al. [75].

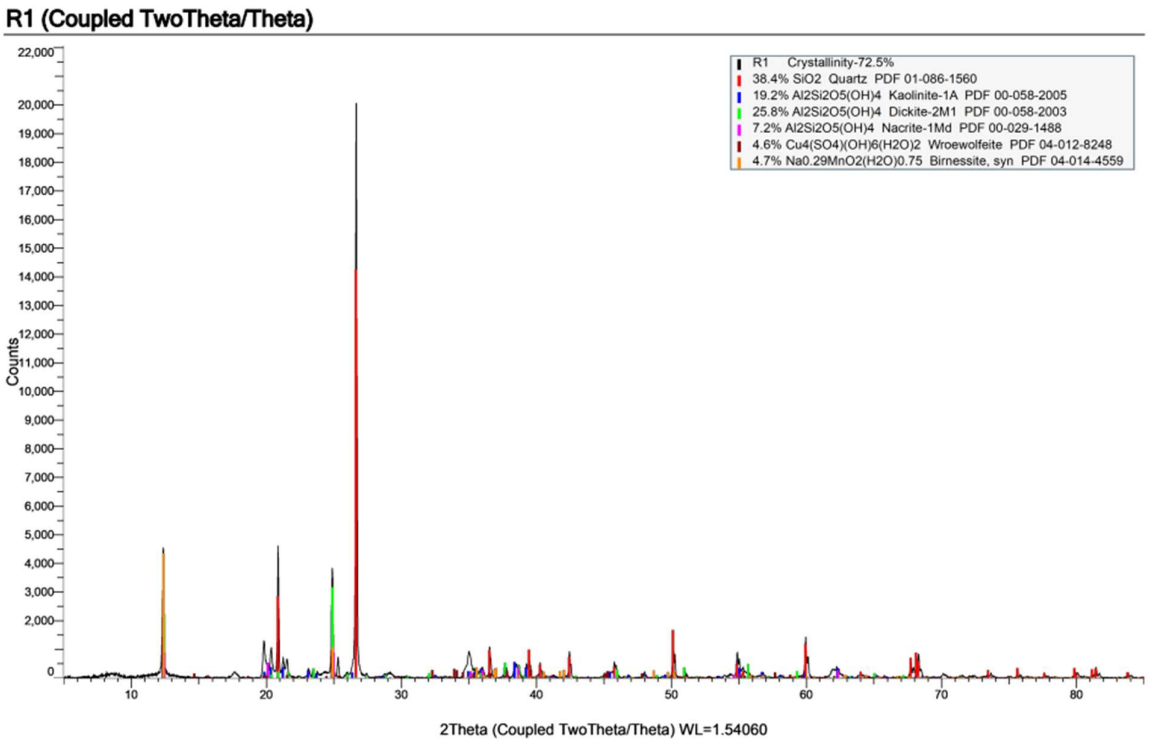


*Figure 29 – Mineralogical composition of heated Hawkesbury sandstone – Untreated*

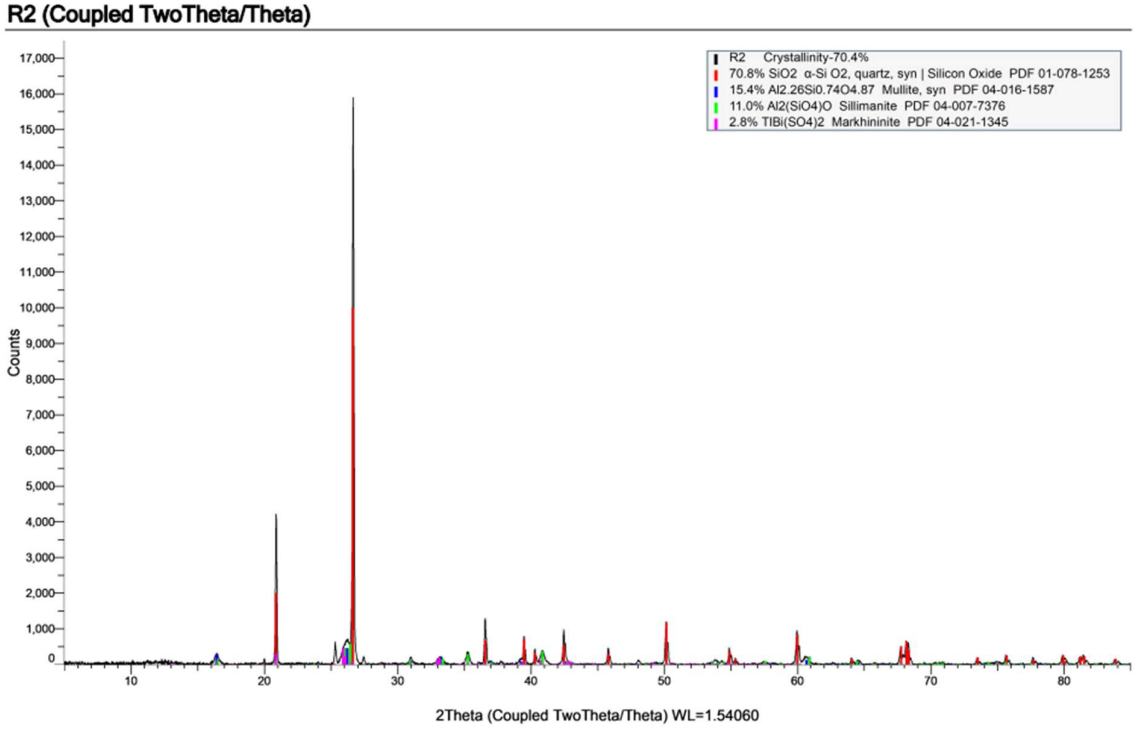


*Figure 30 – Mineralogical composition of heated Hawkesbury sandstone – Hydrocarbon Curve*

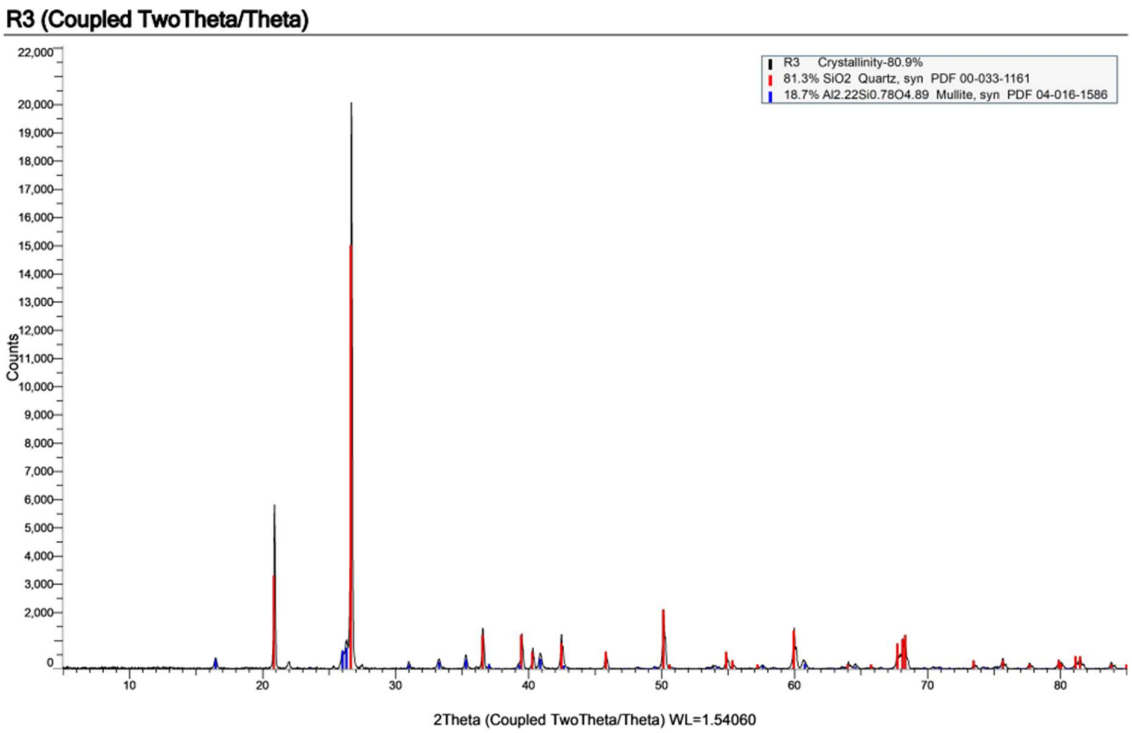


*Figure 31 – Mineralogical composition of heated Hawkesbury sandstone – Modified Hydrocarbon Curve*

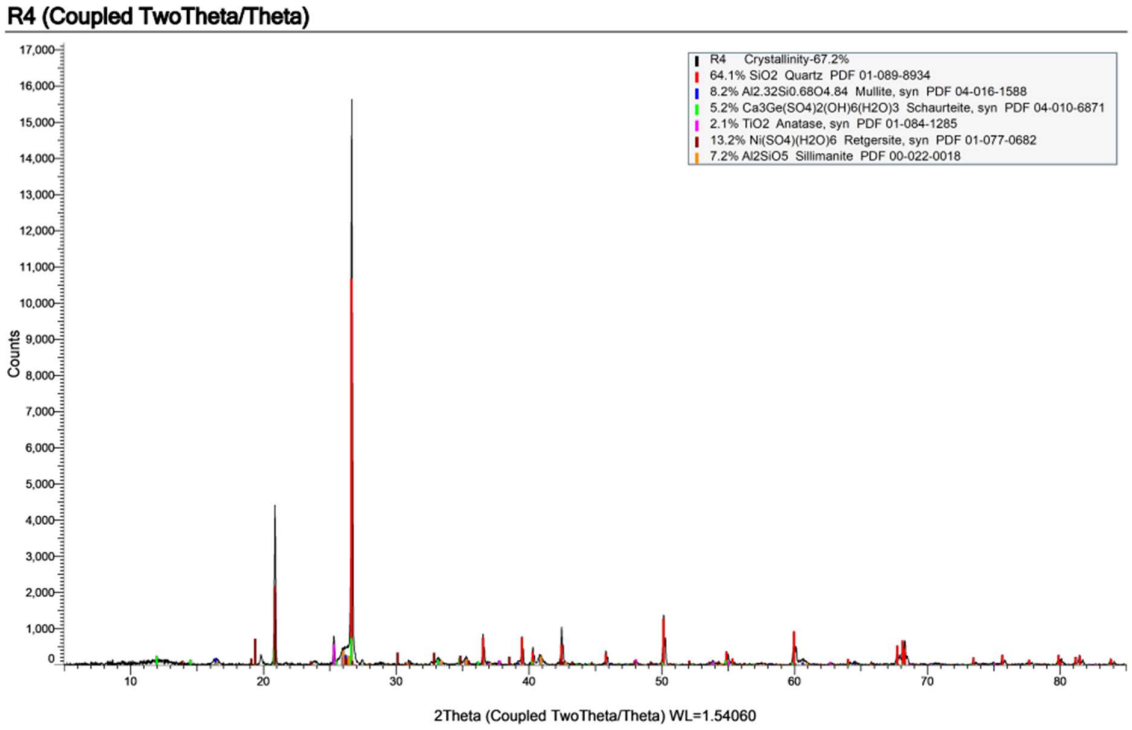


*Figure 32 – Mineralogical composition of heated Hawkesbury sandstone – Linear 2°C/min*

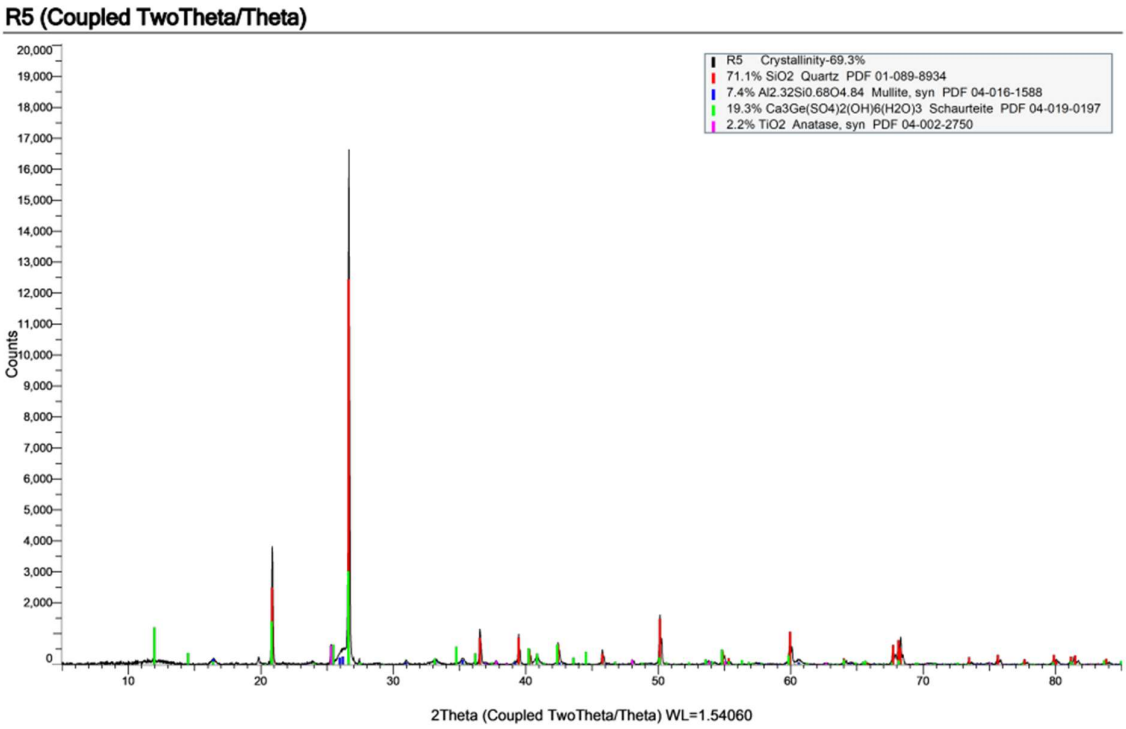


*Figure 33 – Mineralogical composition of heated Hawkesbury sandstone – Linear 5°C/min*

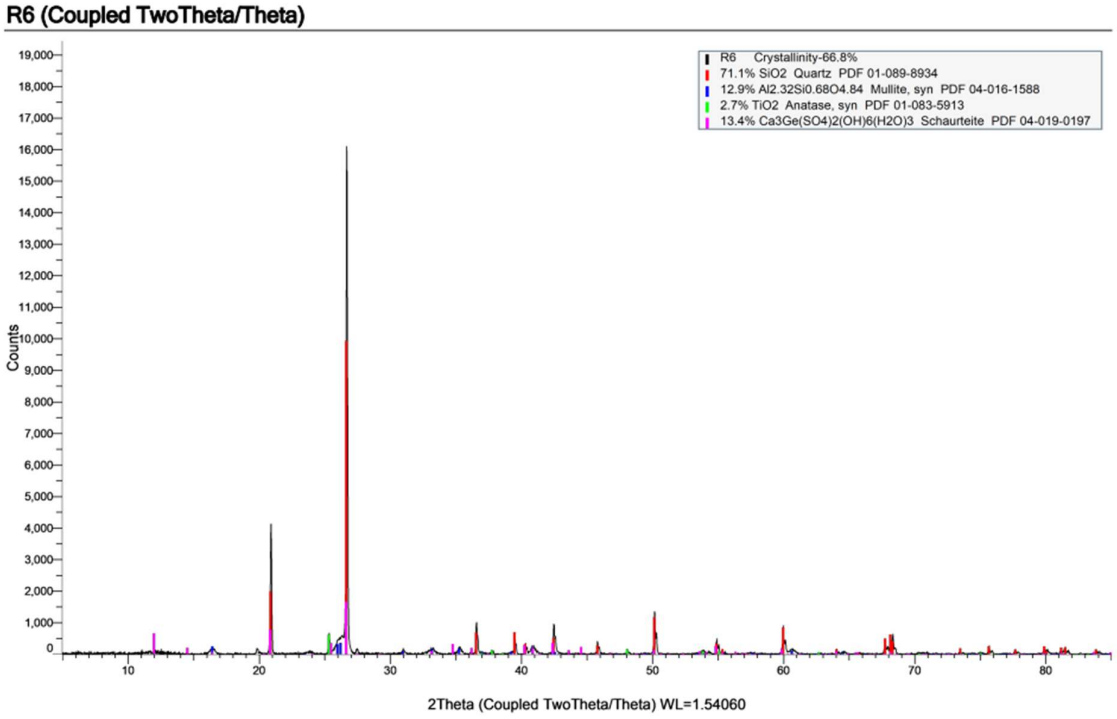


*Figure 34 – Mineralogical composition of heated Hawkesbury sandstone – Linear 10°C/min*

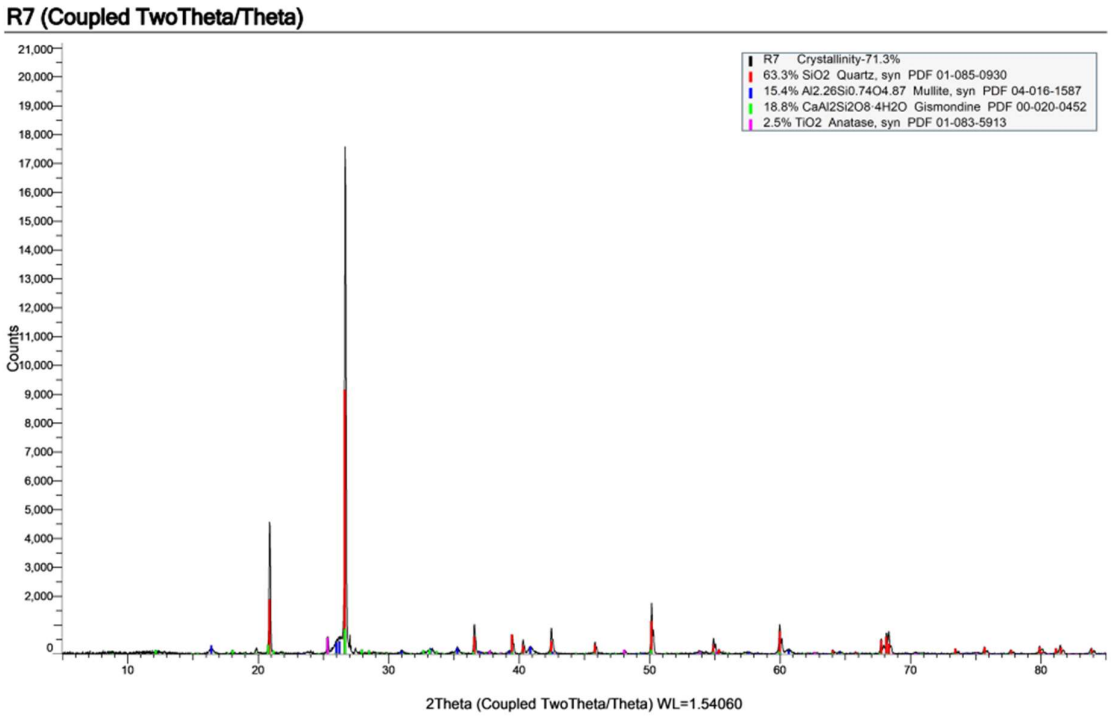


*Figure 35 – Mineralogical composition of heated Hawkesbury sandstone – Linear 20°C/min*

## 4.6 SEM Results

The scanning electron microscopy (SEM) analysis was performed on untreated and heated specimens. After scanning three locations for each specimen, the average atomic and weight concentrations for each case are summarised in Tables 9 and 10, respectively.

*Table 8 – Average of atomic concentration percentage per test*

| **Element** | **Untreated** | **2°C/min** | **5°C/min** | **10°C/min** | **20°C/min** | **MHC** |
|---|---|---|---|---|---|---|
| Al | 4.3% | 6.6% | 5.8% | 4.2% | 5.3% | 4.3% |
| C | 10.2% | 11.2% | 9.7% | 16.2% | 5.8% | 17.5% |
| Cu | 0.2% | 0.2% | 0.1% | 0.1% | 0.1% | 0.2% |
| F | 0.2% | 0.1% | 0.2% | 0.1% | 0.2% | 0.2% |
| Fe | 0.3% | 0.1% | 0.2% | 0.2% | 0.1% | 0.1% |
| K | 0.9% | 1.2% | 0.9% | 0.9% | 1.3% | 1.5% |
| Mn | 0.1% | 0.1% | 0.1% | 0.0% | 0.1% | 0.1% |
| Nb | 0.7% | 0.6% | 0.8% | 0.7% | 0.6% | 1.3% |
| O | 59.3% | 59.8% | 60.6% | 56.9% | 64.0% | 54.8% |
| Pd | 0.2% | 0.2% | 0.2% | 0.2% | 0.2% | 0.4% |
| Si | 23.6% | 19.7% | 21.2% | 20.2% | 22.2% | 19.3% |
| Ti | | | | 0.3% | | |
| Zn | 0.1% | 0.2% | 0.2% | 0.1% | 0.1% | 0.3% |
| Zr | 0.1% | | | 0.2% | 0.1% | 0.2% |

*Table 9 – Average weight concentration percentage per test*

| **Element** | **Untreated** | **2°C/min** | **5°C/min** | **10°C/min** | **20°C /min** | **MHC** |
|---|---|---|---|---|---|---|
| Al | 5.7% | 8.9% | 7.7% | 5.9% | 7.1% | 5.8% |
| C | 6.1% | 6.8% | 5.8% | 10.0% | 3.5% | 10.4% |
| Cu | 0.5% | 0.6% | 0.4% | 0.3% | 0.3% | 0.8% |
| F | 0.2% | 0.1% | 0.2% | 0.1% | 0.2% | 0.2% |
| Fe | 0.7% | 0.4% | 0.5% | 0.5% | 0.3% | 0.3% |
| K | 1.7% | 2.3% | 1.6% | 1.9% | 2.5% | 2.9% |
| Mn | 0.2% | 0.3% | 0.2% | 0.1% | 0.2% | 0.2% |
| Nb | 3.4% | 3.0% | 3.7% | 3.3% | 2.9% | 6.0% |
| O | 47.1% | 48.3% | 48.2% | 46.9% | 50.8% | 43.5% |
| Pd | 0.9% | 0.9% | 1.3% | 1.0% | 0.9% | 2.1% |
| Si | 32.9% | 28.0% | 29.6% | 29.2% | 30.9% | 26.8% |
| Ti | | | | 0.7% | | |
| Zn | 0.4% | 0.5% | 0.7% | 0.3% | 0.3% | 0.8% |
| Zr | 0.5% | | | 0.8% | 0.6% | 1.1% |

The SEM imagery, depicted in Figures 36-41, provided a granular view of the sample's microstructure post-testing. Elemental analysis via SEM identified traces of various elements, including Niobium (Nb), Titanium (Ti), Zinc (Zn), Zirconium (Zr), Palladium (Pd), Copper (Cu), and Manganese (Mn). These findings were similar to those from X-ray Diffraction (XRD) testing, suggesting that the presence of these elements could likely be attributed to contamination during the sample preparation phase, specifically the painting process used for digital image correlation. While the samples weren't the same powder used for XRD testing, using larger pieces instead, the hypothesis is that the paint has leached into the larger pieces, potentially through the increased porosity of the samples post treatment.

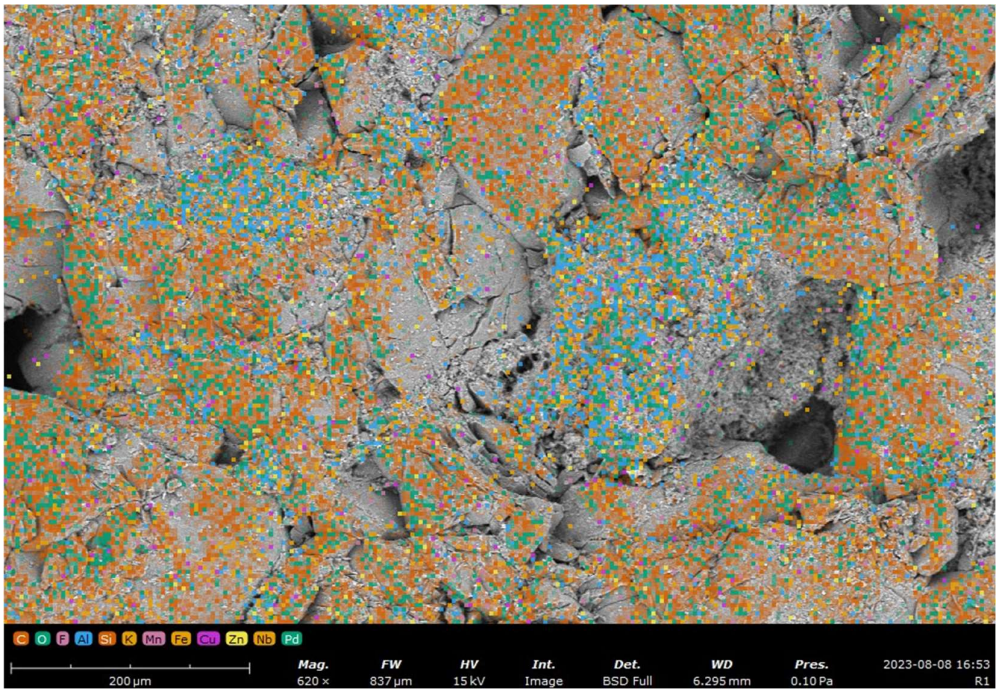


*Figure 36 - Untreated sample # 3 SEM analysis*

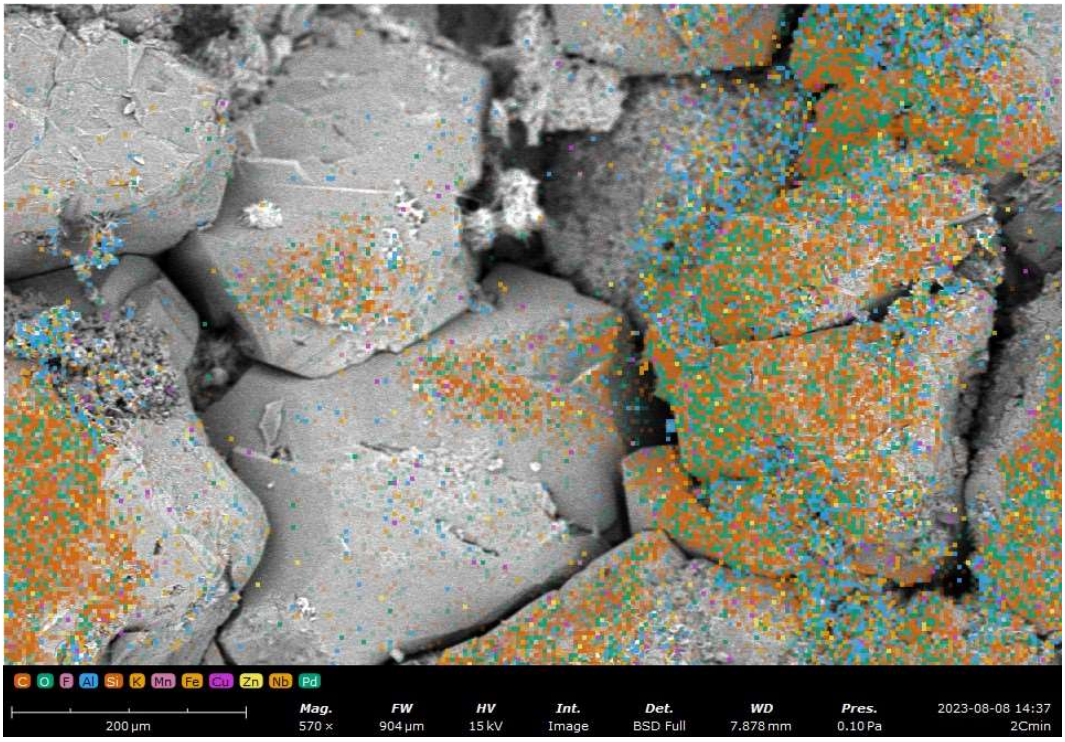


*Figure 37 - 2°C/min sample #1 SEM analysis*

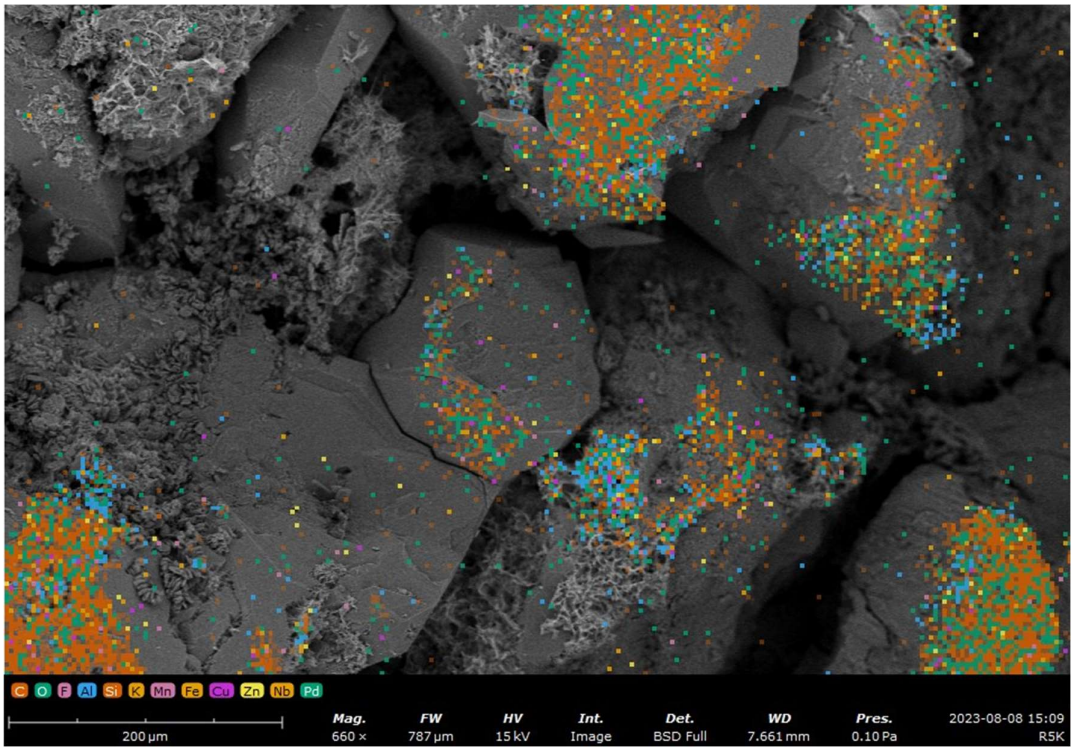


*Figure 38 - 5°C/min sample #2 SEM analysis*

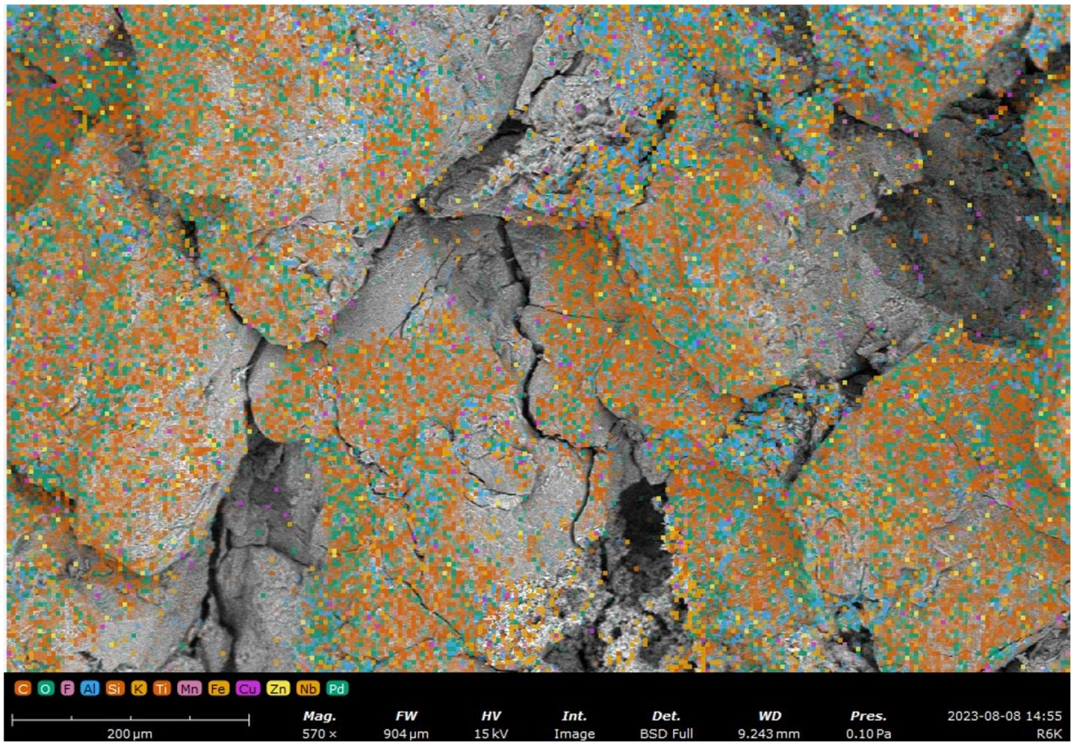


*Figure 39 – 10°C/min sample #3 SEM analysis*

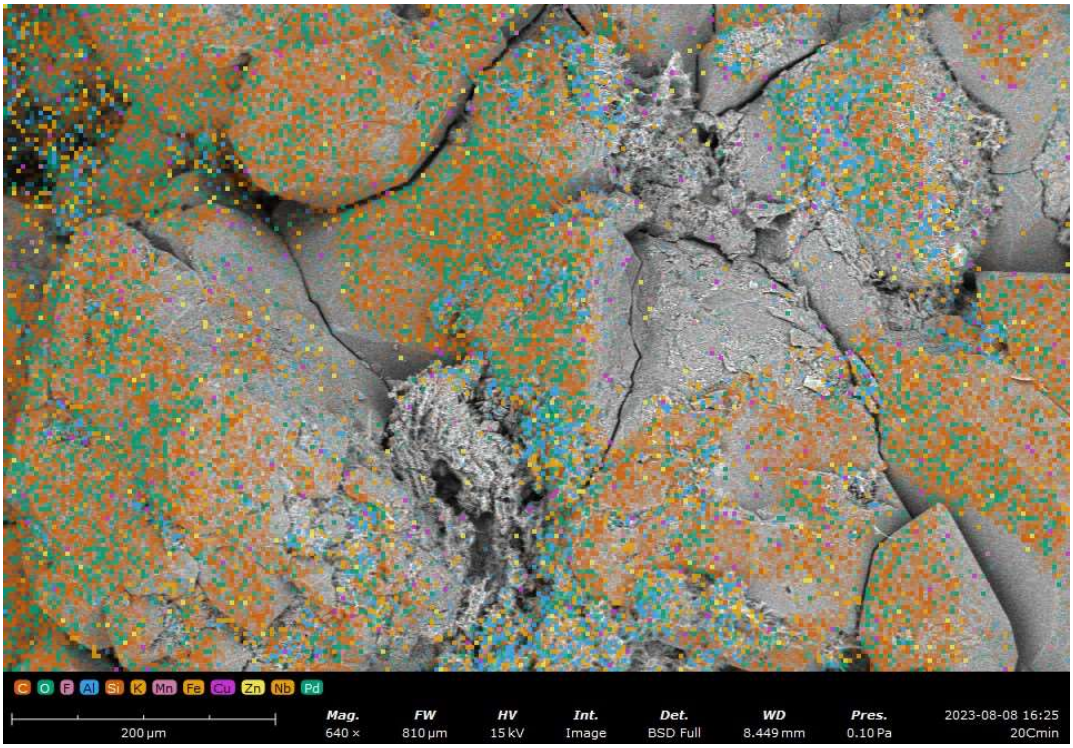


*Figure 40 - 20°C/min Sample #1 SEM analysis*

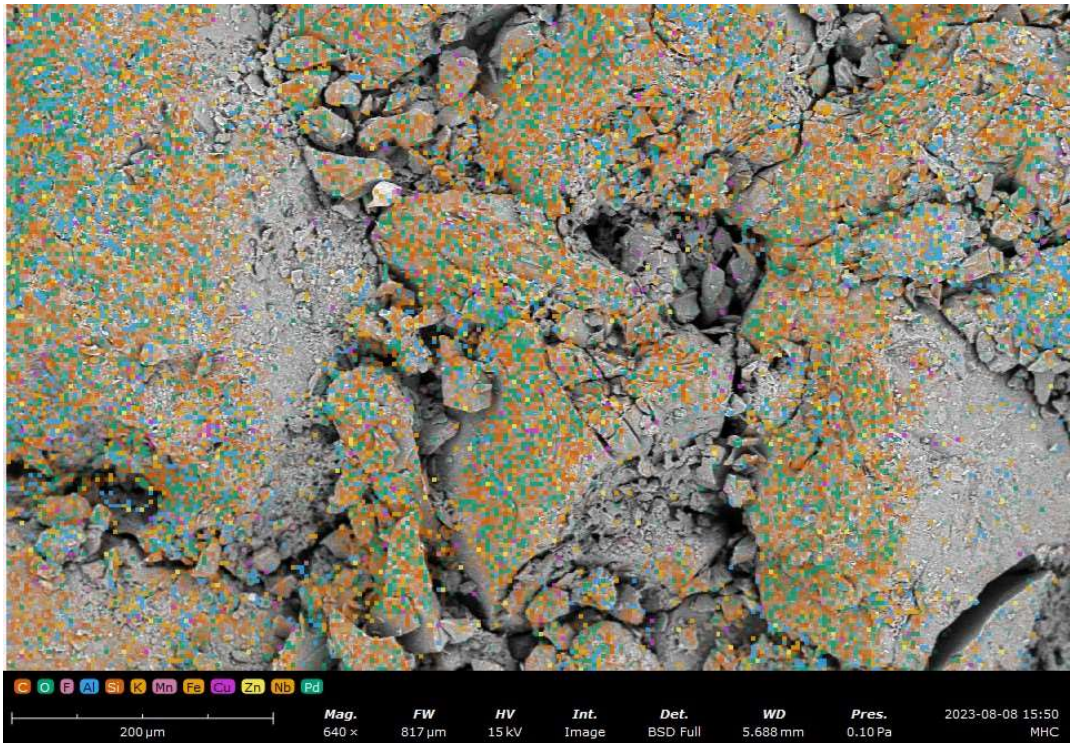


*Figure 41 - MHC Sample #3 SEM analysis*

In terms of the microscale damage there is a clear increase in the number of smaller rock fragments in the Figures 38-40 which are the higher heating rates 10°C/min, 20°C/min and MHC curves. Ultimately this doesn't appear to show the porous shapes observed in part of the literature review but rather a reduction in particle size that could be explained by the thermal shock which was intentionally targeted.

Recognising the potential for such contamination, a methodological refinement could have prevented the contamination, however all testing was done together. This would enable a clearer validation of SEM and XRD outcomes, minimising extraneous variables. Given the low likelihood of these elements occurring naturally within the sandstone, they were omitted from the total elemental summation in the analysis. Subsequently, the data were adjusted to normalise the percentages of the remaining elements, which are characteristic of sandstone. These recalibrated results are detailed in Tables 11 and 12 and illustrated in Figures 42 and 43.

*Table 10 - Atomic concentration percentages after adjustments*

| Element | 1. Untreated | 2. 2°C/min | 3. 5°C/min | 4. 10°C/min | 5. 20°C/min | 6. MHC |
|---|---|---|---|---|---|---|
| Al | 4.4% | 6.8% | 6.0% | 4.4% | 5.5% | 4.5% |
| C | 10.5% | 11.5% | 9.9% | 16.6% | 6.0% | 18.2% |
| O | 60.9% | 61.5% | 62.3% | 58.3% | 65.8% | 57.2% |
| Si | 24.2% | 20.3% | 21.8% | 20.7% | 22.8% | 20.1% |

*Table 11 - Weight concentration percentages after adjustments*

| Element | 1. Untreated | 2. 2°C/min | 3. 5°C/min | 4. 10°C/min | 5. 20°C/min | 6. MHC |
|---|---|---|---|---|---|---|
| Al | 6.2% | 9.7% | 8.5% | 6.4% | 7.7% | 6.7% |
| C | 6.6% | 7.4% | 6.3% | 10.9% | 3.8% | 12.0% |
| O | 51.3% | 52.5% | 52.8% | 51.0% | 55.0% | 50.3% |
| Si | 35.8% | 30.4% | 32.4% | 31.7% | 33.5% | 31.0% |

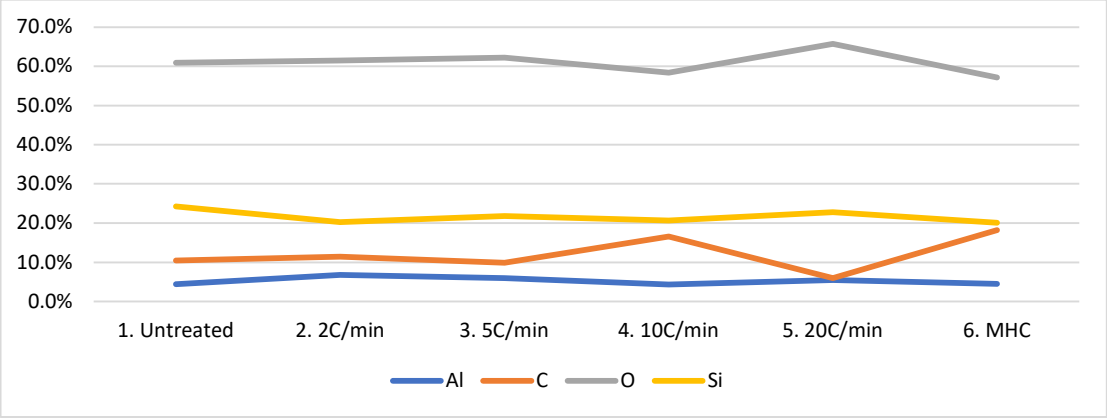


*Figure 42 - Plot of the table of atomic concentration percentage after adjustments*

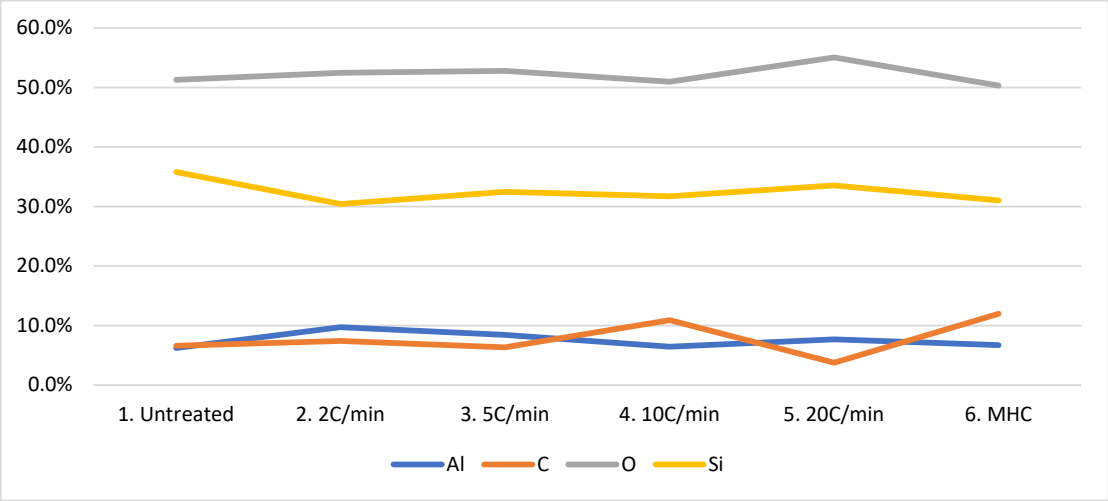


*Figure 43 - Plot of table of weight concentration percentages after adjustments*

A comparative assessment between SEM and XRD results revealed discrepancies that were unanticipated. The primary constituents of sandstone, predominantly $SiO_2$ and its related clay minerals such as those containing aluminium (Al), were expected to align closely with XRD findings. The XRD analysis suggested a reduction in Al and OH compounds, presumably due to the thermal treatments applied. However, the SEM data did not exhibit a consistent pattern correlating with the heat treatment intensities or the specific conditions of the MHC treatment. Silicon (Si) and Oxygen (O) concentrations remained within a narrow 4-5% variance without showing a discernible trend across the different heating profiles, except for a noted decrease in Si and O in the MHC-treated sample, which also coincided with an elevated presence of Carbon (C).

Despite the exclusion of the detected metals and rare earth elements, the SEM analysis did not elucidate a clear trend or correlation with the varying thermal treatment conditions, suggesting the need for further investigation to decipher the microstructural dynamics influenced by heat in sandstone samples.

## 4.7 Applications

The findings of this study, derived from XRD and SEM analyses, reveal a reduction in clay minerals in sandstone samples subjected to all heating scenarios, resulting in an increased proportion of quartz in the residual samples. This phenomenon, hypothesised to occur through dehydration, aligns with conditions typical of geothermal rock formation. Given that the experiments focused on sandstone, a sedimentary rock commonly encountered in tunnelling projects within the Hawkesbury Basin in the greater

Sydney area and beyond, the insights from this research have broad applicability to various tunnelling contexts.

In the event of a tunnel fire, intense heat would impact the rock face, regardless of whether it is exposed or lined with shotcrete or concrete panels. Such heat exposure could induce spalling, particularly under prolonged fire conditions, potentially compromising the protective concrete layers and exposing underlying rock. Notably, catastrophic fire events like the Mont Blanc tunnel tragedy [16] illustrate that fire durations can significantly exceed the four-hour exposure typically considered in construction design, underscoring the variability of heat impact based on the chosen construction method.

Tunnels excavated using drill-and-blast techniques may experience damage zones within the adjacent rock structure, leading to the walls and roof fracturing. This study highlights that porosity and pre-existing microscale fractures, dictated by geological conditions, significantly influence the extent of rock damage under thermal exposure.

Unlike above-ground environments, where heat can dissipate into the atmosphere or be mitigated by wind, underground tunnels trap heat, allowing it to transfer deeper into the rock mass. This heat transfer could subject the exposed rock face to intense heating patterns, such as HC or MHC fire curves. In contrast, deeper rock layers experience more gradual, potentially diminishing heat transfer. The duration of heat retention would depend on firefighting interventions and the thermal conductivity of the surrounding rock mass.

Sedimentary rocks, particularly sandstone, present unique challenges due to their formation in horizontal layers. Tunnel roofs in sedimentary rock often behave as structural beams rather than unified rock masses. The layering can lead to shear failure under thermal contraction, especially in typical bord-and-pillar configurations. Figure 44 illustrates how roof supports, installed to bind the beam-like roof structure, consist of primary supports at depths of 1–2 meters and secondary supports extending to 4–8 meters, anchoring into more stable rock. Heat exposure may degrade the upper layers of the roof, necessitating the replacement of roof bolts to maintain a factor of safety. The tensile weakness inherent to sedimentary rock, particularly at the roof span's midpoint, emphasises the need for proactive reinforcement strategies.

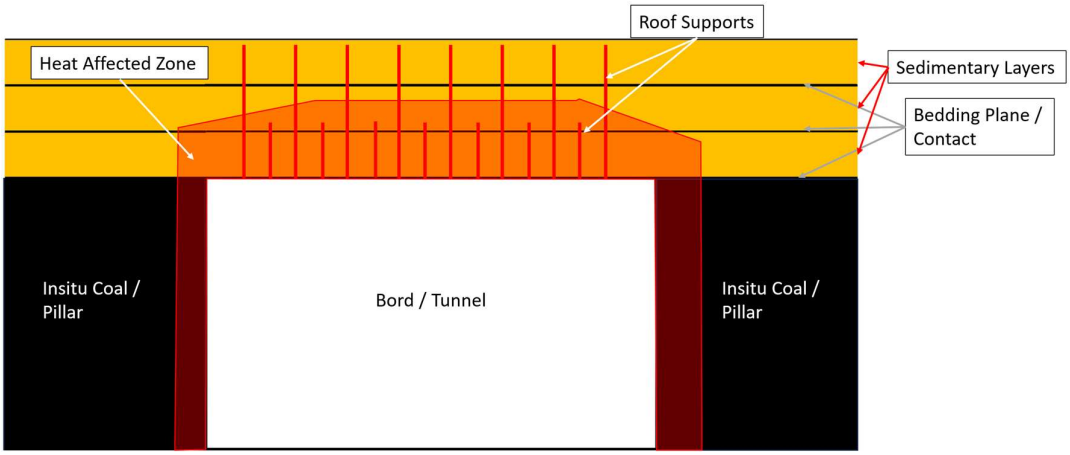


*Figure 44 - Typical cross section of an underground coal tunnel as part of Bord and Pillar mining, showing a geology cross-seciton and heat affected zone*

In underground coal seam gas operations, limited oxygen availability may mitigate initial blaze risk, though doesn't stop underground burning. However, prolonged heat exposure, as described by Yavuz et al. [49], indicates that significant damage to the rock structure may occur within 24 hours. Heat-induced fracturing and dehydration could reduce rock strength, potentially resulting in subsidence. This highlights the importance of integrating field measurements to validate models of deep rock behaviour.

Heating of OH bonds within cylindrical specimens has been shown to cause water evaporation through porous rock. In an underground setting, particularly below the groundwater level, this evaporated water may become trapped, resulting in increased pressure within the rock mass. Water expands at temperatures exceeding 100°C as it converts to vapour, potentially exacerbating structural damage.

For practical and theoretical applications in assessing heat-treated rock, particularly in post-fire scenarios within underground tunnels, modelling software could incorporate directional heat exposure and adjust unconfined compressive strength (UCS) values accordingly. Visual inspections of unlined tunnel rock faces are crucial to identify fractures at both microscopic and macroscopic scales. This study suggests dehydration-induced porosity or volume reduction in the rock may necessitate additional rock bolting to ensure structural integrity. Furthermore, in subsidence modelling for underground coal seam gas operations, additional research into specimen shrinkage is recommended to quantify void creation between sedimentary layers and the corresponding UCS reductions, which could inform long-term subsidence predictions.

# 5. Conclusions and Recommendations

## 5.1 Conclusions from the Present Study

In this research, we investigated and contrasted the effects of thermal shock and linear heating on the mechanical properties of Hawkesbury Sandstone under temperature conditions analogous to those found in hydrocarbon fires. The experimental laboratory findings are summarised as follows:

- All heating scenarios markedly decreased the sandstone's compressive and tensile strengths, with the changes occurring in roughly equivalent ratios. Heating rates of 2°C/min, 5°C/min, and 10°C/min did not yield significantly different outcomes regarding mechanical properties. However, a 20°C/min heating rate resulted in lower UCS and tensile strength, with the MHC showing the largest reductions.
- For UCS, linear heating reduced strength by 18-42% on average, with no clear trend line across the different heating rates. The peak temperature of 1,100°C was reached in all cases, but the MHC experienced the largest reduction in UCS at 79%. Axial strain for untreated was 0.77%, which increased to a range of 1.46-1.72% for treated samples with no clear separation in strain between linear heating and thermal shock.
- For tensile strength, linear heating caused reductions of 56-71% on average, again with no clear trend line based on heating rate. The MHC condition resulted in the largest tensile strength reduction at 82%. Axial strain for untreated samples was 0.45% and sat between 0.45-0.56, showing no considerable separation between any heated or untreated samples.
- The scale effect results observed in both untreated and heat-treated samples demonstrate higher strength values near the d50 value, which aligns with the diameter used in the Hoek and Brown formula. Heat treatment reduced strength across the 15-50mm range, while the 67mm value remained nearly identical post-heat treatment, and the 75mm sample exhibited a slight increase in strength. However, the overall trends do not conform to the predictions of the Hoek and Brown formula. This indicates that the scale effect behaviour for Hawkesbury Sandstone, and potentially other sedimentary rocks, may deviate from the patterns observed in igneous or crystalline rocks. Further investigation is necessary to establish the relationship between sample size and strength for this rock type.

- The X-ray diffraction (XRD) testing revealed a notable increase in quartz content, nearly doubling from 38.4% to an average of approximately 70%. The quartz content escalated further to 81.3% under the MHC, likely influenced by the additional peak temperature of 200°C. This change suggests a significant decrease in clay content, which appears to have contributed to retaining SiO4 structures within the sandstone matrix.
- The crystallinity percentage in the XRD test under the MHC was significantly higher, reaching 80%, with the sample subjected to an extra 200°C. In contrast, other samples, including the untreated reference, showed crystallinity percentages ranging from 66% to 72%.
- The SEM results indicated an unclear correlation between increasing quartz and crystallinity as well as a reduction in aluminium associated with clays. However, the microscale imagery revealed a significant increase in specimen damage, consistent with the understood effects of thermal shock. This suggests that thermal shock intensifies microstructural damage, warranting further detailed analysis to quantify these changes and their implications for geotechnical applications.

From these results, we conclude that heating diminishes the mechanical strength of Hawkesbury Sandstone, with temperatures exceeding 1,100°C, with the heating rate being an important factor in determining the mechanical impacts. Under sustained heating conditions, potentially metamorphic-like inducing changes appear to occur without the high pressure of the environment.

Future investigations should delve into the implications of these findings on a larger scale, particularly within the context of tunnel engineering. Assessing how such thermal effects influence the structural integrity of a tunnel's cross-section, significantly beyond the likely spalling depth in a real tunnel fire scenario, is imperative. Understanding the heat transfer dynamics beyond the tunnel walls could provide insights into how the rock structure experiences thermal effects akin to those observed in our HC, MHC and linear heating experiments. Such studies would enhance our knowledge of geotechnical engineering, particularly in designing and maintaining safe tunnel structures under extreme thermal conditions.

## 5.2 Recommendations for future research

The research undertaken in this project was confined to examining sandstone specimens of a smaller scale in a laboratory setting, which inherently limits its direct applicability to unlined sandstone tunnels specifically. For future research, several avenues could be explored to enhance the understanding of thermal effects on geological materials in tunnel engineering. These areas include:

- Investigating larger rock samples to better measure the transfer of heat as a function of depth may involve dissecting or coring the samples to analyse microscale fracturing and chemical alterations at different depths relative to the point of heat application.
- Applying the same heating protocols to other rock types that are potential candidates for unlined tunnel construction to compare and contrast their thermal response.
- Examining heat transfer in tunnels with different linings, such as shotcrete or shield linings, and assessing how this heat interacts with the surrounding geological structure.
- Conduct heat treatments on sandstone beams and then test their shear strength to simulate the structural weaknesses likely to be encountered in a sandstone tunnel cross-section.
- Experiment with rock specimens with rock bolts installed under tension to observe how the heat from a tunnel fire may influence the bolt and surrounding rock, considering that the expansion of steel bolts could induce further fracturing in the rock mass, independent of other fracture-inducing stresses.

Subsequent studies should aim to extrapolate these findings to more extensive and varied geological contexts, investigating multiple rock types to ascertain if they can be categorised into groups such as sedimentary, igneous, and metamorphic, which is crucial for tunnel engineering applications. Understanding how thermal shock affects the structural integrity of various tunnel configurations and materials is vital to extrapolate beyond the immediate spalling zones which are observed in real-world tunnel fires as the heat has nowhere to go when deep underground. By expanding research to include different rock types and tunnel linings, the field can broaden its repository of knowledge,

aiding geotechnical engineers in designing and maintaining tunnels that are resilient to the hopefully infrequent but intense thermal events.

## 5.3 Publications

A portion of this research was submitted as a conference paper to the Australian Centre for Geomechanics' conference Third International Slop Stability in Mining Conference (SSIM 2023) in November 2023 under the title: *Tensile strength of Hawkesbury sandstone exposed to high temperatures: Considerations for exposed mine batters* (Submitted) using two data sets from the tensile testing data in this research.

An additional portion was submitted as a journal paper by P.L.P. Wasantha, K. Cranfield-Brooks, M. Guerrieri, W.G.P. Kumari, T. Xu (Submitted). *Investigating the Effect of Fire Exposure on the Mechanical Characteristics of Hawkesbury Sandstone: Insights from Experimental Analysis, Rock Mechanics and Rock Engineering.*

# 6. References


[1] N. Buddoo, “Future of Tunnelling | Australia grapples with construction boom,” 5 October 2021. [Online]. Available: https://www.newcivilengineer.com/the-future-of/future-of-tunnelling-australia-grapples-with-construction-boom-05-10-2021/.

[2] E. Hardy, “Going down: Australia’s tunnel projects,” Engineers Australia, 12 July 2023. [Online]. Available: https://createdigital.org.au/going-down-australias-tunnel-projects/. [Accessed 1 April 2024].

[3] L. S. S. F. K. M. Z. Z. Ofira Ayalon, “Evaluating Market Benefits of Transportation Tunnels—The Carmel Tunnels as a Case Study,” *Journal of Environmental Protection,* vol. 7, no. 10, p. 1259, 2016.

[4] A. Kauranen, “Finland counted its bomb shelters and found 50,500 of them,” Reuters, 30 August 2023. [Online]. Available: https://www.reuters.com/world/europe/finland-counted-its-bomb-shelters-found-50500-them-2023-08-29/. [Accessed 1 April 2024].

[5] S. El-Showk, “Final Resting Place,” *Science,* vol. 375, no. 6583, pp. 806-810, 2022.

[6] L. Buckmaster and J. Simon-Davies, “Australia's future population,” Parliament of Australia, 10 October 2010. [Online]. Available: https://www.aph.gov.au/About_Parliament/Parliamentary_Departments/Parliamentary_Library/pubs/BriefingBook43p/futurepopulation. [Accessed 1 April 2024].

[7] STEP Inc, “Hawkesbury Sandstone,” [Online]. Available: https://www.step.org.au/images/STEPimages/PDFdownloads/RocksTrees.pdf. [Accessed 1 April 2024].

[8] Transport NSW, “Tunnelling under Sydney Harbour - Fact Sheet,” July 2023. [Online]. Available: https://media.caapp.com.au/pdf/8xcng7/a9891cad-f209-4c4f-a544-e2e8539ef602/WHT%20Stage%202%20Modification%20%20Tunnelling%20under%20Sydney%20Harbour%20%28Jul%202023%29.pdf. [Accessed 1 April 2024].

[9] Structurae, “Zambele Tunnel,” Structurae, 20 February 2016. [Online]. Available: https://structurae.net/en/structures/zambele-tunnel. [Accessed 29 April 2024].

[10] Curtis Concrete Pumping, “Shotcrete Linings for Culverts & Tunnels,” Unknown. [Online]. Available: https://www.curtisconcretepumping.com/culvert-tunnel-shotcrete-linings/. [Accessed 2022 September 28].

[11] N. Cranenburgh, “The engineering behind Melbourne’s groundbreaking Metro Tunnel project,” Create Digital, 7 April 2021. [Online]. Available:

https://createdigital.org.au/engineering-behind-groundbreaking-metro-tunnel-project/. [Accessed 28 September 2022].

[12] R. G. Bhawani Singh, "Chapter 14 - Rock Mass Quality for Open Tunnel Boring Machines," in *Engineering Rock Mass Classification*, Butterworth-Heinemann, 2012, pp. 185-191.

[13] Victoria University, "FIRE TEST FACILITIES," [Online]. Available: https://www.vu.edu.au/research/researching-at-vu/laboratories-facilities/fire-test-facilities. [Accessed 11 September 2022].

[14] S. Harms and H. Konietzky, "Shotcrete in tunnelling and mining," TU Bergakademie Freiberg, Geotechnical Institute, Freiberg, Germany, 2020.

[15] K. Larsson, "Fires in tunnels and their effect on rock - A review," Luleå University of Technology Department of Civil and Environmental Engineering, Luleå, Sweden, 2006.

[16] P. Capella, "35 die, 1 Briton missing in Mont Blanc tunnel fire," The Guardian, 27 Mar 1999. [Online]. Available: https://www.theguardian.com/world/1999/mar/27/6. [Accessed 28 September 2022].

[17] M. Gardiner, "A Deadly Blaze in the Alps Made a Biker a Hero and Tunnels Safer for All," The New York Times, 21 March 2019. [Online]. Available: https://www.nytimes.com/2019/03/21/business/mont-blanc-tunnel-fire-anniversary-rescue.html. [Accessed 28 September 2022].

[18] Promat, "International fire curves – useful tool for designing fire safety," 6 February 2020. [Online]. Available: https://www.promat.com/en-au/construction/projects/expert-area/33637/international-fire-curves-fire-safety/. [Accessed 11 September 2022].

[19] Geoengineer.org, "Unconfined Compression Test," Geoengineer.org, [Online]. Available: https://www.geoengineer.org/education/laboratory-testing/unconfined-compression-test. [Accessed 11 September 2022].

[20] S. Australia, "AS 4133.4.2.1-2007 - Methods of testing rocks for engineering purposes Rock strength tests - Determination of uniaxial compressive strength of 50 MPa and greater," 6 June 2019. [Online]. Available: https://infostore.saiglobal.com/en-us/standards/as-4133-4-2-1-2007-122052_saig_as_as_256158/. [Accessed 12 October 2022].

[21] Geoengineer.org, "Splitting Tensile Strength Test (Brazilian)," Geoengineer.org, [Online]. Available: https://www.geoengineer.org/education/laboratory-testing/splitting-tensile-strength-test-brazilian. [Accessed 11 September 2022].

[22] S. Australia, "AS 1012.10-2000 - Methods of testing concrete Determination of indirect tensile strength of concrete cylinders ('Brazil' or splitting test)

(Reconfirmed 2014)," 18 May 2000. [Online]. Available: https://infostore.saiglobal.com/en-us/standards/as-1012-10-2000-129179_saig_as_as_273253/. [Accessed 12 October 2022].

[23] CSIRO, "Mineralogical services," CSIRO, [Online]. Available: https://www.csiro.au/en/work-with-us/services/testing-and-certification/mineralogical-services. [Accessed 28 September 2022].

[24] L. T. Inc., "SCANNING ELECTRON MICROSCOPY," 2022. [Online]. Available: https://labtesting.com/services/materials-testing/metallurgical-testing/sem-analysis/. [Accessed 28 September 2022].

[25] H. L. Y. Z. &. L. A. Ingason, "Runehamar Tunnel Fire Tests," *Fire Safety Journal,* vol. 71, pp. 134-149, 2015.

[26] Heinen, "Fire resistance – HCM," Heinen, 2022. [Online]. Available: https://www.heinen-doors.com/en/performances/fire-resistance-hcm/. [Accessed 11 September 2022].

[27] P. G. M. a. X. T. Wasantha, "Effects of tunnel fires on the mechanical behaviour of rocks in the vicinity - A review," *Tunnelling and Underground Space Technology,* vol. 108, 2021.

[28] J. F. A. N. D. D. a. Y. G. Li Zhi, "Physical and mechanical properties of thermally cracked andesite under pressure," *Rock Mechanics and Rock Engineering,* vol. 52, no. 10, pp. 3509-3529, 2019.

[29] J. X. S Liu, "An experimental study on the physico-mechanical properties of two post-high-temperature rocks," *Engineering Geology,* vol. 185, pp. 63-70, 2015.

[30] A. M. M. D. W. R. S. a. T. E. Yang Lintao, "Effect of high temperatures on sandstone – a computed tomography scan study," *International Journal of Physical Modelling in Geotechnics,* vol. 17, no. 2, pp. 75-90, 2017.

[31] Y. Y. S. C. C. S. W. H. Wei S, "Experimental study of the effect of high temperature on the mechanical properties of coarse sandstone," *Applied Sciences,* vol. 9, no. 12, p. 2424, 2019.

[32] V. T. R. I. S. &. A. J. Brotóns, "Temperature influence on the physical and mechanical properties of a porous rock: San Julian's calcarenite," *Enginering Geology,* vol. 167, pp. 117-127, 2013.

[33] J. Q. L. L. Z. Hao, "Effect of thermal treatment on physical and mechanical properties of sandstone for thermal energy storage: a comprehensive experimental study," *Acta Geotech,* vol. 17, p. 3887–3908, 2022.

[34] R. W. Y. Z. L. L. B. L. K. L. P. a. W. Y. Lei, "The evolution of sandstone microstructure and mechanical properties with thermal damage," *Energy Science & Engineering,* vol. 7, no. 6, pp. 3058-3075, 2019.

[35] Z. F. J. N. A. D. D. &. G. Y. Li, “Physical and Mechanical Properties of Thermally Cracked Andesite Under Pressure,” *Rock Mechanics and Rock Engineering,* vol. 52, no. 10, pp. 3509-3529, 2019.

[36] Y. M. A. M. W. D. S. R. &. E. T. Lintao, “Effect of high temperatures on sandstone – a computed tomography scan study,” *International Journal of Physical Modelling in Geotechnics,* vol. 17, no. 2, pp. 1-16, 2017.

[37] P. V. D. C. B. a. P. M. Ranjith, “Transformation plasticity and the effect of temperature on the mechanical behaviour of Hawkesbury sandstone at atmospheric pressure,” *Engineering Geology,* vol. 161, pp. 120-127, 2012.

[38] A.-b. Jin, S.-l. Wang, Y.-d. Wei, H. Sun and L.-c. Wei, “Effect of different cooling conditions on physical and mechanical properties of high-temperature sandstone,” *Rock and Soil Mechanics,* vol. 41, no. 11, 2020.

[39] Q. Rao, Z. Wang, H.-f. Xie and Q. Xie, “Experimental study of mechanical properties of sandstone at high temperature,” *Journal of Central South University of Technology,* vol. 14, pp. 478-483, 2007.

[40] C. Lu, Q. Sun, W. Zhang, J. Geng, Y. Qi and L. Lu, “The effect of high temperature on tensile strength of sandstone,” *Applied Thermal Engineering,* no. 111, pp. 573-579, 2017.

[41] S. Qang, L. Wang, B. Ren, K. Ding, C. Jiang and J. Guo, “Mechanical behavior and fracture characteristics of high-temperature sandstone under true triaxial loading conditions,” *Journal of Materials Research and Technology,* no. 28, pp. 569-581, 2024.

[42] T. Zhu, H. Jing, H. Su and Q. Yin, “Physical and mechanical properties of sandstone containing a single fissure after exposure to high temperatures,” *International Journal of Mining Science and Technology,* vol. 2, no. 26, pp. 319-325, 2016.

[43] J. Xu, W.-L. Tian, Y.-S. Bu and J. Yang, “Experimental study on mechanical properties and microscopic mechanisms of layered sandstone after high temperature water cooling,” *Frontiers in Earth Science,* vol. 12, 2024.

[44] M. J. Y. L. A. L. K.-U. H. P. G. M. D. B. D. S. H. a. F. W. Heap, “The influence of thermal-stressing (up to 1000 °C) on the physical, mechanical, and chemical properties of siliceous-aggregate, high-strength concrete,” *Construction and Building Materials,* no. 42, pp. 248-265, 2013.

[45] A. Ozguven and Y. Ozcelik, “Effects of high temperature on physico-mechanical properties of Turkish natural building stones,” *Engineering Geology,* no. 183, pp. 127-136, 2014.

[46] S. Q. Y. D. a. Z. W. Zhao F, "Thermal effects on failure characteristics of," *Geotechnical Research,* vol. 6, no. 4, pp. 302-311, 2019.

[47] S. Q. H. S. G. J. L. C. Zhang W, "Experimental study on the variation of physical and mechanical properties of rock after high temperature treatment," *Applied Thermal Engineering,* vol. 98, pp. 1297-1304, 2016.

[48] H. D. S. &. C. S. Yavuz, "Thermal effect on the physical properties of carbonate rocks," *International Journal of Rock Mechanics and Mining Sciences,* vol. 47, no. 1, pp. 94-103, 2010.

[49] S. Australia, "AS 3600:2018 - Concrete structures," 29 June 2018. [Online]. Available: https://store.standards.org.au/product/as-3600-2018. [Accessed 12 October 2022].

[50] G. Preston, "Explaining exploration: what is drilling?," Kitco, 15 May 2022. [Online]. Available: https://www.kitco.com/commentaries/2020-01-29/Explaining-exploration-what-is-drilling.html#:~:text=Typically%2C%20mineral%20exploration%20projects%20will,known%20as%20%27HQ%27%20size.. [Accessed 2 October 2022].

[51] J. L. J. S. C. Y. Hongxing Han, "Influence of Scale Effect on Strength and Deformation Characteristics of Rockfill Materials," *Materials,* vol. 15, no. 15, p. 5467, 2022.

[52] J. a. M. C. Rusnak, "Using the point load test to determine the uniaxial compressive strength of coal measure rock," National Institute for Occupational Safety and Health & Peabody Group, St. Louis, MO & Pittsburgh, PA, 2000.

[53] K. P. R. J. Z. S. &. S. S. Thuro, "Scale effects in rock strength properties. Part 1: Unconfined compressive test and Brazilian test.," *ISRM regional symposium, EUROCK,* pp. 169-174, 2001.

[54] E. a. N. H. Tuncay, "The effect of length to diameter ratio of test specimens on the uniaxial compressive strength of rock.," *Bulletin of engineering geology and the environment,* vol. 4, no. 68, pp. 491-497, 2009.

[55] H. a. Brown, Underground excavations in rock, London: Instn Min. Metall., 1980.

[56] G. Walton, "Scale Effects Observed in Compression Testing of Stanstead Granite Including Post-peak Strength and Dilatancy," *Geotechnical and Geological Engineering,* vol. 36, pp. 1091-1111, 2018.

[57] R. J. A. S. J. M. A. S. Goudie, "The relations between modulus of elasticity and temperature in the context of the experimental simulation of rock weathering by fire," *Goudie, A. S., R. J. Allison, and S. J. McLaren. "The relations between modulus of elasticity and temperature in the context of the experimental simulation*

*of rock weathering by fire." Earth Surface Processes and Landforms,* vol. 17, no. 6, pp. 605-615, 1992.

[58] E. Blackwelder, "Fire as an agent in rock weathering," *The Journal of Geology,* vol. 35, no. 2, pp. 134-140, 1927.

[59] M. R. B. R. Buckman S, "Buckman S, Morris RH, Bourman RP. Fire-induced rock spalling as a mechanism of weathering responsible for flared slope and inselberg development," *Nature communications,* vol. 12, no. 1, pp. 1-14, 2021.

[60] J. F. R. U. Elizabeth Burton, "Best Practices in Underground Coal Gasification," 6 June 2010. [Online]. Available: https://www.purdue.edu/discoverypark/energy/assets/pdfs/cctr/BestPracticesinUCG-draft.pdf. [Accessed 1 September 2022].

[61] M. W. M. a. K. J. Sury, "Reviews of environmental issues of underground coal gasification - best practice guide," Department of Trade and Industry, London, 2004.

[62] D. Stephens, "An Introduction to Underground Coal Gasification," Lawrence Livermore National Laboratory, Livermore, CA, 1980.

[63] M. D. M. K. J. F. P. &. B. M. Laciak, "he Prediction of Possibilities of CO Poisoning and Explosion during Syngas Leakage in the UCG Process," *Processes,* vol. 9, no. 11, p. 1912, 2021.

[64] University of Calgary, "Coal Types," Energy Education, [Online]. Available: https://energyeducation.ca/encyclopedia/Coal_types. [Accessed 7 April 2024].

[65] A. Korre, S. Durucan and Z. Nie, "Life cycle environmental impact assessment of coupled underground coal gasification and CO2 capture and storage: Alternative end uses for the UCG product gases," *International Journal of Greenhouse Gas Control,* vol. 91, 2019.

[66] A. Kumar, "Overview Of Underground Coal Gasification (UCG) – For A Promising Future Of India," *International Journal of Engineering Applied Sciences and Technology,* vol. 6, no. 3, pp. 161-166, 2021.

[67] CSIRO, "Tutorial on Underground Coal Gasification (UCG)," 12 November 2006. [Online]. Available: https://fossil.energy.gov/international/Publications/Tutorial_UCG_Session1_12Nov06.pdf. [Accessed 7 April 2024].

[68] M. H. Y. L. D. J. C. W. Q. &. W. Y. Wang, "A Study on the Heat Transfer of Surrounding Rock-Supporting Structures in High-Geothermal Tunnels," *Wang, M., Hu, Y., Liu, D., Jiang, C., Wang, Q., & Wang, Y. (2020). A study on the heat transfer of surrounding rock-supporting structures in high-geothermal tunnels. Applied Sciences,* vol. 10, no. 7, p. 2307, 2020.

[69] Victoria University, “FIRE TEST FACILITIES,” [Online]. Available: https://www.vu.edu.au/research/researching-at-vu/laboratories-facilities/fire-test-facilities. [Accessed 29 April 2024].

[70] The University of Melbourne, “X-ray diffraction (XRD),” 2023. [Online]. Available: https://eng.unimelb.edu.au/nanomaterials/capabilities/xray-characterisation/x-ray-diffraction-xrd. [Accessed 29 October 2023].

[71] Victoria University, “VU FIRE-TESTING EXPERTISE,” 14 March 2019. [Online]. Available: https://www.vu.edu.au/about-vu/news-events/news/vu-fire-testing-expertise.

[72] Z. X. Y. a. C. P. L. Ji Yong Xing, “Safety Analysis of Shield Tunnel Segment Lining Based on Field Test,” IOP Conference Series: Earth and Environmental Science, Singapore, 2017.

[73] FIRE EXTINGUISHER ONLINE, “Lithium Ion Battery Fire Safety Explained | Electric car, smartphone, laptop,” fireextinguisher, 18 March 2022. [Online]. Available: https://www.fireextinguisheronline.com.au/blog/post/lithium-ion-battery-fire-safety. [Accessed 11 September 2022].

[74] C. Lampton, “What are the dangers of hydrogen-powered vehicles?,” HowStuffWorks, [Online]. Available: https://auto.howstuffworks.com/fuel-efficiency/alternative-fuels/hydrogen-vehicle-danger2.htm. [Accessed 11 September 2022].

[75] Geoengineer.org, “Triaxial Compression Test in Rock,” Geoengineer.org, [Online]. Available: https://www.geoengineer.org/education/laboratory-testing/triaxial-compression-test-in-rock. [Accessed 11 September 2022].

[76] S. YAGIZ, “P-wave velocity test for assessment of geotechnical properties of,” *Bulletin of Materials Science,* vol. 34, no. 4, pp. 947-953, 2011.

[77] Structurae - International Database and Gallery of Structures, “Årstadalstunneln,” 21 September 2016. [Online]. Available: https://structurae.net/en/structures/arstadalstunneln. [Accessed 28 September 2022].

[78] M. G. T. X. P.L.P. Wasantha, “Effects of tunnel fires on the mechanical behaviour of rocks in the vicinity – A review,” *Tunnelling and Underground Space Technology,* vol. 108, 2021.

# 7. Appendices

*Figure 45 - 15 & 32mm core samples prior to heat treatment*

*Figure 46 – 50, 67 and 75mm core samples prior to heat treatment*

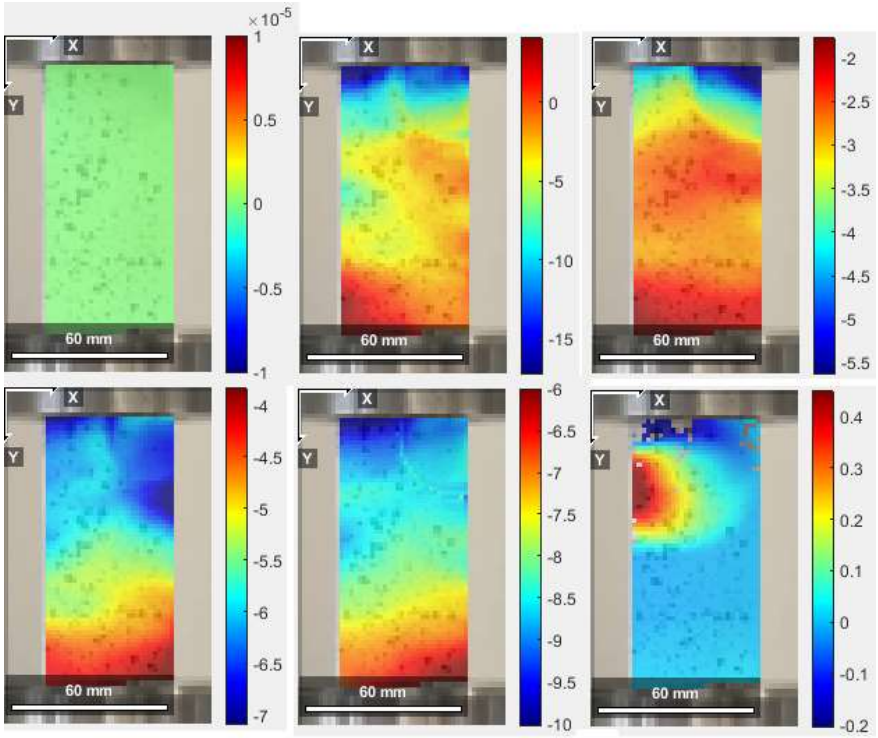


*Figure 47 – Eyy strain plot using Green-Lagrangian method - 2°C/min 50mm Sample #2*

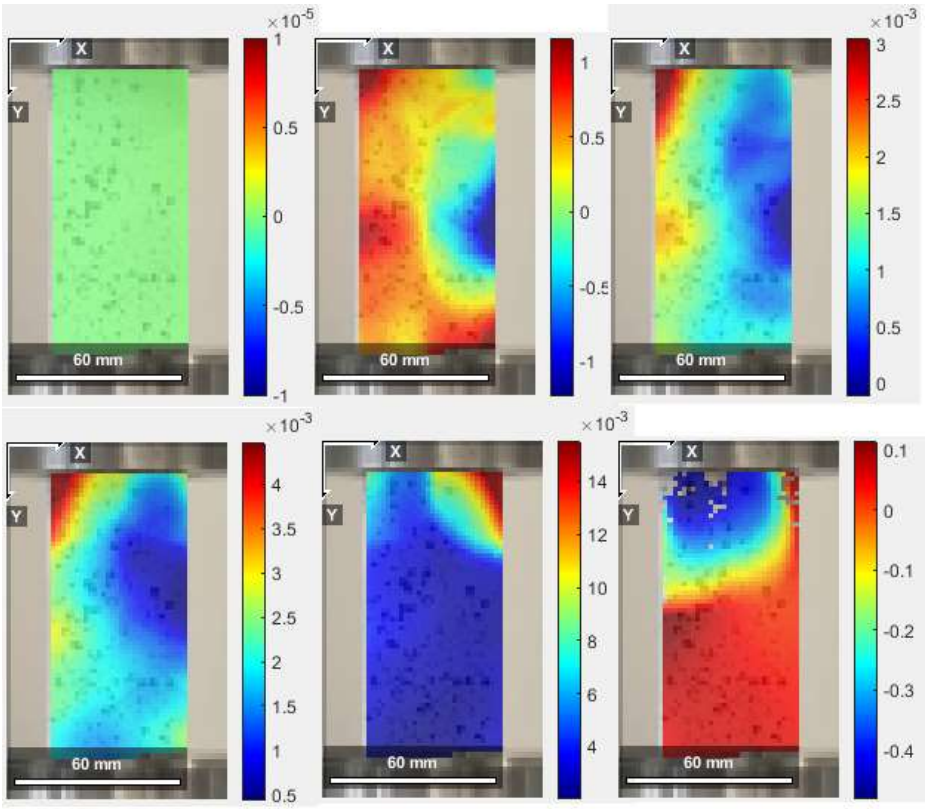


*Figure 48 - Exx strain plot using Green-Lagrangian method - 2°C/min 50mm Sample #2*

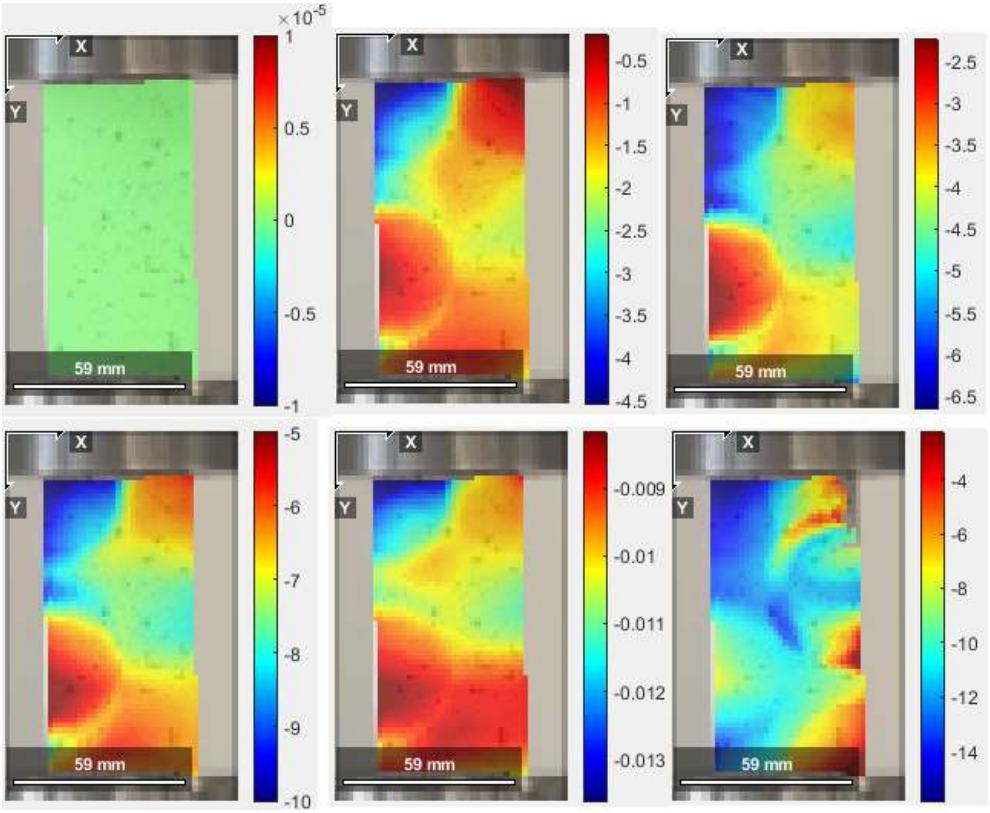


*Figure 49 - Eyy strain plot using Green-Lagrangian method - 5°C/min 50mm Sample #1*

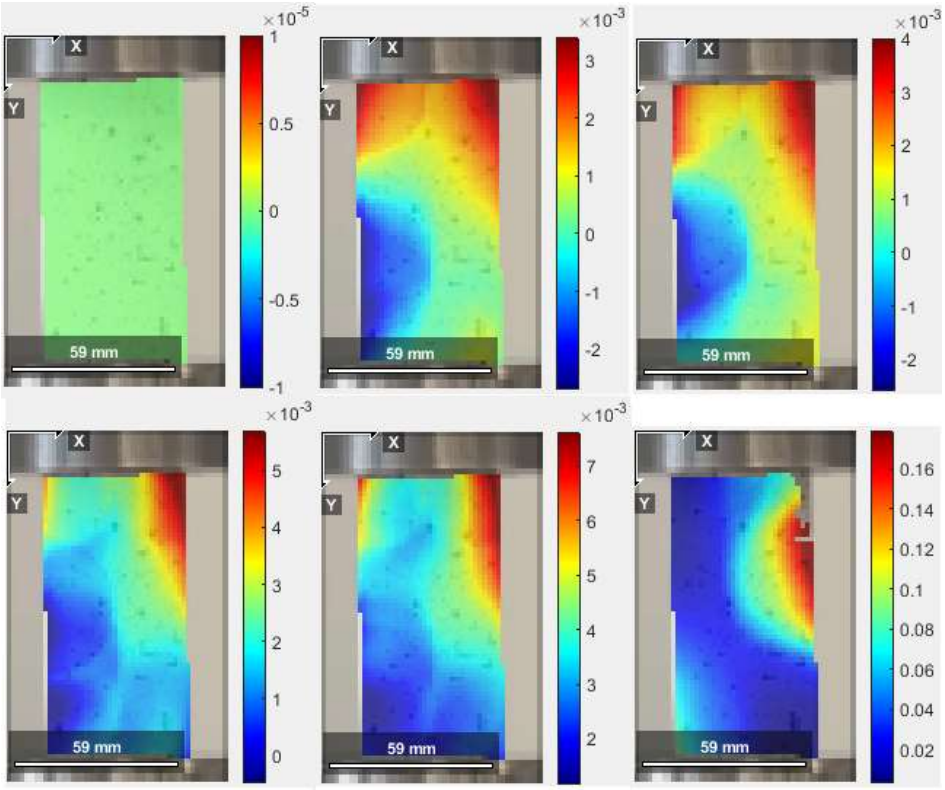


*Figure 50 - Exx strain plot using Green-Lagrangian method - 5°C/min 50mm Sample #1*

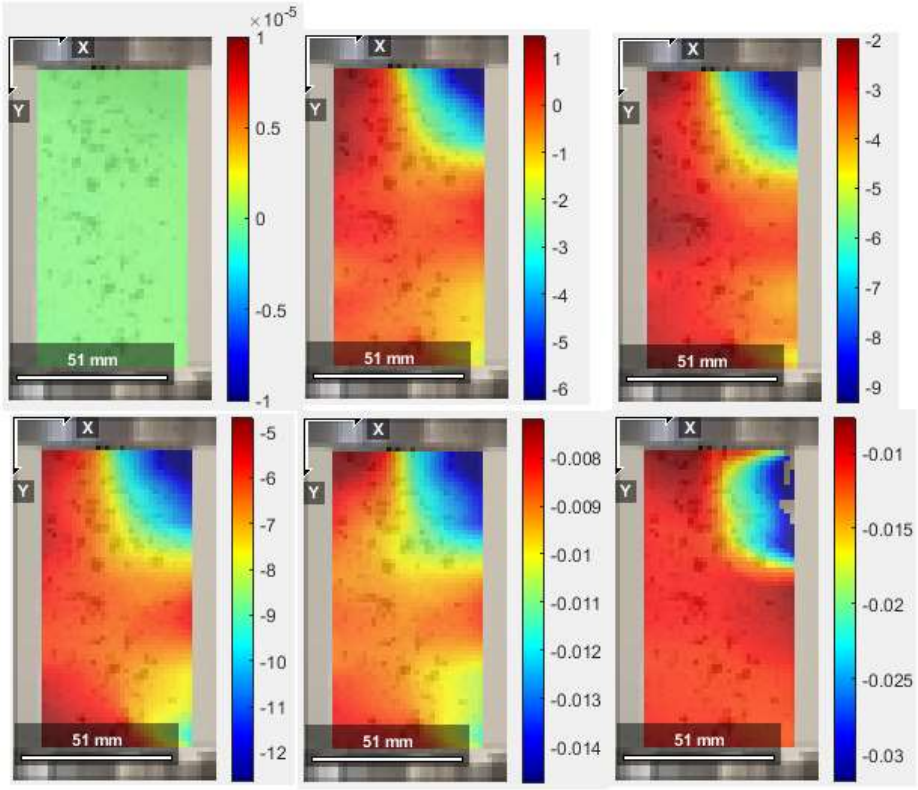


*Figure 51 - Eyy strain plot using Green-Lagrangian method - 10°C/min 50mm Sample #3*

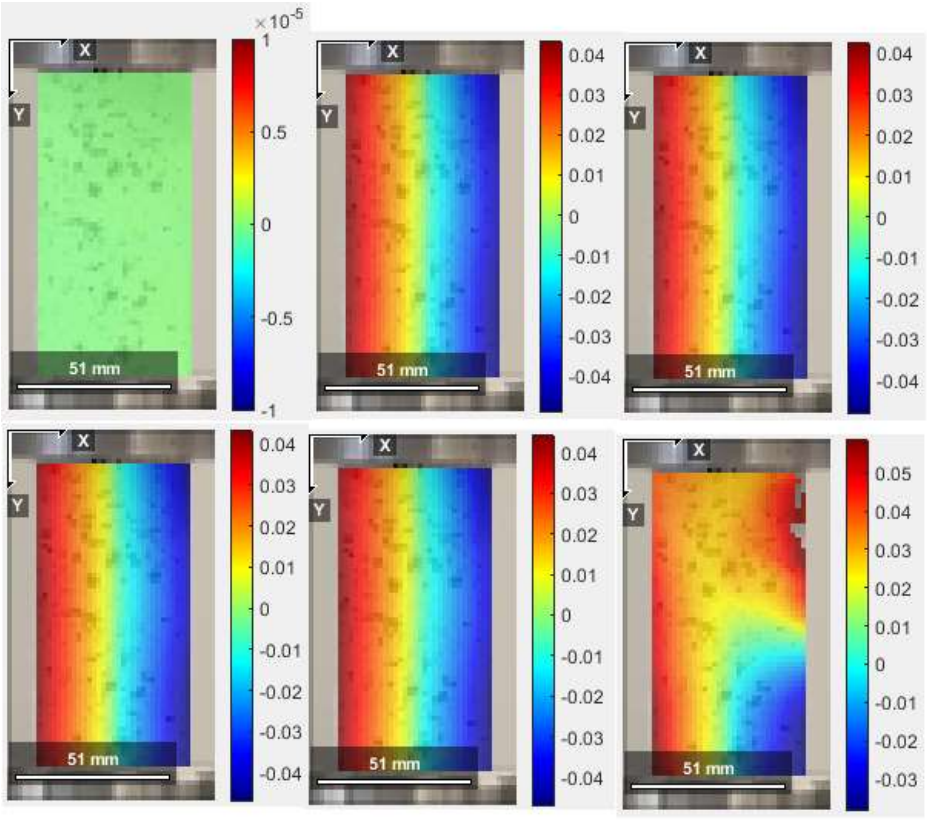


*Figure 52 - Exx strain plot using Green-Lagrangian method - 10°C/min 50mm Sample #3*

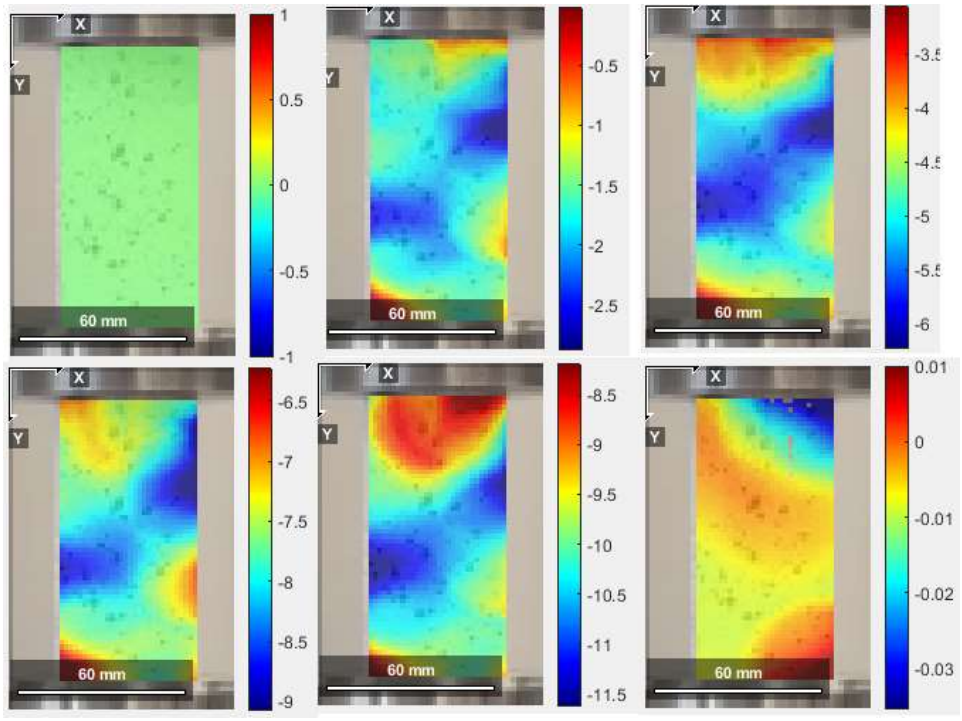


*Figure 53 - Eyy strain plot using Green-Lagrangian method - 20°C/min 50mm Sample #1*

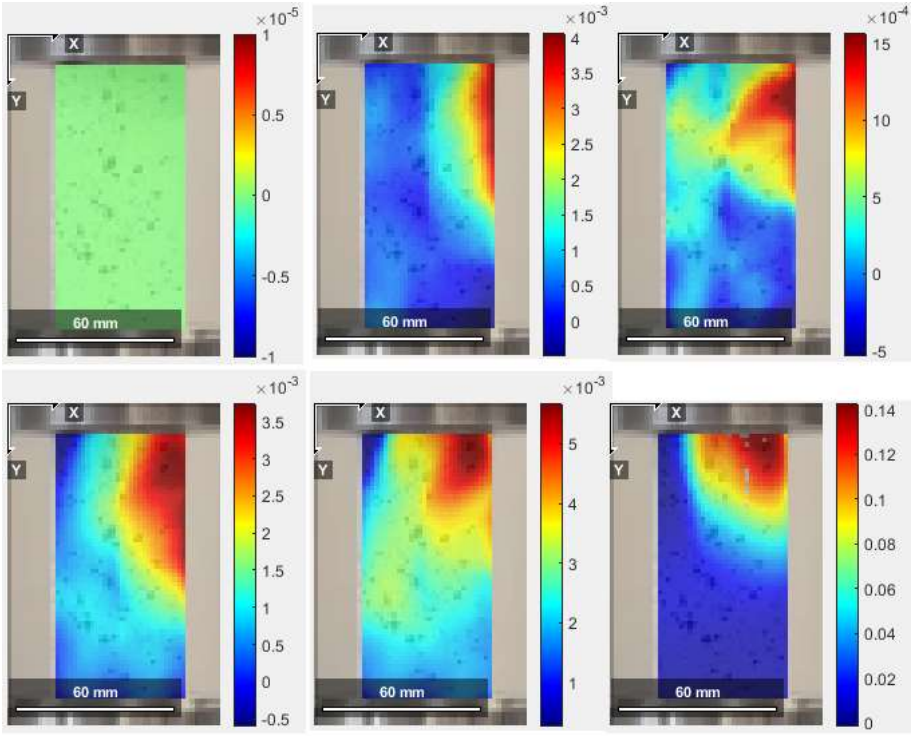


*Figure 54 - Exx strain plot using Green-Lagrangian method - 20°C/min 50mm Sample #1*

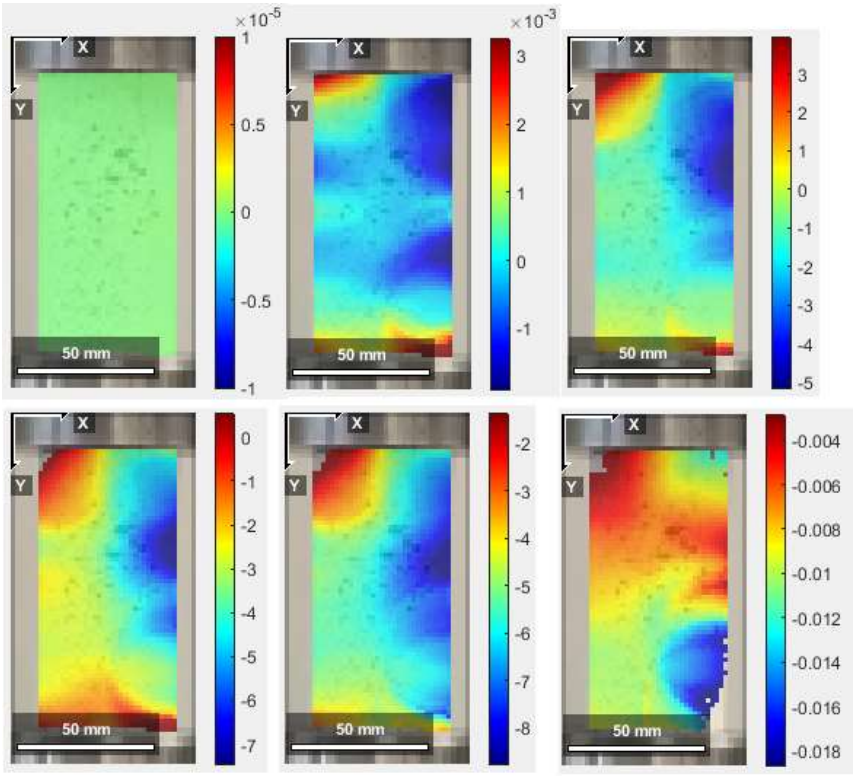


*Figure 55 – Eyy strain plot using Green-Lagrangian method - MHC 50mm Sample #1*

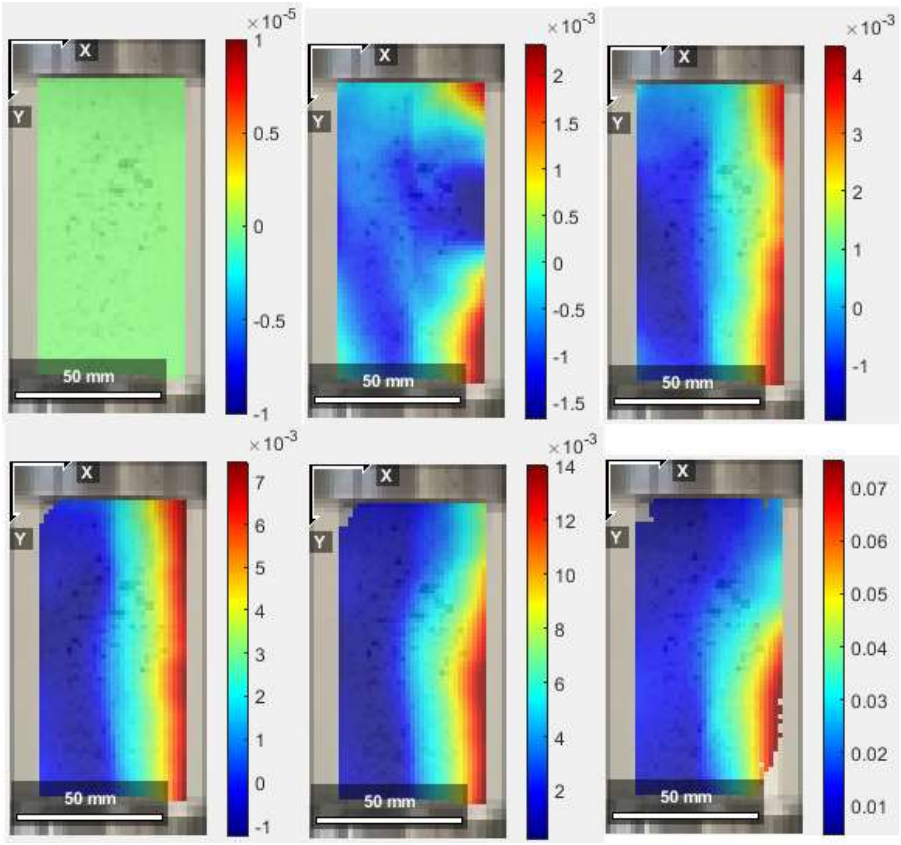


*Figure 56 - Exx strain plot using Green-Lagrangian method - MHC 50mm Sample #1*

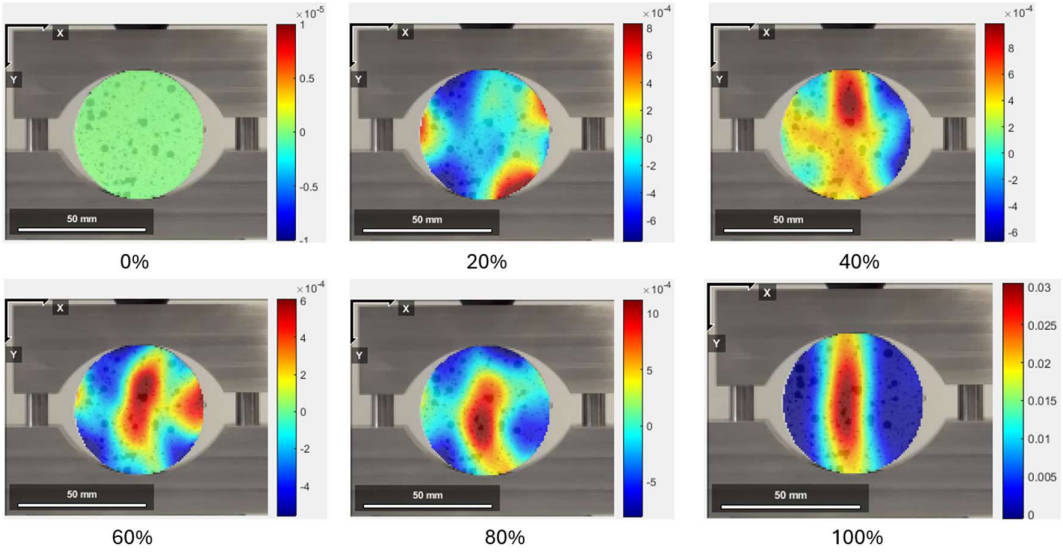


*Figure 57 - Exx strain plot using Green-Lagrangian method - Untreated 50mm Sample #1*

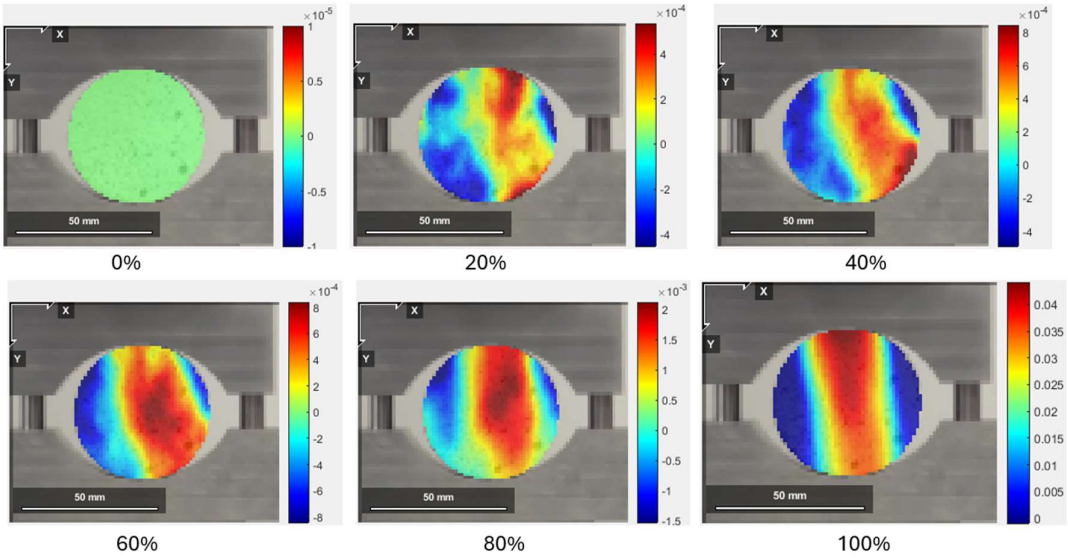


*Figure 58 - Exx strain plot using Green-Lagrangian method - Untreated 50mm Sample #2*

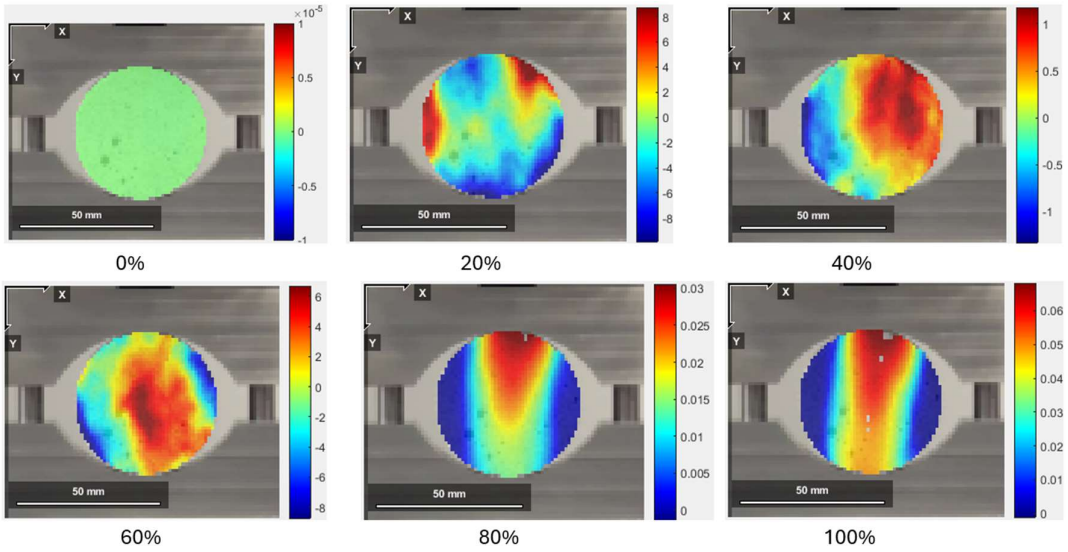


*Figure 59 - Exx strain plot using Green-Lagrangian method - Untreated 50mm Sample #3*

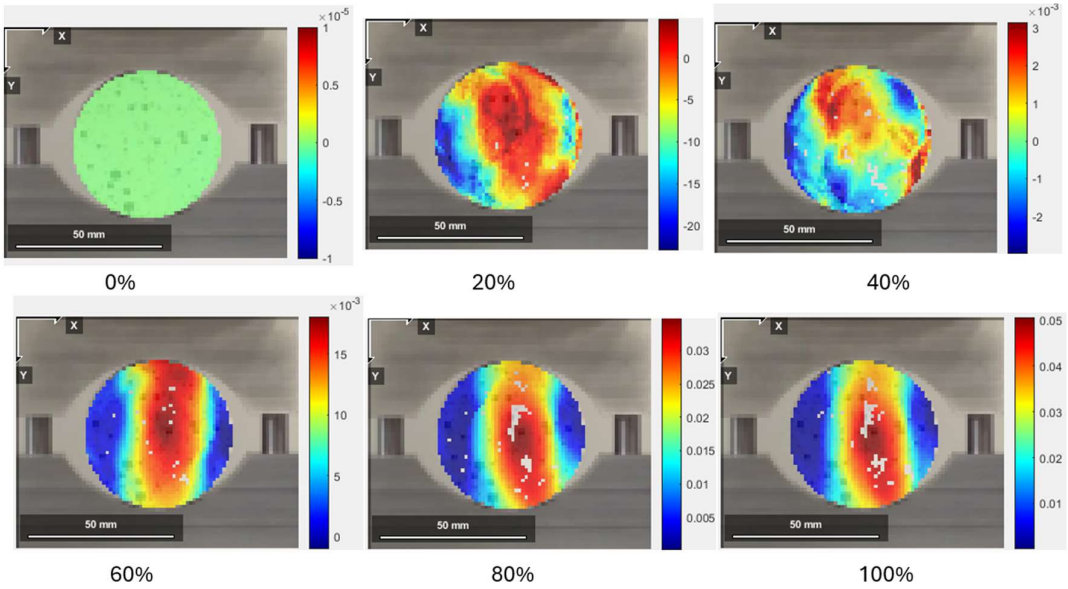


*Figure 60 - Exx strain plot using Green-Lagrangian method - 2°C/min 50mm Sample #1*

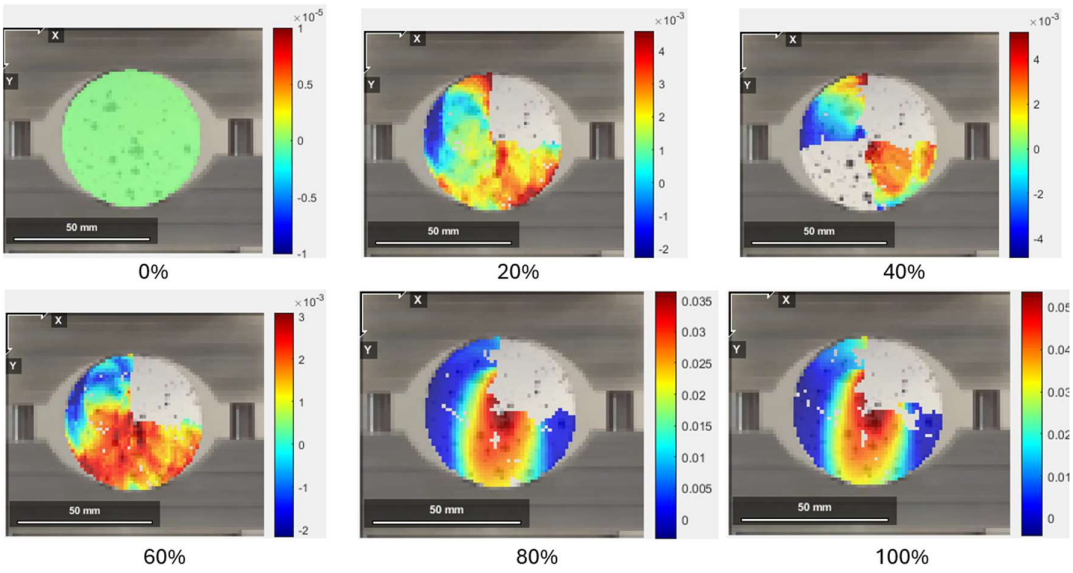


*Figure 61 - Exx strain plot using Green-Lagrangian method - 2°C/min 50mm Sample #2*

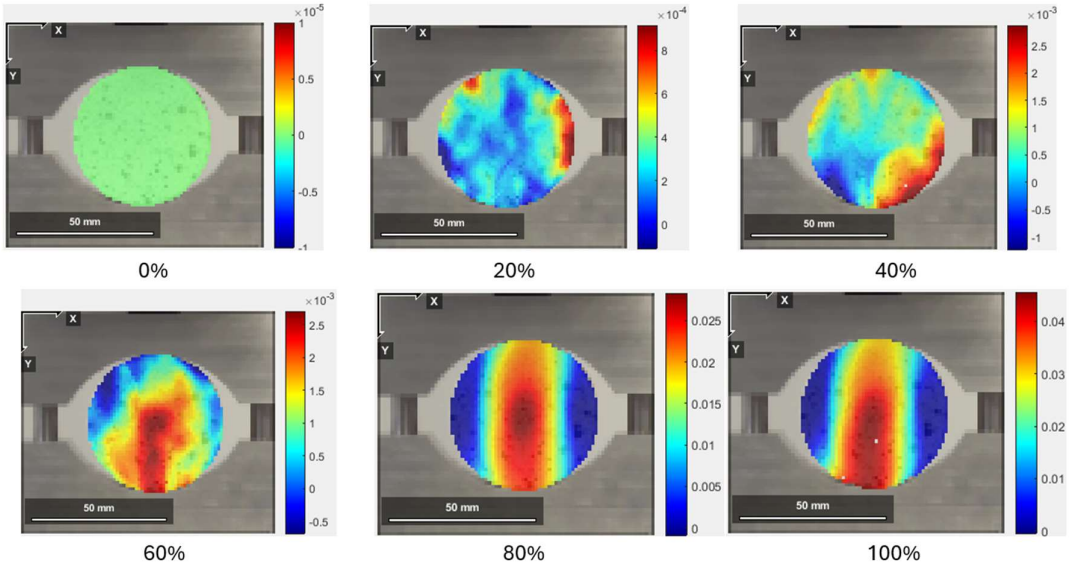


*Figure 62 - Exx strain plot using Green-Lagrangian method - 2°C/min 50mm Sample #3*

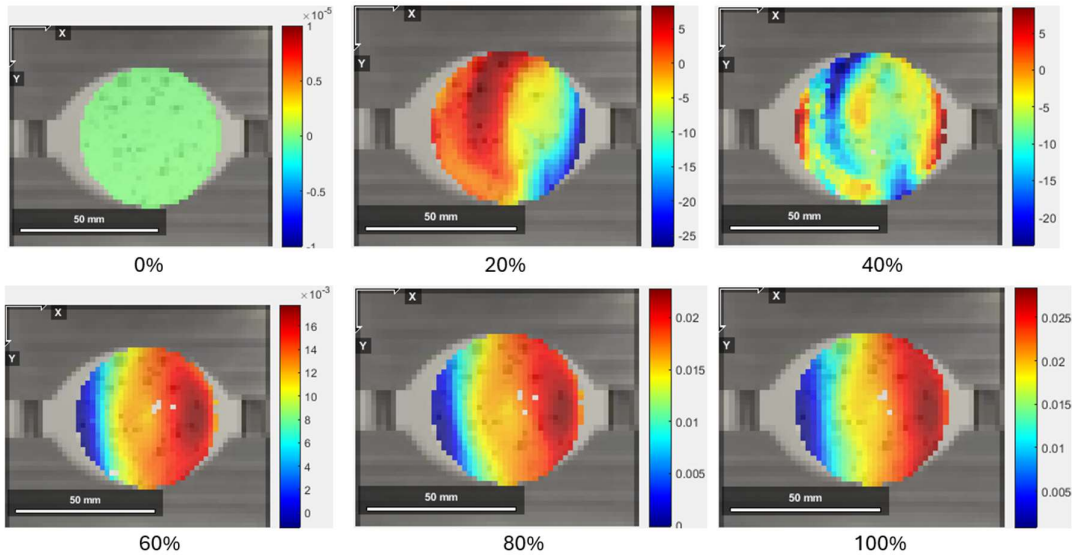


*Figure 63 - Exx strain plot using Green-Lagrangian method - 5°C/min 50mm Sample #1*

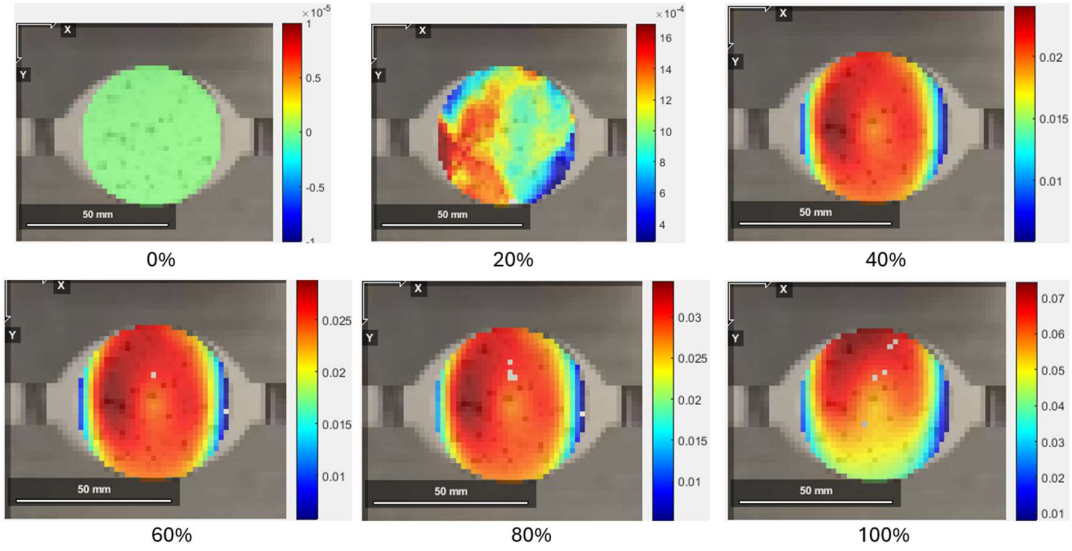


*Figure 64 - Exx strain plot using Green-Lagrangian method - 5°C/min 50mm Sample #2*

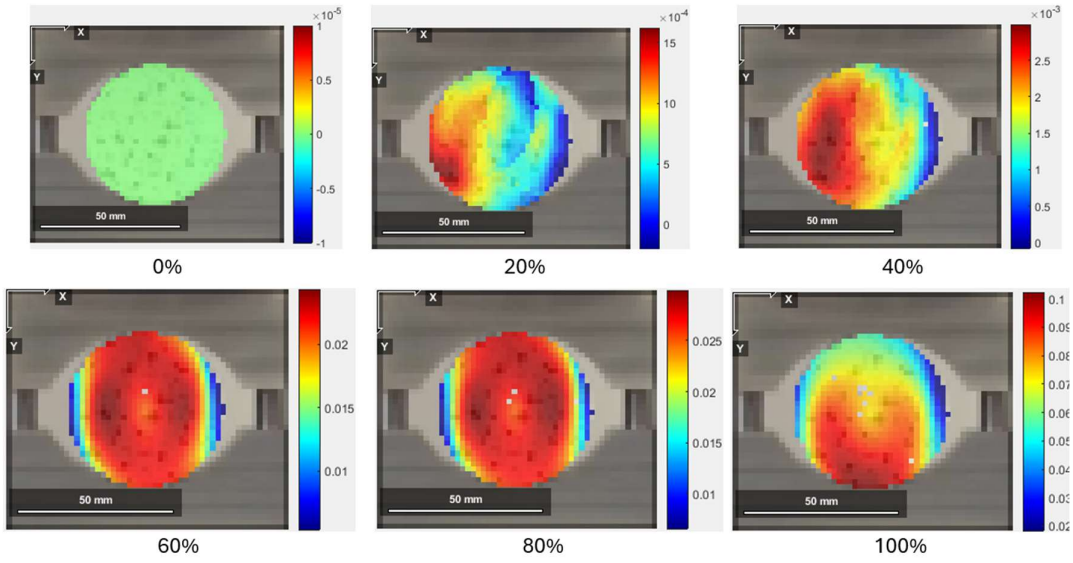


*Figure 65 - Exx strain plot using Green-Lagrangian method - 5°C/min 50mm Sample #3*

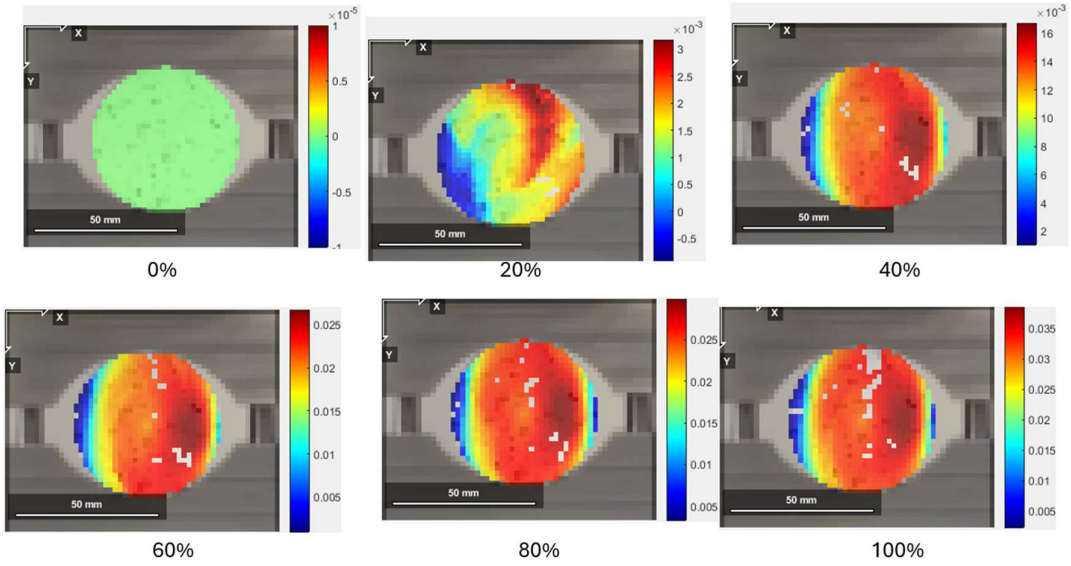


*Figure 66 - Exx strain plot using Green-Lagrangian method - 10°C/min 50mm Sample #1*

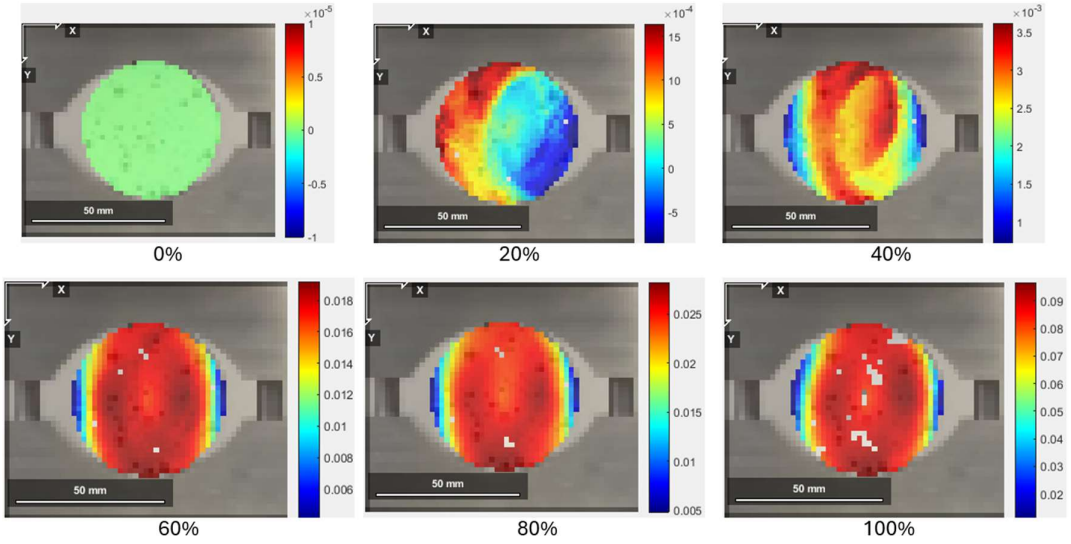


*Figure 67 - Exx strain plot using Green-Lagrangian method - 10°C/min 50mm Sample #2*

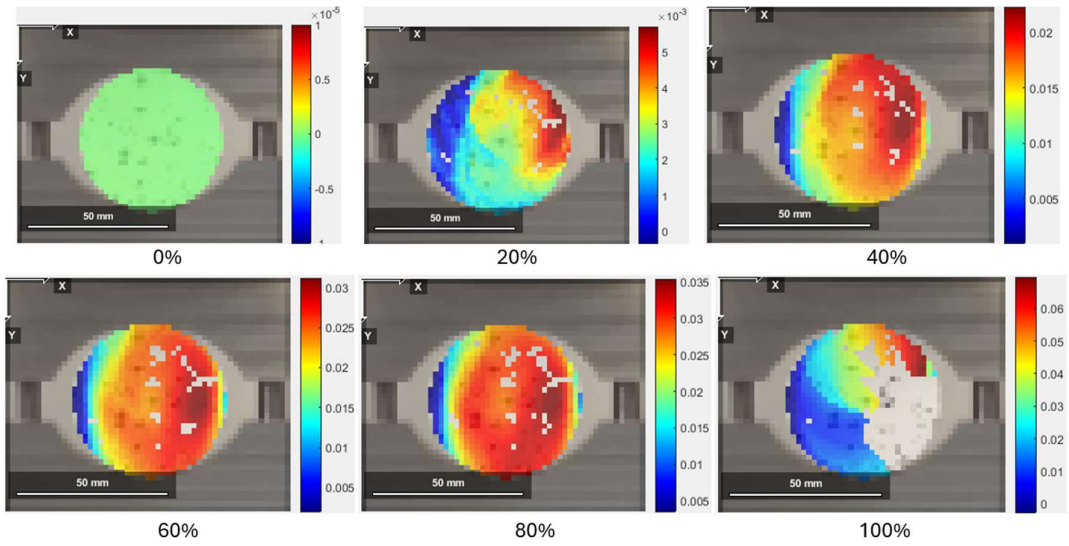


*Figure 68 - Exx strain plot using Green-Lagrangian method - 10°C/min 50mm Sample #3*

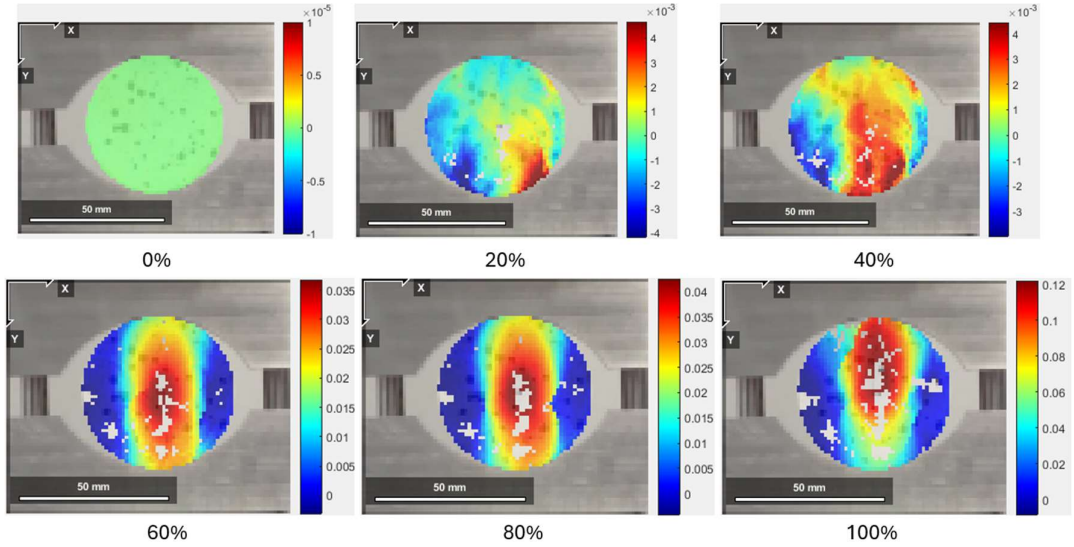


*Figure 69 - 20°C/min 50mm Tensile Sample #1 sample showing Exx strain plot*

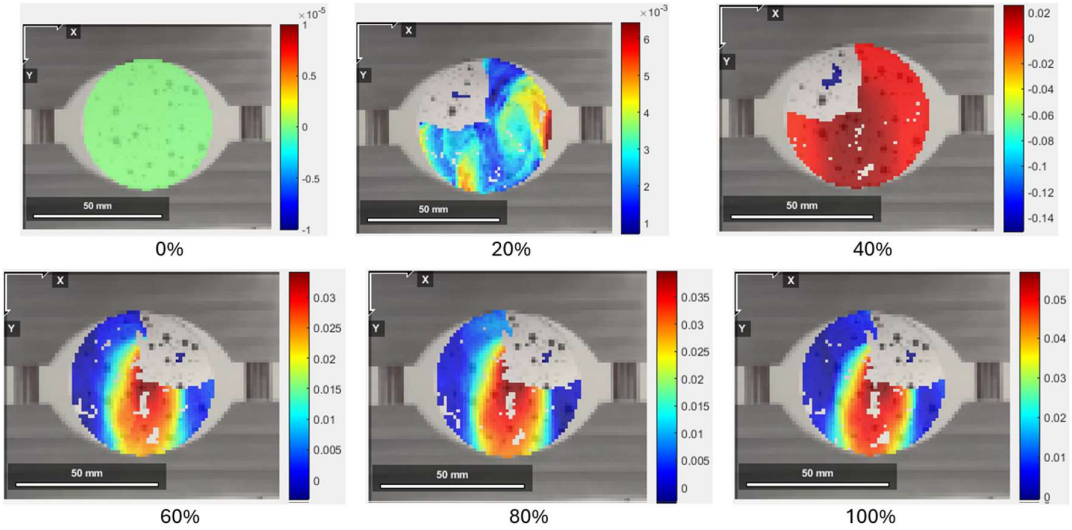


*Figure 70 - Exx strain plot using Green-Lagrangian method - 20°C/min 50mm Sample #2*

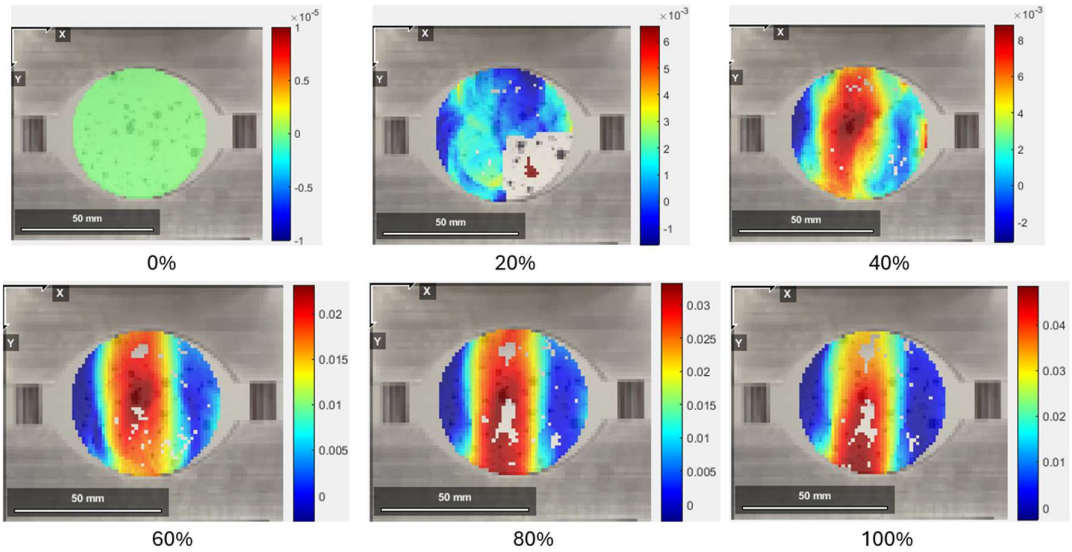


*Figure 71 - Exx strain plot using Green-Lagrangian method - 20°C/min 50mm Sample #3*

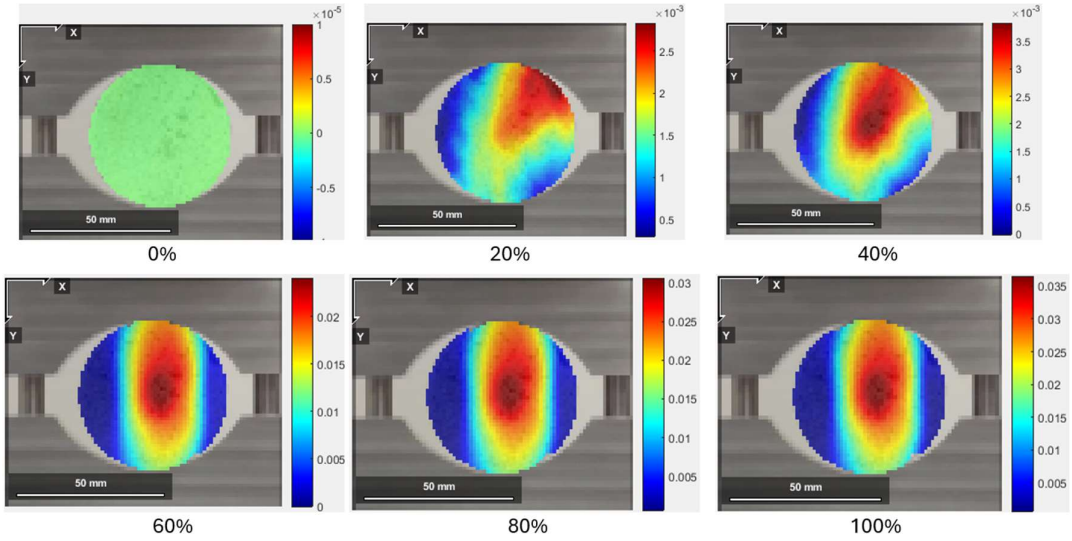


*Figure 72 - Exx strain plot using Green-Lagrangian method - MHC 50mm Sample #2*

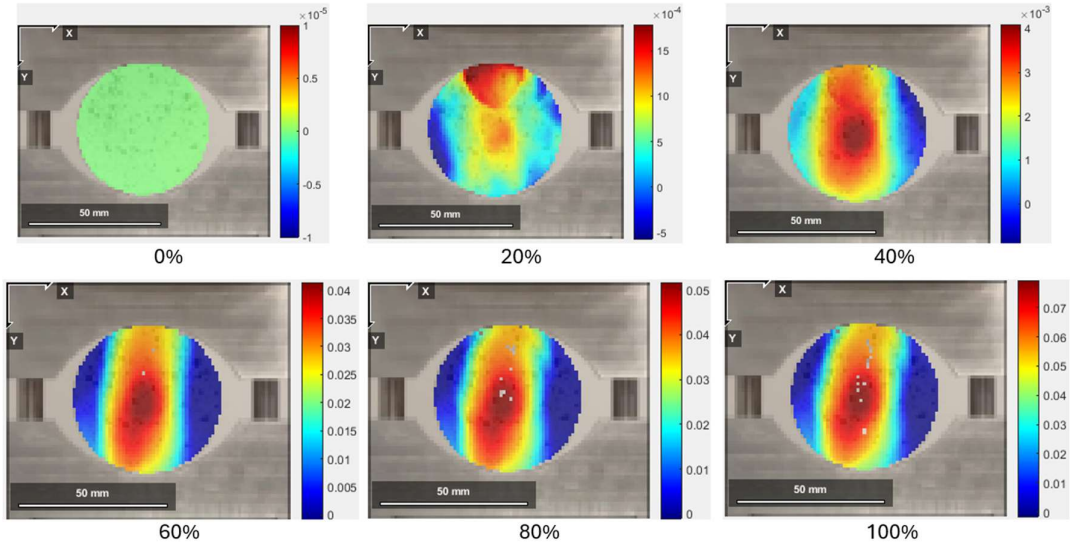


*Figure 73 - Exx strain plot using Green-Lagrangian method - MHC 50mm Sample #3*

*Table 12 – SEM results for speciments of all heat treatment tests*

| Element | Test | Atomic concentration percentage | Weight concentration percentage |
|---|---|---|---|
| Al | 1. Untreated #1 | 3.50% | 4.70% |
| Al | 1. Untreated #2 | 5.13% | 6.89% |
| Al | 1. Untreated #3 | 4.22% | 5.61% |
| Al | 2. 2°C/min #1 | 5.89% | 8.01% |
| Al | 2. 2°C/min #2 | 3.65% | 5.01% |
| Al | 2. 2°C/min #3 | 10.25% | 13.80% |
| Al | 3. 5°C/min #1 | 9.04% | 11.60% |
| Al | 3. 5°C/min #2 | 3.15% | 4.30% |
| Al | 3. 5°C/min #3 | 5.32% | 7.31% |
| Al | 4. 10°C/min #1 | 3.84% | 5.39% |

| | | | |
|---|---|---|---|
| Al | 4. 10°C/min #2 | 4.19% | 5.80% |
| Al | 4. 10°C/min #3 | 4.71% | 6.49% |
| Al | 5. 20°C/min #1 | 6.50% | 8.59% |
| Al | 5. 20°C/min #2 | 3.92% | 5.31% |
| Al | 5. 20°C/min #3 | 5.53% | 7.40% |
| Al | 5. MHC #1 | 3.96% | 5.31% |
| Al | 5. MHC #2 | 5.72% | 7.81% |
| Al | 5. MHC #3 | 3.30% | 4.30% |
| C | 1. Untreated #1 | 8.70% | 5.20% |
| C | 1. Untreated #2 | 9.86% | 5.89% |
| C | 1. Untreated #3 | 12.00% | 7.11% |
| C | 2. 2°C/min #1 | 9.93% | 6.01% |
| C | 2. 2°C/min #2 | 11.63% | 7.11% |
| C | 2. 2°C/min #3 | 12.01% | 7.20% |
| C | 3. 5°C/min #1 | 9.10% | 5.20% |
| C | 3. 5°C/min #2 | 10.71% | 6.49% |
| C | 3. 5°C/min #3 | 9.16% | 5.61% |
| C | 4. 10°C/min #1 | 18.70% | 11.69% |
| C | 4. 10°C/min #2 | 17.37% | 10.70% |
| C | 4. 10°C/min #3 | 12.54% | 7.69% |
| C | 5. 20°C/min #1 | 5.43% | 3.20% |
| C | 5. 20°C/min #2 | 7.65% | 4.60% |
| C | 5. 20°C/min #3 | 4.36% | 2.60% |
| C | 5. MHC #1 | 17.46% | 10.41% |
| C | 5. MHC #2 | 14.32% | 8.71% |
| C | 5. MHC #3 | 20.65% | 12.00% |
| Cu | 1. Untreated #1 | 0.13% | 0.40% |
| Cu | 1. Untreated #2 | 0.16% | 0.50% |
| Cu | 1. Untreated #3 | 0.19% | 0.60% |
| Cu | 2. 2°C/min #1 | 0.22% | 0.70% |
| Cu | 2. 2°C/min #2 | 0.15% | 0.50% |
| Cu | 2. 2°C/min #3 | 0.16% | 0.50% |
| Cu | 3. 5°C/min #1 | 0.17% | 0.50% |
| Cu | 3. 5°C/min #2 | 0.19% | 0.60% |
| Cu | 3. 5°C/min #3 | 0.06% | 0.20% |
| Cu | 4. 10°C/min #1 | 0.06% | 0.20% |
| Cu | 4. 10°C/min #2 | 0.09% | 0.30% |
| Cu | 4. 10°C/min #3 | 0.09% | 0.30% |
| Cu | 5. 20°C/min #1 | 0.10% | 0.30% |
| Cu | 5. 20°C/min #2 | 0.09% | 0.30% |
| Cu | 5. 20°C/min #3 | 0.06% | 0.20% |
| Cu | 5. MHC #1 | 0.16% | 0.50% |
| Cu | 5. MHC #2 | 0.12% | 0.40% |
| Cu | 5. MHC #3 | 0.46% | 1.40% |

| | | | |
|---|---|---|---|
| F | 1. Untreated #1 | 0.21% | 0.20% |
| F | 1. Untreated #2 | 0.11% | 0.10% |
| F | 1. Untreated #3 | 0.32% | 0.30% |
| F | 2. 2°C/min #1 | 0.10% | 0.10% |
| F | 2. 2°C/min #2 | 0.00% | 0.00% |
| F | 2. 2°C/min #3 | 0.21% | 0.20% |
| F | 3. 5°C/min #1 | 0.33% | 0.30% |
| F | 3. 5°C/min #2 | 0.21% | 0.20% |
| F | 3. 5°C/min #3 | 0.10% | 0.10% |
| F | 4. 10°C/min #1 | 0.10% | 0.10% |
| F | 4. 10°C/min #2 | 0.00% | 0.00% |
| F | 4. 10°C/min #3 | 0.10% | 0.10% |
| F | 5. 20°C/min #1 | 0.11% | 0.10% |
| F | 5. 20°C/min #2 | 0.21% | 0.20% |
| F | 5. 20°C/min #3 | 0.21% | 0.20% |
| F | 5. MHC #1 | 0.11% | 0.10% |
| F | 5. MHC #2 | 0.31% | 0.30% |
| F | 5. MHC #3 | 0.22% | 0.20% |
| Fe | 1. Untreated #1 | 0.25% | 0.70% |
| Fe | 1. Untreated #2 | 0.22% | 0.60% |
| Fe | 1. Untreated #3 | 0.33% | 0.90% |
| Fe | 2. 2°C/min #1 | 0.14% | 0.40% |
| Fe | 2. 2°C/min #2 | 0.11% | 0.30% |
| Fe | 2. 2°C/min #3 | 0.14% | 0.40% |
| Fe | 3. 5°C/min #1 | 0.19% | 0.50% |
| Fe | 3. 5°C/min #2 | 0.18% | 0.50% |
| Fe | 3. 5°C/min #3 | 0.18% | 0.50% |
| Fe | 4. 10°C/min #1 | 0.07% | 0.20% |
| Fe | 4. 10°C/min #2 | 0.10% | 0.30% |
| Fe | 4. 10°C/min #3 | 0.32% | 0.90% |
| Fe | 5. 20°C/min #1 | 0.11% | 0.30% |
| Fe | 5. 20°C/min #2 | 0.11% | 0.30% |
| Fe | 5. 20°C/min #3 | 0.11% | 0.30% |
| Fe | 5. MHC #1 | 0.07% | 0.20% |
| Fe | 5. MHC #2 | 0.07% | 0.20% |
| Fe | 5. MHC #3 | 0.19% | 0.50% |
| K | 1. Untreated #1 | 0.62% | 1.20% |
| K | 1. Untreated #2 | 1.03% | 2.00% |
| K | 1. Untreated #3 | 0.99% | 1.90% |
| K | 2. 2°C/min #1 | 1.17% | 2.30% |
| K | 2. 2°C/min #2 | 0.80% | 1.60% |
| K | 2. 2°C/min #3 | 1.49% | 2.90% |
| K | 3. 5°C/min #1 | 1.50% | 2.80% |
| K | 3. 5°C/min #2 | 0.61% | 1.20% |

| | | | |
|---|---|---|---|
| K | 3. 5°C/min #3 | 0.45% | 0.90% |
| K | 4. 10°C/min #1 | 0.74% | 1.50% |
| K | 4. 10°C/min #2 | 1.00% | 2.00% |
| K | 4. 10°C/min #3 | 1.10% | 2.20% |
| K | 5. 20°C/min #1 | 1.62% | 3.10% |
| K | 5. 20°C/min #2 | 1.07% | 2.10% |
| K | 5. 20°C/min #3 | 1.19% | 2.30% |
| K | 5. MHC #1 | 1.13% | 2.20% |
| K | 5. MHC #2 | 2.02% | 4.00% |
| K | 5. MHC #3 | 1.27% | 2.40% |
| Mn | 1. Untreated #1 | 0.11% | 0.30% |
| Mn | 1. Untreated #2 | 0.07% | 0.20% |
| Mn | 1. Untreated #3 | 0.07% | 0.20% |
| Mn | 2. 2°C/min #1 | 0.11% | 0.30% |
| Mn | 2. 2°C/min #2 | 0.07% | 0.20% |
| Mn | 2. 2°C/min #3 | 0.11% | 0.30% |
| Mn | 3. 5°C/min #1 | 0.11% | 0.30% |
| Mn | 3. 5°C/min #2 | 0.07% | 0.20% |
| Mn | 3. 5°C/min #3 | 0.00% | 0.00% |
| Mn | 4. 10°C/min #1 | 0.03% | 0.10% |
| Mn | 4. 10°C/min #2 | 0.07% | 0.20% |
| Mn | 4. 10°C/min #3 | 0.04% | 0.10% |
| Mn | 5. 20°C/min #1 | 0.07% | 0.20% |
| Mn | 5. 20°C/min #2 | 0.04% | 0.10% |
| Mn | 5. 20°C/min #3 | 0.07% | 0.20% |
| Mn | 5. MHC #1 | 0.07% | 0.20% |
| Mn | 5. MHC #2 | 0.07% | 0.20% |
| Mn | 5. MHC #3 | 0.08% | 0.20% |
| Nb | 1. Untreated #1 | 0.71% | 3.30% |
| Nb | 1. Untreated #2 | 0.60% | 2.80% |
| Nb | 1. Untreated #3 | 0.92% | 4.20% |
| Nb | 2. 2°C/min #1 | 0.56% | 2.60% |
| Nb | 2. 2°C/min #2 | 0.64% | 3.01% |
| Nb | 2. 2°C/min #3 | 0.73% | 3.40% |
| Nb | 3. 5°C/min #1 | 1.02% | 4.50% |
| Nb | 3. 5°C/min #2 | 0.75% | 3.50% |
| Nb | 3. 5°C/min #3 | 0.66% | 3.10% |
| Nb | 4. 10°C/min #1 | 0.79% | 3.80% |
| Nb | 4. 10°C/min #2 | 0.82% | 3.90% |
| Nb | 4. 10°C/min #3 | 0.48% | 2.30% |
| Nb | 5. 20°C/min #1 | 0.64% | 2.90% |
| Nb | 5. 20°C/min #2 | 0.64% | 3.00% |
| Nb | 5. 20°C/min #3 | 0.61% | 2.80% |
| Nb | 5. MHC #1 | 1.43% | 6.61% |

| | | | |
|---|---|---|---|
| Nb | 5. MHC #2 | 0.81% | 3.80% |
| Nb | 5. MHC #3 | 1.67% | 7.50% |
| O | 1. Untreated #1 | 60.91% | 48.50% |
| O | 1. Untreated #2 | 59.81% | 47.65% |
| O | 1. Untreated #3 | 57.11% | 45.05% |
| O | 2. 2°C/min #1 | 61.11% | 49.25% |
| O | 2. 2°C/min #2 | 60.73% | 49.50% |
| O | 2. 2°C/min #3 | 57.70% | 46.10% |
| O | 3. 5°C/min #1 | 56.98% | 43.40% |
| O | 3. 5°C/min #2 | 61.22% | 49.45% |
| O | 3. 5°C/min #3 | 63.46% | 51.75% |
| O | 4. 10°C/min #1 | 54.95% | 45.75% |
| O | 4. 10°C/min #2 | 56.31% | 46.20% |
| O | 4. 10°C/min #3 | 59.51% | 48.65% |
| O | 5. 20°C/min #1 | 63.42% | 49.75% |
| O | 5. 20°C/min #2 | 63.13% | 50.65% |
| O | 5. 20°C/min #3 | 65.50% | 52.00% |
| O | 5. MHC #1 | 55.70% | 44.24% |
| O | 5. MHC #2 | 57.80% | 46.85% |
| O | 5. MHC #3 | 50.90% | 39.40% |
| Pd | 1. Untreated #1 | 0.13% | 0.70% |
| Pd | 1. Untreated #2 | 0.15% | 0.80% |
| Pd | 1. Untreated #3 | 0.23% | 1.20% |
| Pd | 2. 2°C/min #1 | 0.17% | 0.90% |
| Pd | 2. 2°C/min #2 | 0.18% | 1.00% |
| Pd | 2. 2°C/min #3 | 0.17% | 0.90% |
| Pd | 3. 5°C/min #1 | 0.41% | 2.10% |
| Pd | 3. 5°C/min #2 | 0.17% | 0.90% |
| Pd | 3. 5°C/min #3 | 0.17% | 0.90% |
| Pd | 4. 10°C/min #1 | 0.20% | 1.10% |
| Pd | 4. 10°C/min #2 | 0.24% | 1.30% |
| Pd | 4. 10°C/min #3 | 0.13% | 0.70% |
| Pd | 5. 20°C/min #1 | 0.17% | 0.90% |
| Pd | 5. 20°C/min #2 | 0.17% | 0.90% |
| Pd | 5. 20°C/min #3 | 0.17% | 0.90% |
| Pd | 5. MHC #1 | 0.40% | 2.10% |
| Pd | 5. MHC #2 | 0.20% | 1.10% |
| Pd | 5. MHC #3 | 0.58% | 3.00% |
| Si | 1. Untreated #1 | 24.61% | 34.40% |
| Si | 1. Untreated #2 | 22.64% | 31.67% |
| Si | 1. Untreated #3 | 23.49% | 32.53% |
| Si | 2. 2°C/min #1 | 20.45% | 28.93% |
| Si | 2. 2°C/min #2 | 21.92% | 31.36% |
| Si | 2. 2°C/min #3 | 16.82% | 23.60% |

| | | | |
|---|---|---|---|
| Si | 3. 5°C/min #1 | 20.86% | 27.90% |
| Si | 3. 5°C/min #2 | 22.54% | 31.97% |
| Si | 3. 5°C/min #3 | 20.27% | 29.03% |
| Si | 4. 10°C/min #1 | 20.43% | 29.87% |
| Si | 4. 10°C/min #2 | 19.51% | 28.10% |
| Si | 4. 10°C/min #3 | 20.60% | 29.57% |
| Si | 5. 20°C/min #1 | 21.62% | 29.77% |
| Si | 5. 20°C/min #2 | 22.88% | 32.23% |
| Si | 5. 20°C/min #3 | 22.10% | 30.80% |
| Si | 5. MHC #1 | 19.17% | 26.73% |
| Si | 5. MHC #2 | 18.43% | 26.23% |
| Si | 5. MHC #3 | 20.16% | 27.40% |
| Ti | 4. 10°C/min #3 | 0.29% | 0.70% |
| Zn | 1. Untreated #1 | 0.12% | 0.40% |
| Zn | 1. Untreated #2 | 0.12% | 0.40% |
| Zn | 1. Untreated #3 | 0.12% | 0.40% |
| Zn | 2. 2°C/min #1 | 0.15% | 0.50% |
| Zn | 2. 2°C/min #2 | 0.12% | 0.40% |
| Zn | 2. 2°C/min #3 | 0.21% | 0.70% |
| Zn | 3. 5°C/min #1 | 0.29% | 0.90% |
| Zn | 3. 5°C/min #2 | 0.21% | 0.70% |
| Zn | 3. 5°C/min #3 | 0.18% | 0.60% |
| Zn | 4. 10°C/min #1 | 0.09% | 0.30% |
| Zn | 4. 10°C/min #2 | 0.12% | 0.40% |
| Zn | 4. 10°C/min #3 | 0.09% | 0.30% |
| Zn | 5. 20°C/min #1 | 0.09% | 0.30% |
| Zn | 5. 20°C/min #2 | 0.09% | 0.30% |
| Zn | 5. 20°C/min #3 | 0.09% | 0.30% |
| Zn | 5. MHC #1 | 0.09% | 0.30% |
| Zn | 5. MHC #2 | 0.12% | 0.40% |
| Zn | 5. MHC #3 | 0.54% | 1.70% |
| Zr | 1. Untreated #2 | 0.11% | 0.50% |
| Zr | 4. 10°C/min #2 | 0.17% | 0.80% |
| Zr | 5. 20°C/min #1 | 0.13% | 0.60% |
| Zr | 5. MHC #1 | 0.24% | 1.10% |

*Table 13 - Full data set of maximum strain and maximum stress at that strain for compression testing, relating to Table 4*

| **Samples** | **Max. Strain** | **Max. Axial Stress** |
|---|---|---|
| Untreated 50mm #1 - Max Temp 25°C | 0.74 | 30.84 |
| Untreated 50mm #2 - Max Temp 25°C | 0.75 | 30.56 |
| Untreated 50mm #3 - Max Temp 25°C | 0.81 | 43.36 |

| | | |
|---|---|---|
| Untreated 50mm Average - Max Temp 25°C | 0.77 | 34.92 |
| MHC 50mm #1 - Max Temp 1300°C | 1.24 | 5.80 |
| MHC50mm #2 - Max Temp 1300°C | 1.60 | 9.26 |
| MHC50mm #3 - Max Temp 1300°C | 1.55 | 7.36 |
| MHC50mm Average - Max Temp 1300°C | 1.46 | 7.47 |
| Linear 2°C/min 50mm #1 - Max Temp 1100°C | 1.45 | 21.55 |
| Linear 2°C/min 50mm #2 - Max Temp 1100°C | 1.60 | 25.27 |
| Linear 2°C/min 50mm #3 - Max Temp 1100°C | 1.57 | 25.31 |
| Linear 2°C/min 50mm Average - Max Temp 1100°C | 1.54 | 24.04 |
| Linear 5°C/min 50mm #1 - Max Temp 1100°C | 1.65 | 29.13 |
| Linear 5°C/min 50mm #2 - Max Temp 1100°C | 1.64 | 27.93 |
| Linear 5°C/min 50mm #3 - Max Temp 1100°C | 1.36 | 29.36 |
| Linear 5°C/min 50mm Average - Max Temp 1100°C | 1.65 | 28.53 |
| Linear 10°C/min 50mm #1 - Max Temp 1100°C | 1.66 | 27.61 |
| Linear 10°C/min 50mm #2 - Max Temp 1100°C | 1.50 | 25.02 |
| Linear 10°C/min 50mm #3 - Max Temp 1100°C | 1.52 | 28.61 |
| Linear 10°C/min 50mm Average - Max Temp 1100°C | 1.56 | 27.08 |
| Linear 20°C/min 50mm #1 - Max Temp 1100°C | 1.68 | 27.64 |
| Linear 20°C/min 50mm #2 - Max Temp 1100°C | 1.61 | 19.11 |
| Linear 20°C/min 50mm #3 - Max Temp 1100°C | 1.83 | 21.20 |
| Linear 20°C/min 50mm Average - Max Temp 1100°C | 1.72 | 20.16 |

*Table 14 - Full data set of maximum displacement and maximum load at that strain for tensile testing, relating to Table 5*

| **Samples** | **Max. Strain (mm)** | **Max. Axial Stress (kN)** |
|---|---|---|
| Untreated 50mm #1 - Max Temp 25°C | 0.50 | 2.65 |
| Untreated 50mm #2 - Max Temp 25°C | 0.45 | 2.72 |
| Untreated 50mm #3 - Max Temp 25°C | 0.43 | 2.43 |
| Untreated 50mm Average - Max Temp 25°C | 0.46 | 2.60 |
| MHC 50mm #2 - Max Temp 1300°C | 0.33 | 0.51 |
| MHC50mm #3 - Max Temp 1300°C | 0.79 | 0.54 |
| MHC50mm Average - Max Temp 1300°C | 0.56 | 0.53 |
| Linear 2°C/min 50mm #1 - Max Temp 1100°C | 0.49 | 1.04 |

| | | |
|---|---|---|
| Linear 2°C/min 50mm #2 - Max Temp 1100°C | 0.54 | 1.17 |
| Linear 2°C/min 50mm #3 - Max Temp 1100°C | 0.55 | 0.98 |
| Linear 2°C/min 50mm Average - Max Temp 1100°C | 0.52 | 1.06 |
| Linear 5°C/min 50mm #1 - Max Temp 1100°C | 0.42 | 0.70 |
| Linear 5°C/min 50mm #2 - Max Temp 1100°C | 0.58 | 1.40 |
| Linear 5°C/min 50mm #3 - Max Temp 1100°C | 0.65 | 1.42 |
| Linear 5°C/min 50mm Average - Max Temp 1100°C | 0.50 | 1.05 |
| Linear 10°C/min 50mm #1 - Max Temp 1100°C | 0.58 | 1.37 |
| Linear 10°C/min 50mm #2 - Max Temp 1100°C | 0.48 | 0.76 |
| Linear 10°C/min 50mm #3 - Max Temp 1100°C | 0.62 | 1.45 |
| Linear 10°C/min 50mm Average - Max Temp 1100°C | 0.56 | 1.19 |
| Linear 20°C/min 50mm #1 - Max Temp 1100°C | 0.42 | 0.81 |
| Linear 20°C/min 50mm #2 - Max Temp 1100°C | 0.40 | 0.74 |
| Linear 20°C/min 50mm #3 - Max Temp 1100°C | 0.49 | 0.63 |
| Linear 20°C/min 50mm Average - Max Temp 1100°C | 0.45 | 0.69 |

*Table 15 - Standard deviations of tested samples using the excel function "=STDEV.P"*

| | Untreated (MPa) | | | | 2°C/min (MPa) | | | |
|---|---|---|---|---|---|---|---|---|
| **Diameter** | **1** | **2** | **3** | **STDEV.P** | **1** | **2** | **3** | **STDEV.P** |
| 15mm | 22.6 | 30.1 | 21.1 | **3.9** | 16.6 | 19.0 | 20.8 | **1.7** |
| 32mm | 25.4 | 28.1 | 22.8 | **2.2** | 11.2 | 17.3 | | **3.0** |
| 50mm | 17.4 | 15.4 | 21.8 | **2.7** | 10.5 | 12.7 | 12.3 | **1.0** |
| 67mm | 19.2 | 12.7 | 12.2 | **3.2** | 10.1 | 17.0 | 16.9 | **3.2** |
| 75mm | 25.5 | 26.2 | 26.2 | **0.4** | 27.7 | 27.3 | 27.4 | **0.2** |